Radiosensitizing effect of gold nanoparticles: PENELOPE simulations

Catarina F. Dias
Mestrado em Física Médica
Departamento de Física e Astronomia
2023

Orientador
Pedro Manuel Peixoto Teles, Professor Auxiliar,
Faculdade de Ciências da Universidade do Porto

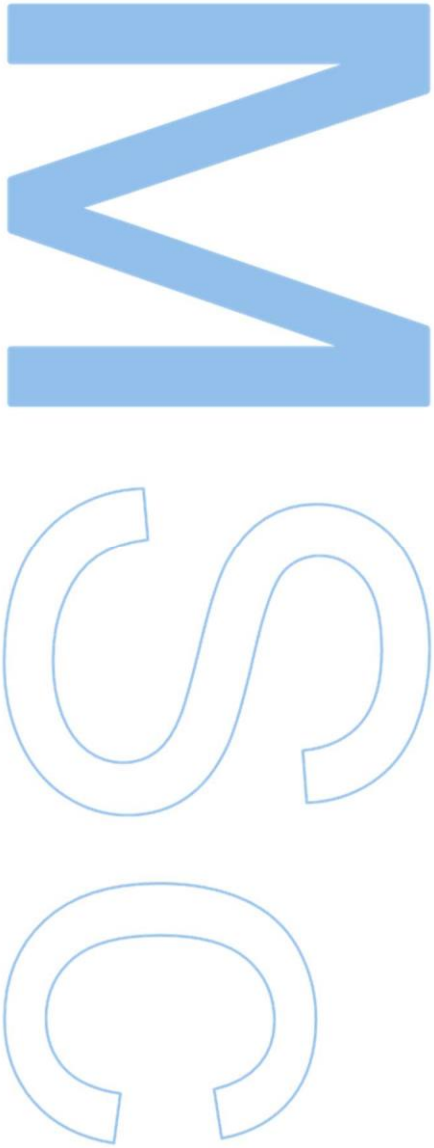


U.PORTO
FACULDADE DE CIÊNCIAS
UNIVERSIDADE DO PORTO

UNIVERSIDADE DO PORTO

MASTERS THESIS

Radiosensitizing effect of gold nanoparticles: PENELOPE simulations

Author:
Catarina F. DIAS

Supervisor:
Pedro TELES

A thesis submitted in fulfilment of the requirements
for the degree of MSc. Medical Physics

at the

Faculdade de Ciências da Universidade do Porto
Departamento de Física e Astronomia

January 26, 2024

" Afinal, há é que ter paciência, dar tempo ao tempo, já devíamos ter aprendido, e de uma vez para sempre, que o destino tem de fazer muitos rodeios para chegar a qualquer parte. "

José Saramago

Acknowledgements

Quero começar por agradecer à Universidade do Porto, nomeadamente à Faculdade de Ciências do Porto, por me ter proporcionado a frequência do Mestrado em Física Médica, o qual permitiu que fosse desenvolvido todo o trabalho retratado na presente tese. Seguidamente, agradecer a gentileza com que o orientador, Pedro Teles, disponibilizou o seu computador, permitindo a obtenção de resultados através das simulações Monte Carlo. Quero igualmente aqui reiterar a minha gratidão pelos seus ensinamentos, transmitidos ao longo destes dois anos, e por me fazer sentir motivada para o projeto, através de palavras de encorajamento, levando-me a não desistir sempre que surgia um revés. Agradeço também aos meus pais, por me terem apoiado, dia após dia nesta minha jornada, tornando menos árduo todo o trajeto por mim desbravado. Um especial agradecimento ao meu irmão Manuel João que, embora mais novo do que eu, se tem revelado uma verdadeira inspiração para mim. Também não posso deixar de reconhecer o apoio incessante da minha colega de curso, Rita Albergueiro que, com a sua sapiência e amizade, me fez acreditar que com esforço, determinação e crença no que se está a fazer não existem impossíveis. Quero também dedicar algumas palavras de gratidão aos meus amigos, em especial ao Tiago Couraceiro pela disponibilização do seu computador, o qual constituiu um auxílio precioso nas várias simulações desempenhadas com o software PENElOPE. A todos eles um profundo bem-haja por todas as palavras de encorajamento.

UNIVERSIDADE DO PORTO

Abstract

Faculdade de Ciências da Universidade do Porto
Departamento de Física e Astronomia

MSc. Medical Physics

Radiosensitizing effect of gold nanoparticles: PENELOPE simulations

by Catarina F. DIAS

In 2020, breast cancer alone accounted for 12% of the staggering 18 million new cancer cases worldwide, highlighting the urgent need for effective therapies. Among various approaches, radiotherapy is a well-established method for combating cancer by inducing DNA damage through ionizing radiation. Precision in delivering radiation doses is crucial in this endeavor, and gold nanoparticles (AuNPs) have emerged as promising tools to enhance the effectiveness of radiotherapy.

The fundamental principle behind AuNP radio-enhancement lies in their ability to release numerous electrons within a nanoscale volume, thereby amplifying the biological damage caused by radiation to the tumor while sparing the healthy tissue. To investigate the sensitizing effects of AuNPs, researchers often employ Monte Carlo simulations to calculate the dose enhancement in specific scenarios. One such simulation tool is the PENELOPE code, which utilizes the PenEasy program for simulating coupled electron-photon transport.

This study explores the underlying physical principles behind the growing interest in AuNP radiosensitization, reviews the studies conducted in this field over the years, and investigates the functionality of PENELOPE. Additionally, it aims to provide specific results by simulating basic geometry setups.

In a water medium, simulations involving the irradiation of a gold nanoparticle with a 50 kVp source revealed a higher production of low-energy electrons compared to when using a 100 kVp source. This observation highlights the significant role played by low-energy electrons in increasing energy deposition in the vicinity of AuNPs.

In breast tissue, smaller AuNPs have lower DER, using the same source size. For instance, at 200-800 nm from a nanoparticle, the largest diameter (100 nm) have a dose

increase of 100 times, while the smallest (12.5 nm) only doubles. Photoelectric absorption dominates gold volume, contributing with 95% of the total secondary electrons for all studied diameters. A method based on the Local Effect Model (LEM) was employed to predict survival curves influenced by AuNPs. This approach divided a volume into concentric shells and computed damage using a spherical dose distribution. The results indicated substantial damage when a single nanoparticle with a 100-nanometer diameter was present, primarily due to its high gold mass concentration. Even at the lowest concentration, there was a noteworthy reduction in survival fraction, with a SER of 1.77 attained. Incorporating a distribution of AuNPs within the cytoplasm of an elliptical cell, it was determined that under a 1.5% mass-weight condition, the dose absorbed by the nucleus doubled compared to the scenario without AuNPs. This outcome held true for both 100 nm and 50 nm nanospheres.

Keywords: Gold nanoparticle (AuNp) – Monte Carlo – PENELOPE – photoelectric absorption – low-energy electrons – dose enhancement ratio (DER) – spherical shell

UNIVERSIDADE DO PORTO

Resumo

Faculdade de Ciências da Universidade do Porto
Departamento de Física e Astronomia

Mestrado em Física Médica

Efeito de Radiossensibilização por nanopartículas de ouro: Simulações com PENELOPE

por Catarina F. DIAS

Em 2020, o cancro da mama representou 12% dos 18 milhões de novos casos de cancro em todo o mundo, enfatizando a necessidade urgente de terapias eficazes. Entre várias abordagens, a radioterapia é um método bem estabelecido no combate ao cancro, causando danos no ADN através de radiações ionizantes. A precisão na administração das doses de radiação é crucial neste esforço. As nanopartículas de ouro (AuNPs) têm emergido como ferramentas promissoras para aumentar a eficácia da radioterapia.

O princípio fundamental por detrás do efeito de radiossensibilização das AuNPs envolve a libertação de numerosos eletrões num volume nanométrico, amplificando assim os danos biológicos causados pela radiação. Para estudar os efeitos de sensibilização das AuNPs, os investigadores frequentemente recorrem a simulações para calcular o aumento da dose em cenários específicos. Uma dessas ferramentas de simulação é o código PENELOPE, que utiliza o programa PenEasy para simular o transporte acoplado de eletrões e fotões.

Este estudo explora os princípios subjacentes ao crescente interesse na radiossensibilização com AuNPs, analisa os estudos realizados neste campo ao longo dos anos e investiga a funcionalidade do PENELOPE. Além disso, tem como objetivo fornecer resultados específicos através da simulação de configurações geométricas básicas.

Num meio constituido por água, as simulações envolvendo a irradiação de uma nanopartícula de ouro com uma fonte de 50 kVp revelaram uma maior produção de eletrões de baixa energia em comparação com o uso de uma fonte de 100 kVp. Esta observação sublinha o importante papel desempenhado pelos eletrões de baixa energia na amplificação da deposição de energia nas proximidades das AuNPs.

No tecido mamário, as AuNPs menores exibiram um DER menor, utilizando a mesma fonte. Por exemplo, a uma distância de 200 a 800 nm de uma nanopartícula, o maior diâmetro (100 nm) resultou em um aumento de dose cerca de 100 vezes maior, enquanto o menor (12,5 nm) apenas duplicou a dose. A absorção fotoelétrica foi o fenómeno predominante no volume de ouro, contribuindo com 95% dos eletrões totais para todos os diâmetros estudados. Para prever as curvas de sobrevivência influenciadas pelo ouro, foi empregado um método com base no LEM. Esse método dividiu um volume em cascas concêntricas e calculou o dano usando uma distribuição esférica de dose. Os resultados indicaram danos significativos, mesmo quando considerando apenas uma única nanopartícula com um diâmetro de 100 nanômetros, principalmente devido à sua alta concentração de massa de ouro. Mesmo com concentrações mais baixas, houve uma notável redução na fração de sobrevivência, alcançando um SER de 1,77. Ao incorporar uma distribuição de AuNPs no citoplasma de uma célula elíptica, foi determinado que, sob uma condição de 1,5% de massa de ouro, a dose absorvida pelo núcleo dobrou em comparação com o cenário sem AuNPs. Esse resultado é válido tanto para nanoesferas de 100 nm como para aquelas com 50 nm de diâmetro.

Palavras-Chave: Nanopartículas de ouro – Monte Carlo – PENELOPE – absorção fotoelétrica – eletrões de baixa energia – razão de melhoramento de dose – casca esférica

Contents

Acknowledgements v

Abstract vii

Resumo ix

Contents xi

List of Figures xv

List of Tables xix

1 Introduction 1

2 Ionizing radiation 5
2.1 Photon interactions . . . 9
2.1.1 Rayleigh scattering . . . 9
2.1.2 Photoelectric Effect . . . 10
2.1.3 Compton Scattering . . . 11
2.1.4 Pair production . . . 13
2.2 Electron interactions . . . 14
2.2.1 Atomic relaxation . . . 16
2.3 X-ray source . . . 17
2.3.1 SpekPy . . . 22
2.4 Dosimetry . . . 23
2.4.1 Radiometric quantities . . . 23
2.4.2 Interaction coefficients . . . 24
2.4.3 Energy deposition . . . 25

3 Gold Nanoparticles and radiosensitizing effects 29
3.1 Physics of Gold Atoms . . . 30
3.2 Radiobiology . . . 33
3.3 State-of-the-art . . . 37
3.3.1 Local Effect Model . . . 45

4 Computational Techniques 49
4.1 Monte Carlo . . . 49

4.1.1 Radiation Transport in Therapy . . . 50
4.1.2 Analog simulation *vs.* condensed history . . . 54
4.2 PENELOPE . . . 56
4.2.1 PenEasy . . . 57
4.2.2 Source Models . . . 58
Source Box-Isotropic-Gauss-Spectrum (BIGS) . . . 59
Source Phase Space File (PSF) . . . 60
4.2.3 Geometry . . . 61
4.2.4 Transport Parameters . . . 66
4.2.5 Tallies . . . 67
4.2.5.1 Tally Spatial Dose Distribution . . . 68
4.2.5.2 Tally Spherical Dose Distribution . . . 68
4.2.5.3 Tally Energy Deposition . . . 68
4.2.5.4 Tally Fluence Track Length . . . 69
4.2.5.5 Tally Phase Space File . . . 69

5 Monte Carlo simulations: results and discussion 71
5.1 Gold nanoparticle surrounded by water . . . 71
5.2 Radiossensitization effect of a single AuNP in breast tissue . . . 78
5.2.1 Dose enhancement ratio . . . 80
5.2.2 Surrounding Halo . . . 81
5.3 Survival curves . . . 89
5.4 Distribution of AuNPs in a cell . . . 95
6 AuNps (D = 100 nm) in the cytoplasm . . . 96
2000 AuNPs in the cytoplasm . . . 98
Alternative Scenarios . . . 101

6 Conclusion 105

A KERMA expression 109

B SpekPy settings 111

C PENELOPE data 113
C.1 Database for photon interactions . . . 113
C.2 Number codes used by PENELOPE . . . 115

D Implemented simulations - additional information 117
D.1 Fortran error within source material . . . 117
D.2 Water medium . . . 118
D.3 Propagation of uncertainties . . . 118
D.4 Breast tissue medium . . . 118
D.4.1 Transport Parameters . . . 118
D.4.2 Code for reading Spherical dose . . . 119
D.4.3 Creation of PSF . . . 120
D.4.4 Function for grouping shells . . . 125
D.4.5 Lognormal Distribution . . . 127

Bibliography **129**

List of Figures

2.1 The change in direction and energy of a particle following its collision with a target (adapted from [8]). . . . 5
2.2 Predominant photon interaction in energy deposition, where k represents the photon's energy in units of the electron rest energy [11]. . . . 9
2.3 Schematic representation of the Compton scattering [7]. . . . 12
2.4 Interactions between electrons and atoms for different impact parameters [7]. 16
2.5 Non-radiative processes caused by atomic relaxation phenomena [7]. . . . 17
2.6 Schematic representation of an X-ray tube [15], with a zoom within the red circumference [14] in order to understand the *line focus principle* . . . 17
2.7 spectrum[18] . . . 21
2.8 Diagram illustrating the process of generating an X-ray spectrum using the SpekPy package in the Python programming language. . . . 22

3.1 Cross section of Photoelectric effect as function of photon energy [11]. . . . 30
3.2 Left side: Ratio of Mass Attenuation Coefficients (Material with 1% Gold *vs.* Water); Right side: Ratio of Mass Energy Absorption Coefficients (Material with 1% Gold *vs.* Water) [5]. . . . 32
3.3 Range of low-energy electrons in liquid water [22] and in a gold material [23]. . . . 32
3.4 Two possible lethal chromosome aberrations, depending on the dose [26]. . 36
3.5 Contribution of Auger electrons and photoelectrons to dose deposition as a function of distance from the center of the nanoparticle [32]. . . . 40
3.6 Range of electrons escaping a gold nanoparticle for different radiation sources [30]. . . . 42
3.7 Survival curves for different distributions of AuNPs (=GNPs) within a cell, considering various radiation sources: kilovoltage photons on the left, protons in the middle, and megavoltage photons on the right [38]. . . . 44
3.8 Exemplification of the LEM principle, where the nucleus is divided into small compartments [41]. . . . 46
3.9 Comparison of the survival curves derived from experimental data with the predictions made by the LEM model, revealing a high degree of concordance [32]. . . . 48

4.1 Representation of two different Monte Carlo sampling techniques. a) Random sampling from a distribution $p(s)$ using the inverse-transform method [8] b) Random sampling using a simple rejection method. . . . 51
4.2 Illustration depicting the generation of random trajectories using a detailed simulation approach [8]. . . . 54

4.3 A schematic representation exemplifying how PENELOPE operates during photon simulations. . . . 58
4.4 Tree diagram illustrating the structure of the PenEasy input file. . . . 59
4.5 Two distinct ways of representing the identical geometry file, emphasizing the significance of accurately specifying the superimposed bodies. . . . 66

5.1 Output spectra generated using SpekPy for tube voltages of 50 kVp (blue) and 100 kVp (orange). . . . 72
5.2 Dose enhancement ratio for different combinations of energy source and nanoparticle size. a) nanometric scale for $D_{NP} = 100$nm; b) nanometric scale for $D_{NP} = 50$nm; c) micrometric scale for $D_{NP} = 100$nm; d) micrometric scale for $D_{NP} = 50$nm. . . . 74
5.3 Probability of electron emission, considering an irradiation with 50 kVp and 100 kVp X-rays. a) diameter of 100 nm; b) diameter of 50 nm. . . . 75
5.4 Geometry setups considered, where the source has a circular shape. a) irradiation of a sphere; b) irradiation of a cylinder through its transversal axis; c) irradiation of a cylinder through its longitudinal axis. . . . 76
5.5 Dose enhancement ratio for cylinder irradiations and different energy source. a) 100 shells up to 1 µm distance; b) 50 shells up to 50 µm distance. . . . 76
5.6 Probability of electron emission for irradiation through the transversal axis of a cylinder. . . . 77
5.7 X-ray spectra obtained by SpekPy, using a tube voltage of 50 kVp. . . . 79
5.8 Dose enhancement ratio in the vicinity of a gold nanoparticle surrounded by breast tissue. a) distances up to 1000 nm; b) distances between 1000 and 5000 nm; c) distances further than 5000 nm. . . . 81
5.9 Scheme for better understanding the method used in the creation of PSFs. . 82
5.10 Contribution of the different interactions for secondary electrons generation in gold (left) and in breast tissue (right). . . . 87
5.11 Spectra of Auger electrons that were detected in the halo surrounding a AuNP with 100 nm diameter. . . . 89
5.12 Diagram illustrating the partitioning in spherical shells surrounding a gold nanoparticle for the application of a model based on LEM. . . . 90
5.13 Survival curves obtained based in the DER around an unique AuNP. . . . 94
5.14 Cell geometry. a) Vision through the z-axis of a cell in the absence of gold nanoparticles; b) Vision through the y-axis of a cell containing 6 AuNPs; c) Vision through the z-axis of a cell with 2000 AuNPs distributed in the cytoplasm. . . . 96
5.15 Example of the structure of a PSF, as well as the creation of the matrix "mat_dose". . . . 97
5.16 Histogram of the dose deposited in the voxels that constitute the nucleus for the case of 6 AuNPs distributed in a cell. . . . 97
5.17 Histogram and adjusted PDF curve for a distribution of 2000 AuNPs with diameter of 50 nm (left) and 100 nm (center). On the right, their distributions are illustrated together with the case of absence of gold for comparison. 101
5.18 Energy deposition in the nucleus for different distributions of AuNPs in a cell. . . . 102

5.19 Dose absorbed by the nucleus for the same concentration of gold nanoparticles with different diameters in the cytoplasm (left) and on the surface (right). . . . 102
5.20 Scheme representing the distribution of 2000 AuNPs in the cytoplasm (left) and on the surface of a cell (right). . . . 103

D.1 Fortran code that generates errors when specifying the 'source material' in PenEasy input file. . . . 117
D.2 Code implemented for reading data files of spherical dose. . . . 119
D.3 Function that can resolve some issues related with the large extent of Phase Space Files in Jupyther Notebook. . . . 119
D.4 Funtion used for reading and examinign the Phase Space Files. . . . 120
D.5 Contribution of the different mechanisms for secondary electrons generation in tissue, assuming an AuNP with diameter of 100 nm (left), 25 nm (center) and 12.5 nm (right). . . . 121
D.6 Function used to determine the principal shell transitions involved in atoms ionization. . . . 121
D.7 Function developed to transform the number code used by PENELOPE in shell labels. . . . 122
D.8 Function developed for grouping the subshells around a AuNP in ticker shells. . . . 125
D.9 Input geometry file of the cell. The nucleus and the cytoplasm are defined by ellipsoids with different axis. The external medium is a sphere. . . . 125
D.10 Code used for reading the file 'TallySpatialDose Distrib' given by PenEasy. 126
D.11 Example of various probability density functions for doses on the left and the result of their superimposition on the right. . . . 126
D.12 Developed code for scattering the positions of numerous nanoparticles within the cytoplasm of a cell. . . . 126
D.13 Code used for writing the geometry file of one nanosphere. . . . 127

List of Tables

2.1 Events that must be considered during the calculation of the interaction probability. . . . 7

3.1 Electron binding energies for the gold element (Z=89) [21]. . . . 31

4.1 An example of the PDFs employed for simulating Photoelectric absorption in PENELOPE. . . . 56
4.2 Labels of the columns presented in a Phase Space File produced by PenEasy. . . . 61

5.1 Data obtained in the surrounding halo of a gold nanoparticle. . . . 84
5.2 Data obtained in the surrounding halo of a nanoparticle made of tissue. . . . 86
5.3 Numerical values used for calculation of the Equation 5.3. . . . 92
5.4 Values obtained for parameters α, β and the calculated SER. . . . 94

B.1 Available features within SpekPy toolkit [48]. . . . 111

C.1 Probability density functions (of the type $\Gamma(X)g(X)$) used by PENELOPE for simulation of photon interactions. . . . 114
C.2 Numerical labels for designating atomic electron shells [8]. . . . 115
C.3 Code number for the interaction events (ICOL) [8]. . . . 115

D.1 Transport parameters used for all the simulations that considered a medium of water. . . . 118
D.2 Transport parameters used for the simulations using a medium of breast tissue. . . . 118
D.3 Principal transitions detected in the surrounding halo of a nanoparticle with 100 nm diameter. . . . 122
D.4 Principal transitions detected in the surrounding halo of a nanoparticle with 50 nm diameter. . . . 123
D.5 Principal transitions detected in the surrounding halo of a nanoparticle with 25 nm (left) and 12.5 nm diameter (right). . . . 124

Chapter 1

Introduction

For centuries, cancer has plagued humanity and remains a significant global health concern in the 21st century. In 2020, there were an astounding 18.1 million new cases of cancer, affecting people of all genders, with women experiencing slightly higher incidence rates [1]. Breast cancer stands as a substantial global health challenge, constituting a noteworthy 12.2% of all newly reported cancer diagnoses. In Portugal, particularly, there were approximately 7000 new breast cancer cases reported, reflecting the consistent global prevalence of this widespread disease. Tragically, approximately half of these cases resulted in cancer deaths [2], highlighting the urgent necessity for comprehensive healthcare initiatives and effective cancer management.

Researchers from all over the world have been dedicating their efforts to combat cancer. With its multifaceted causes, including exposure to radiation and pollutants, sedentary lifestyles, poor dietary choices, smoking, and stress [3], preventing cancer remains a challenging task. As a result, various tumor therapy approaches have been investigated to prevent the uncontrolled growth of cancer cells, which is often induced by mutations in genes that are responsible for repairing DNA.

Radiotherapy is a well-researched field, known for its ability to kill cells and reduce tumor sizes by inflicting in them irreversible DNA damage through the use of ionizing radiation. Nonetheless, the efficacy of radiotherapy largely depends on avoiding radiation exposure to neighboring healthy tissues, thus enhancing the overall quality of life of the patient. It is crucial to ensure precise delivery of the radiation dose since cancerous and healthy tissues have similar mass absorption properties. To achieve this, modern radiation therapy techniques utilize a variety of spatially modulated beams to precisely shape

the treatment volume, closely aligning it with the intended target. When combined with strategies designed to increase the sensitivity of cancer cells to radiation, the chances of a successful treatment outcome are significantly improved.

Furthermore, recent significant progress in nanotechnology has ignited optimism for surpassing the limitations of conventional cancer treatments. Nanotechnology involves engineering functional molecular systems within the nanometer range ($1 - 100$ nm), offering unparalleled control over properties just beyond the scale of individual atoms. The range of sizes in nanotechnology is highly important in the fields of medicine and biology. Nanomaterials have the unique ability to interact closely with cellular components and mimic biological molecules. This combination of nanotechnology and biology offers great potential for improving diagnostic tools, contrast agents, drug delivery systems, and pharmaceuticals [3].

Gold nanoparticles (AuNPs) have attracted considerable attention in medicine due to their exceptional biocompatibility, remarkable optical properties, unique surface chemistry, and precise size and shape control [4]. Their versatility extends to various medical applications, such as drug delivery, tumor detecting, and photothermal therapy, making them an excellent choice for cancer treatment. However, this study is primarily concerned with the use of AuNPs to enhance radiation effects. The basic idea behind AuNP radio-enhancement is their ability to release electron cascades within a nanoscale volume, resulting in an amplification of biological damage caused by the exciting radiation [5].

In order to understand the physical principles of radiosensitization with gold nanoparticles, Chapter 2 is devoted to a basic understanding of the physical mechanisms involved in the interactions of ionizing radiation with matter. In this chapter, ionizing radiation is firstly divided into two fundamental components: photon interactions and electron interactions. Subsequently, the chapter explores the atomic relaxation processes and reveals the intricate sequence of events that unfold after these interactions. The remainder of the chapter focuses on *Radiobiology*, investigating the biological effects induced by ionizing radiation. Finally, a central aspect of radiation therapy is addressed: dosimetry, which involves a thorough study of radiometric quantities, interaction coefficients and energy deposition.

After explaining the fundamental principles and definitions related to ionizing radiation, Chapter 3 discusses the physical mechanisms involved in AuNP's effect on dose enhancement. The interaction process known as photoelectric absorption is emphasized

due to its role in initiating a cascade process that causes multiple emissions of electrons. Then, a brief overview of the recent studies on gold nanoparticles is presented, covering different approaches to assembly the varying AuNP size, cell geometry, gold distribution, energy source, and more. The chapter concludes with a reference to the Local Effect Model (LEM), which extrapolates dose enhancements derived from a single AuNP. Accurately quantifying the impact of a single AuNP on its immediate surroundings remains a difficult task, therefore, in the case of multiple AuNPs, the LEM model is often used [6].

Given that the radiosensitizing effect of AuNPs is initiated by an external beam that stimulates gold atoms, Chapter 2.3 is dedicated to providing a comprehensive exploration of the X-ray source. The fundamental structure of an X-ray tube is introduced, along with a briefly explanation of its individual components and their contributions to the output spectrum. The conclusions of this section constitutes a summary of the functionality of a toolkit utilized in this study called SpekPy.

To study the sensitizing effects of gold nanoparticles, researchers often use Monte Carlo simulations to calculate the dose increase that AuNPs induce in specific scenarios. The Monte Carlo technique is a numerical strategy for modeling the behavior of complex systems through repeated random sampling. Since this method is now widely used in radiation physics research, especially for calculating particle transport parameters in certain media, one chapter is dedicated to the Monte Carlo technique. Chapter 4 first introduces the principles of this method and mentions two random sampling methods that are frequently used in the simulation of radiation transport in therapy: the inverse-transform method and the rejection method. After that, the concepts of analog simulation and condensed history are introduced and briefly elucidated.

The latter section of Chapter 4 is devoted to a specific Monte Carlo algorithm and computer code known as PENELOPE, which was used in this thesis to simulate coupled electron–photon transport. The aim is to provide a comprehensive understanding of how Monte Carlo techniques are applied in PENELOPE, especially in the simulation of photon interactions. Moreover, since PENELOPE relies on a main program, called PenEasy, for its operation, this chapter also delves into the structure of the input file within the PenEasy software. This work aims to provide all the information necessary for a user to operate PenEasy from the beginning, taking into account all the peculiarities of the software language. Not all the features available in the program were accessed, but the ones that are used are explained in a clear manner.

This thesis delves into the principles driving the increasing interest in AuNP radiosensitization, investigates the studies conducted in this field over the years, and explores the functionality of PENELOPE, but also aims to present specific simulation results. This last purpose is presented in Chapter 6. In an initial approach, the results of simulations involving AuNPs surrounded by water are presented. The objective is to validate the employed methods through comparison with another study, as this marks the first simulation conducted with PENELOPE. After code validation, variations in the geometry of gold nanoparticles were explored. Subsequently, simulations were performed with gold nanoparticles in breast tissue, analyzing the impact of gold sphere diameter on energy optimization. The influence of a single AuNP in its surroundings was studied and used to extrapolate the survival curve, using a method based on the Local Effect Model (LEM). After having investigated nanoparticle sizes, the study also explores the differences in energy absorption within a cell when considering a distribution of numerous AuNPs. The chapter ends by assessing the impact of source size on dose enhancement in the vicinity of a single gold nanoparticle.

Indeed, the focus in this study centers on the realm of AuNPs and their remarkable ability to enhance energy deposition in their immediate surroundings. It's truly extraordinary to reflect on the early stages of radiation physics research where the potentially harmful effects of ionizing radiation on human tissues were often ignored, leading to disastrous consequences for many pioneers in the field [7]. However, the present landscape has seen a remarkable transformation. Today, we are actively exploring the potential of gold nanoparticles to aid in radiotherapy, marking the beginning of an exciting journey filled with the promise of unveiling new perspectives and invaluable insights.

Chapter 2

Ionizing radiation

Ionizing radiation can be classified into two types, both of which result in the excitation or ionization of atoms. What distinguishes these categories is the presence or absence of charge. On one hand, we have ionizing radiation composed of charged particles, including light particles like electrons and positrons, as well as heavy elements such as protons, α particles, deuterium, and tritium. These particles directly transfer their energy to matter through Coulomb interactions along their path. In the other type, that of uncharged particles, like photons and neutrons, they indirectly transfer their energy to the charged particles which then ionize the medium.

A very important quantity that helps to quantify the interaction of ionizing radiation with matter is *cross section* (σ, generally in cm^2), which can be defined in terms of atomic cross section or macroscopic cross section.

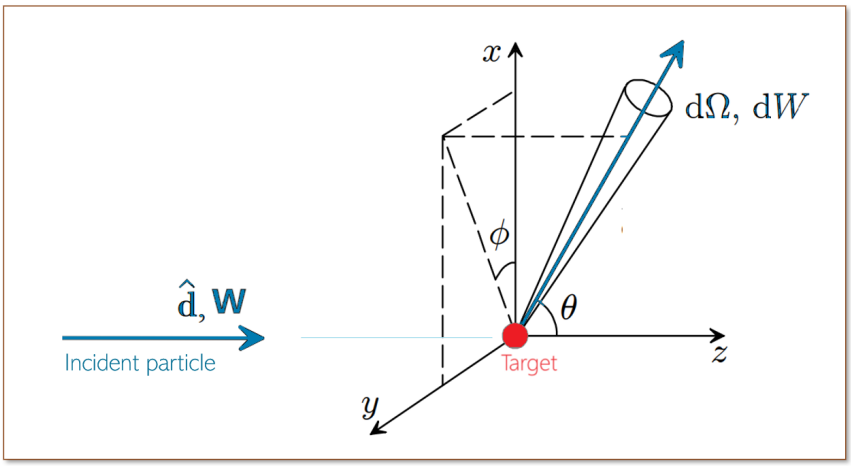

FIGURE 2.1: The change in direction and energy of a particle following its collision with a target (adapted from [8]).

When a monoenergetic beam, with energy W, is emitted in a direction $\hat{d}$ and hits a target, the incident particle lose a certain energy dW and is deflected, as illustrated in Figure 2.1. The deflection depends on the solid angle $d\Omega$, that is formed by the polar angle between the direction of the incident particle before and after the interaction (θ) and the azimuthal angle (ϕ). If a detector is placed at a macroscopic distance from the target, in order to cover the deflection region, it is possible to count the number of particles that have lost energy between W and dW [8]. This count depends on the number of incident particles per unit time and per target unit area ($\dot{N}_{in}$). Thus, the number of particles detected per unit of time is given by equation 2.1.

$$\dot{N}_{det} = \frac{d^2\sigma}{d\Omega dW}\,\dot{N}_{in}\,d\Omega\,dW \tag{2.1}$$

This equation takes into account the double differential cross section defined as the probability of scattering into a given solid angle $d\Omega$, losing a given energy dW. This quantity, integrated twice, gives the total cross-section (σ) of a specific phenomenon:

$$\sigma = \int_0^E \left(\int_\Omega \frac{d^2\sigma}{d\Omega dW} d\Omega \right) dW \tag{2.2}$$

Geometrically, the total cross section gives the area of a plane surface that, when placed perpendicularly to the incident beam, is crossed by the same number of projectiles that undergo interactions with any angular deflection and energy loss [8]. The data provided in literature tables typically represent the values of the differential cross section (DCS), corresponding to the term enclosed in parentheses in equation 2.2. It should be noted that the characteristic angles of the deflection, θ and ϕ, are both random variables whose probability distribution function (PDF) are defined by the molecular DCSs.

Another crucial quantity is the mean free path (MFP), which represents the average distance traveled by the incident particle before it loses all of its energy. To compute the probability $p(s)$ of an interaction occurring in the range $[s, s + ds]$, two separate events must be contemplated (Table 2.1).

Event 1	Event 2
The particle travels a distance s without interacting with the medium. Any interaction occurs at $s' > s$ with probability: $p_1 = \int_s^\infty p(s')\, ds'$	A particle interacts with a target in an homogeneous medium with density ρ at the interval ds. Considering $N = \frac{N_A}{A}\rho$, where N_A is the *Avogadro constant* and A is the *molar mass*, the probability of interaction per unit length is: $p_2 = N\sigma$

TABLE 2.1: Events that must be considered during the calculation of the interaction probability.

The required parameter $p(s)$ is obtained by multiplying the probabilities of both events. Assuming that the probability of a particle traveling a long distance without interacting is zero (p(∞)=0), the integral yields the exponential law of attenuation [8].

$$p(s) = N\sigma \ \exp(-sN\sigma) \tag{2.3}$$

Given the probability of an interaction occurring in the range $[s, s + ds]$, the average free path is easily calculated:

$$< s >= \int_0^\infty s\ p(s)\ ds = \frac{1}{N\sigma} \tag{2.4}$$

For electrons, this amount has values of the order of 10^{-6} cm, but for photons, depending on their energy, free paths are observed in the tens of centimeters. This discrepancy is due to charge differences, as the photon track is unaffected by Coulomb forces and rarely interacts with atoms. On the other hand, a charged particle interacts aggressively with matter, losing energy. This energy loss can be described as being gradual since most inelastic processes result in the transfer of a negligible fraction of the kinetic energy, i.e., it can be regarded in the sense of "continuous slowing down approximation" (CSDA) [9].

The macroscopic cross section of uncharged particles is specified by a parameter known as the linear attenuation coefficient: $\mu = N\sigma$. The tabulated data are reported in the literature in terms of the **mass attenuation coefficient** ($\frac{\mu}{\rho}$, generally in $cm^2\ g^{-1}$), that is affected by incident energy, just as σ is.

$$\frac{\mu}{\rho} = \sigma\frac{N_A}{A} \tag{2.5}$$

Although attenuation coefficients and MFPs can be used to characterize charged-particle interactions, the very high density of charged-particle interactions permits a more realistic approach. When slowing down, each electron experiences an enormous amount of interactions, allowing the dissipation to be calculated with the concept of **stopping power**,

which considers the energy loss per unit path length. This formulation considers the sum of two different ways of losing energy and transferring it to other particles. In the case of electrons Coulomb interaction with the nuclei of the absorber, some of the kinetic energy will be transferred to photons, resulting in a **radiation** loss. Otherwise, if the electrons interact with orbital electrons of the absorber, transferring them energy through impact excitation and ionization of absorber atoms, a **collision** loss will occur. In both of these processes, the average energy loss per unit length, experienced by the incident charged particle, can be calculated. Equation 2.6 represents the mass stopping power, which values are more frequently presented in literature. It can be seen that two parcels are considered, one for the radiation stopping power and another for collision stopping power*.

$$\frac{1}{\rho}S_{tot} = -\left(\frac{dE}{\rho ds}\right)_{rad} - \left(\frac{dE}{\rho ds}\right)_{col} \tag{2.6}$$

The stopping power can be utilized to compute the distance required to decelerate an electron to a specific energy level. This distance is referred to as the continuous slowing down approximation range, denoted as R_{CSDA}, and is determined by Equation 2.7.

$$R_{\mathrm{CSDA}} = \int_{E_0}^{E_{\max}} \frac{dE'}{S_{tot}(E')} \tag{2.7}$$

A related quantity is the linear energy transfer (LET), which is the energy transferred per unit length of the track. The LET of charged particles in a medium relates to the collision stopping power because it accounts for the average energy locally imparted to the medium. This value represents an average quantity because, at the microscopic level, the energy per unit length of the particle's path varies across a broad range. Nevertheless, it proves valuable in characterizing different types of radiation. It should be noted that the higher the energy of a certain type of charged particle, the lower the LET and, therefore, the lower its biologic efficacy [10].

In the following sections, the main processes of interaction between matter and ionizing radiation (specifically electrons and photons) are briefly described, as well as a brief summary of radiobiology and the main concepts of dosimetry.

*Also named ionization or electronic stopping power.

2.1 Photon interactions

Photons have the ability to interact with atoms within the medium through interactions either with the atomic nucleus or the orbital electrons. In the former case, these interactions may lead to processes such as photo-disintegration or pair production. In the case of second interactions, it is crucial to assess whether electrons are highly bound or can be regarded as free. The binding energy (E_B) of the electron to the atom establishes this division: if E_B is low in comparison to the energy of the photon, the electron qualifies as free; otherwise, it is a tightly bound electron.

Figure 2.2 illustrates the predominance of the three most relevant photon interactions in energy deposition, for the various atomic numbers.

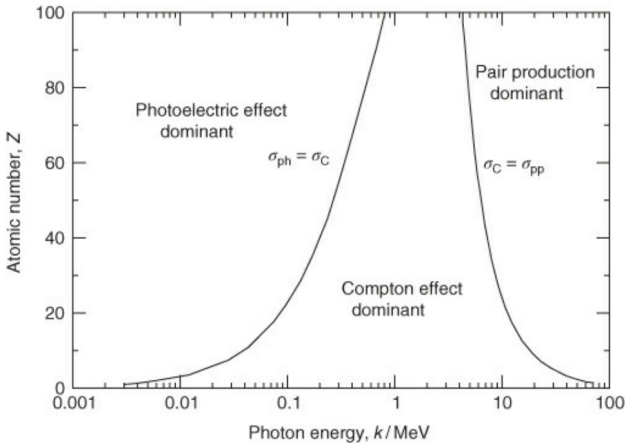

FIGURE 2.2: Predominant photon interaction in energy deposition, where k represents the photon's energy in units of the electron rest energy [11].

It should be emphasized that although the interactions depicted above imply significant energy losses, there are also elastic collisions* between photons and matter.

2.1.1 Rayleigh scattering

An example of an elastic interaction between a photon and a bound atomic electron is called Rayleigh diffusion. This process was presented by the physicist John W. Rayleigh [7] in 1900 and is characterized by the absence of excitation or ionization of the atom. This process is called "coherent" because it arises from the interference between secondary electromagnetic waves coming from different parts of the atomic charge distribution, that is, the photon is scattered by the combined action of the whole atom. The absence of

*By definition, elastic interactions are those in which the initial and final quantum states of the target atom are the same, normally the ground state [8].

ionization is due to the passage of photons with negligible energy losses, where the atom as a whole absorbs the transferred momentum but its recoil energy is very small. This is therefore an elastic scattering event because the deflected photon has the same energy as the incident photon and its scattering angle is very small. The atomic cross section for this phenomena is proportional to Z^2, meaning that this event occurs predominantly for absorbers of high atomic number. Besides, it has more practical importance at low energies, partly because the scattering angle is greater.

Rayleigh cross sections for scattering on molecular structures cannot be well approximated by an independent atom model because the electronic configuration in a molecular structure is very different from that in an atomic structure [11]. Thus, the differential atomic cross section corresponds to the electronic cross section ($_e\sigma$) differential in solid angle with a correction that accounts for the electron density spatial distribution, know as atomic form factor ($F(\mathbf{q}, Z)$).

$$\frac{d_a\sigma_R}{d\Omega}(\theta, Z) = \frac{d_e\sigma_R}{d\Omega}(\theta)|F(\mathbf{q}, Z)|^2 \tag{2.8}$$

The form factor depends on the atomic number, Z, and on the momentum transfer, $\mathbf{q}$. Assuming that the photon preserves its energy E after the collision:

$$|\mathbf{q}| = |\mathbf{p} - \mathbf{p}'| = \frac{2E}{c}\ \sin\left(\frac{\theta}{2}\right)$$

This expression is approximately valid only for photons with energy well above the K absorption edge. This approximate method is sufficient for most applications because, at the energies where anomalous scattering effects become significant, coherent scattering has a very low probability.

Because radiation therapy entails transferring the energy of incoming particles into biological tissue, this particular phenomenon is not considered significant.

2.1.2 Photoelectric Effect

The photoelectric effect is the most important interaction of low-energy photons with matter with low Z [9]. It occurs when a photon, with energy E_i, interacts with a tightly bound electron, such as those in the inner shells of an atom.

In this process, the incident energy is completely absorbed and the result is an ejected electron with a velocity v_e. For this to happen, the incident photon must be more energetic

than the binding energy of the atomic electron shell. If so, the difference between those energies* corresponds to the kinetic energy of the photoelectron emitted ($T_e = E_i - E_B$). In fact, when the incident energy exceeds the K-shell binding energy, about 80% of all photoelectric absorptions occur with the K-shell electrons of the absorber and the remaining 20% occur with less tightly bound higher shell electrons [7].

The direction in which the photoelectron is emitted, compared to the direction of the absorbed photon, is determined by the polar angle θ and azimuthal angle ϕ. If the incident photon is unpolarized, the angular distribution of photoelectrons is not affected by ϕ, which is uniformly distributed in the range $(0, 2\pi)$ [8]. Occasionally, introducing a variable $\nu = 1 - \cos(\theta)$ seems to be advantageous.

The basic theory of the photoelectric effect is based on the assumption that the interaction between the atom and the electromagnetic field associated with the incident photon is weak, and, to a first order, can be treated as a perturbation. Assuming that the photon energy is much larger than the binding energy but non-relativistic ($E_B \leq E_i \leq m_e c^2$) and considering Fermi's golden rule to determine the transition rate for the photoelectric process [11], it yields that cross section is proportional to the first term in equation 2.9.

Then, including an additional relativistic correction term in square brackets, the angular distribution of the photoelectric cross section is given by:

$$\frac{d\sigma_{Ph}}{d\Omega} \propto \frac{Z^5 \beta^4 \sin^2\theta}{(1-\beta\cos\theta)^4}\left[1 + \frac{1}{2}\gamma(\gamma-1)(\gamma-2)(1-\beta\cos\theta)\right] \tag{2.9}$$

$$\beta = \frac{v_e}{c}\ ;\ \gamma = \frac{1}{\sqrt{1-\beta^2}}$$

The angular distribution of photoelectrons is influenced by the energy of the incoming photon. For energies around 10 keV, photoelectrons are generally emitted at angles close to 90° relative to the direction of the incident photon [7]. As the incoming energy increases, the peak of photoelectron emission gradually shifts towards more forward angles. Occasionally, defining a variable $A = \frac{1}{\beta} - 1$ can be useful.

2.1.3 Compton Scattering

The interaction of a photon with a loosely bound orbital electron is known as Compton scattering, after Arthur Compton [7]. This event causes the incident photon, with energy

*Actually, the atom will gain a finite kinetic energy but it is negligible because the mass of the nucleus is much larger than of the electron.

$E_i = h\nu$, to deviate from its initial route. The transferred energy causes a recoil electron that is released from the atom with kinetic energy E_K, resulting in a scattered photon with energy $E_C = h\nu'$.

Although electrons occupy different atomic energy levels, which means they are in motion and bound to the nucleus, for the Compton effect it is assumed that the electron interacting with the incoming photon is typically unbound and stationary at the outset. Thus, before the impact, the electron does not have kinetic energy and the collision can be represented by the figure below:

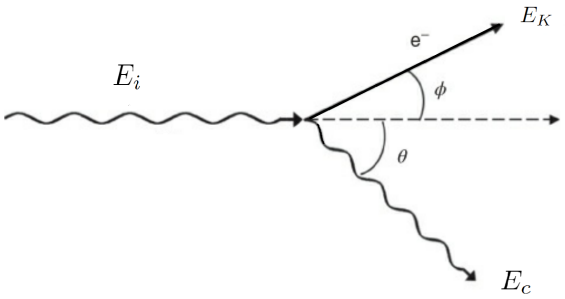

FIGURE 2.3: Schematic representation of the Compton scattering [7].

The solution to the collision kinetics of the Compton scattering is based on the conservation of both energy and momentum in the next equations, where p_e is the relativistic momentum of the recoil electron *.

$$\begin{cases} E_i + m_e c^2 = E_C + m_e c^2 + E_K \\ \frac{E_i}{c} = \frac{E_C}{c}\cos\theta + p_e \cos\phi \\ 0 = -\frac{E_C}{c}\sin\theta + p_e \sin\phi \end{cases}$$

These three equations, through some algebraic manipulation, enable the determination of the energy of the scattered photon given its deflection angle and the incident energy.

$$E_C = \frac{E_i}{1 + \frac{E_i}{m_e c^2}(1 - \cos\theta)}$$

*The electron is ejected with total energy that is considered relativistic: $E_e = \sqrt{(m_e c^2)^2 + p_e^2 c^2}$

The Klein–Nishina formulation (KN) provides the differential cross section (DCS) for Compton scattering by a stationary free electron. Although this fundamental DCS was once widely employed in certain radiation transport algorithms, it proves to be a limited approximation for photon–atom Compton interactions. In practical terms, atomic electrons are not at rest but possess a momentum distribution, resulting in the Doppler broadening of the Compton line, an effect accounted for in the so-called impulse approximation. The DCS is calculated by assuming that electrons in the i-th subshell have a momentum distribution. The active target electron is ejected to a free state after a Compton interaction with the i-th subshell, leaving the atom in an excited state with a vacancy. Thus, the effect of electron binding may be included, which asserts that Compton excitations are permitted only if the energy transfer is greater than the binding energy of the active subshell. Therefore, the atomic DCS is given by the KN formula, corrected by a factor S, known as the incoherent scattering function in the impulse approximation[12] that accounts for Doppler broadening and binding effects [8]:

$$\frac{d\sigma_C}{d\Omega} \approx \frac{r_e^2}{2}\left(\frac{E_C}{E_i}\right)^2\left(\frac{E_C}{E_i}+\frac{E_i}{E_C}-\sin^2\theta\right)S(E_i,\theta) \tag{2.10}$$

It is worth noting that a large part of the energy region of radiation used in medical applications is dominated by Compton scattering.

2.1.4 Pair production

A pair production process consists in a complete absorption of a photon by the atom forming an electron/positron pair. In order to conserve linear momentum simultaneously with total energy and charge, this phenomena can only occur in the presence of a Coulomb field, that is commonly created by an atomic nucleus, with rest energy $m_A c^2$. It can also arise, with lower probability, in the field of an atomic electron, originating a process called "triplet production" because the creator of the Coulomb field gains a large amount of kinetic energy.

In contrast to other photon interactions, there is a well-defined threshold energy below which the pair production cannot happen, based on the invariant $E^2 - p^2c^2$ before and after the interaction. The values for the nuclear pair production (NPP) and triplet production (TP) are:

$$\begin{cases} E_t^{NPP} = (1.022\ \text{MeV}) \times \left(1 + \frac{m_e c^2}{m_A c^2}\right) \\ \\ E_t^{TP} = 2.044\ \text{MeV} \end{cases}$$

After the interaction, the photon loses its energy and an electron with energy E_- is created. The reduced energy ϵ is the fraction of the photon energy that is taken away by the electron, that is: $\epsilon = \frac{E_- + m_e c^2}{E}$

The Bethe–Heitler (BH) differential cross section accounts for the integrals that involve the atomic form factor and assumes that the Coulomb field of the nucleus is exponentially screened by the atomic electrons. Furthermore, the dependence of the triplet cross section on the reduced energy, ϵ, is assumed to be the same as that of the pair cross section. Actually, the triplet contribution (η) varies with the photon energy and increases monotonically, reaching a saturation value, η_∞, at high energies [8]. However, the BH expression fails at low energies, where it systematically underestimates the total cross section. Therefore, it becomes necessary to introduce an empirical correction term. The differential cross section can be expressed in the following simplified form:

$$\frac{d\sigma_{PP}}{d\epsilon} \propto \frac{2}{3}\left[2\left(\frac{1}{2} - \epsilon\right)^2 \phi_1(\epsilon) + \phi_2(\epsilon)\right] \tag{2.11}$$

Functions ϕ_1 and ϕ_2 account for correction factors that depend on the atomic number, the atomic form factor, the "reduced energy", and the incident photon energy. The energy distribution and angular distribution of electrons and positrons in pair production are complex functions of the incident photon energy and the absorber atomic number [7]. With increasing incident photon energy the distribution of charged particles is peaked increasingly in the forward direction.

2.2 Electron interactions

As previously observed, some interactions between photons and matter lead to the ejection of orbital electrons, which may possess enough kinetic energy to interfere with the surrounding medium. In this manner, charged particle Coulomb-force interactions can, in a simplified classical view, be characterized based on the relationship between the *atomic radius* (r_a) and the *impact parameter* * (b). It is important to note that this characterization

*The impact parameter is defined as the perpendicular distance between the velocity vector of a projectile and the center of the target [13].

is not allowed in a quantum mechanical formulation, in which the uncertainty principle limits the localization of a particle with well-defined momentum [11]. In summary, the following cases are considered:

- $b \approx r_a$

  In this situation, "hard" inelastic collisions take place. The incoming particle primarily interacts with a single atomic electron (often from internal shells). The energy transferred is greater than the binding energy of the orbital electron, hence it is ejected with high speed. As a consequence, there is an emission of $delta$ rays, also known as "knock-on" electrons [7],

- $b >> r_a$

  Due to the charged particle's interference with the whole atom, this condition results in a "soft" inelastic collision, characterized by the excitation or ionization of matter. Although the energy transferred to a particular orbital electron is very small, this type of interaction is one of the most frequent [11], constituting almost half of the energy delivered to the medium.

- $b << r_a$

  In this case, an elastic interaction usually occurs without excitation or ionization. In reality, there is a certain energy transfer to the target, but the average energy lost by the projectile is a very small fraction of the initial energy because of its insignificant mass compared to the target. Consequently, energy loss and target recoil are neglected [8]. The Coulomb field generated by the incident particle acts mainly on the nucleus, that is, the electrical field of the core is the most relevant effect on the deflection of the initial trajectory. Thus, in the presence of atoms with high Z values, this kind of interaction explains the usual sinuosity of electronic trajectories.

  However, when $b << r_a$, a small percentage of interactions may be inelastic. One such case consists of the disturbance generated by Coulomb fields, which cause a deceleration of the incident charged particle, emitting a Bremsstrahlung photon (explained in section 2.3). Another example of inelastic interaction is the annihilation of a positron by colliding with a resting electron in the medium, generating two photons in opposite directions [11].

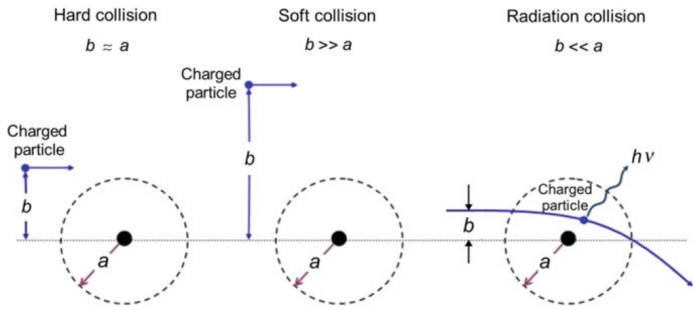

FIGURE 2.4: Interactions between electrons and atoms for different impact parameters [7].

2.2.1 Atomic relaxation

Ionizing radiation frequently excites atoms when it interacts with matter. However, because these excited states are transient, the atom usually relaxes to recover its balanced energy. These processes often involve the release of energy while the atom reorganizes itself, causing an electron from a higher atomic shell to occupy the space left by one from a lower one. The difference between the binding energies of the initial and final shells is transmitted by means of radiative and non-radiative mechanisms.

When a photon is emitted with energy corresponding to the difference in orbital levels, it results in fluorescence. This is a radiative mechanism that releases characteristic X-rays. Conversely, if the energy between the two energy levels is transferred to a less tightly bound orbital electron, it is ejected. This non-radiative process is known as the Auger effect. This terminology is a generalization because, in reality, there are three distinct phenomena, as depicted in Figure 2.5. In the so-called Auger effect, the primary transition takes place between two electron shells, and the energy is transferred to an orbital electron within the initial or upper shell. When the primary transition occurs between sub-levels, we observe the Coster–Kronig effect, where the energy is transferred to an electron in a different shell, or the super Coster–Kronig effect, where the energy is transferred to an electron within the same sub-level where the initial transition occurred [7].

The amount of energy released via radiative or non-radiative methods is determined by the shells or subshells involved and thus depends on the atomic number. In the case of Compton effect or inelastic collisional interactions, gaps are created predominantly in the outer layers [11]. On the contrary, when the photoelectric effect occurs, the probability of gaps forming in the inner layers increases with the atomic number.

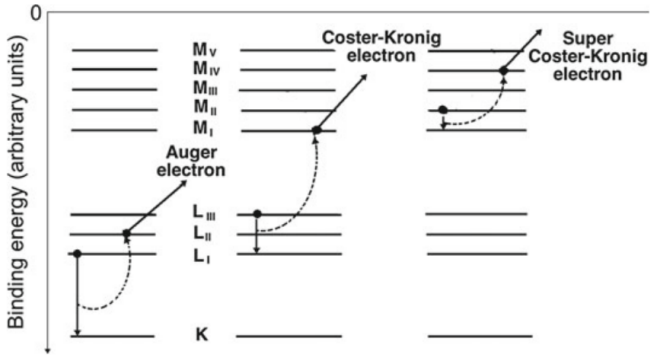

FIGURE 2.5: Non-radiative processes caused by atomic relaxation phenomena [7].

2.3 X-ray source

The energy spectrum of the particles must be provided as an input to the source model in order for the program to calculate the physical parameters according to the correct energy range. In this section, there is a brief overview of the process of X-ray production in a tube since the primary particles considered in this study are generated from the output spectra of this type of device.

X-rays are released when very energetic electrons make contact with matter and convert their kinetic energy into electromagnetic radiation. An apparatus that performs this function is made up of an electron source, an evacuated channel for electron acceleration, a target electrode, and an external energy source to accelerate the electrons [14]. An example of this type of device is schematized in Figure 2.6.

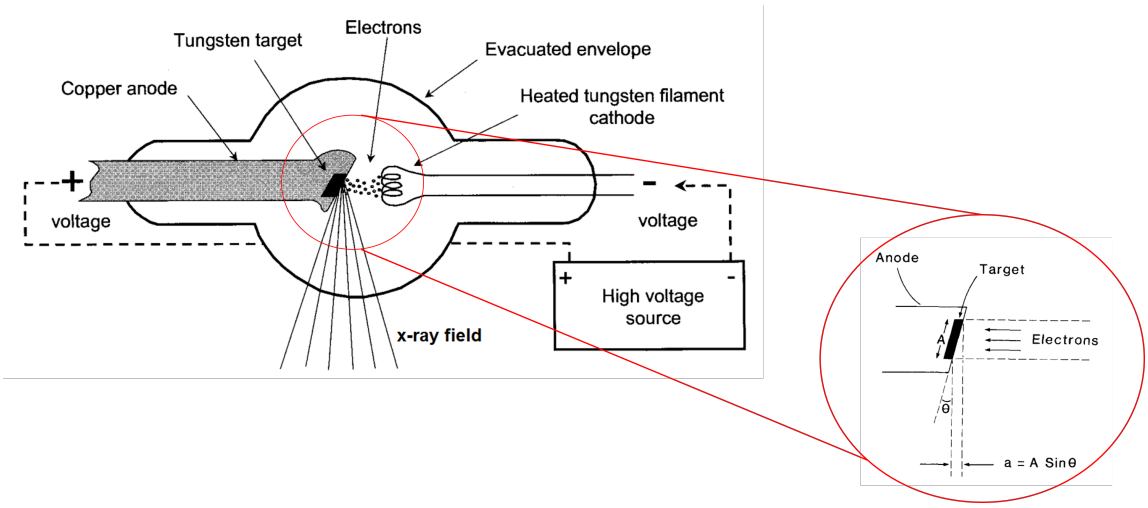

FIGURE 2.6: Schematic representation of an X-ray tube [15], with a zoom within the red circumference [14] in order to understand the *line focus principle*

The cathode, which is made up of a wire filament and a negatively charged focusing cup, is the source of electrons in the X-ray tube. When the tungsten filament is heated, electrons are emitted, a process known as thermionic emission. The function of the cathode cup is to direct the electrons toward the anode, a metallic target electrode, so that they hit the target in a well-defined area known as the focal spot [15].

Electrons liberated from the filament traverse the vacuum within the X-ray tube as the anode is maintained at a positive potential relative to the cathode. Prior to reaching the target, these electrons move at high velocities, and their kinetic energy escalates linearly with the potential difference existing between the cathode and anode. When these electrons make contact with an object, their kinetic energy undergoes transformation into various forms of energy.

Most interactions result in undesired heat through small collisional energy exchanges with target electrons. As a result, the anode in the X-ray generator produces a lot of heat while producing the required number of X-rays for acceptable image quality [14]. The target material is often tungsten because of its high melting point (3370 °C) and high atomic number (Z = 74), which permits significant heat deposition without cracking of its surface and prevents heat damage to the X-ray tube ([15]). A crucial component of anode design is also determining the ideal target region size from which the X-rays are emitted. The focal should be as small as possible to create sharp radiographic images but smaller focal spots generate more heat per unit area of target, restricting currents and exposure. Therefore, there are techniques that may be utilized in diagnostic X-rays to reduce the temperature of the target at any location.

One of these strategies is the use of rotating anodes, which allow greater heat loading and consequently higher X-ray production capabilities. Using this method, electrons transfer their thermal energy to a continually revolving target, dispersing the heat over a large surface and a large mass of anode disk [14].

Another strategy to avoid the increase in temperature of the target is to reduce the apparent size of the focal spot [15], known as the *line focus principle*. This principle distinguishes between actual and effective focal spot sizes: the former is the area (**A**) of the anode hit by electrons, which is determined by the length of the cathode filament and the width of the focusing cup slot; the latter is the area (**a**) of the focal spot projected down the central ray in the X-ray field [14]. Normally, the target is mounted on a steeply inclined surface of the anode, which is characterized by an angle θ. The anode angle causes the

effective focal spot length to be smaller than the actual focal spot length, as illustrated in Figure 2.6. Thus, **a** may be decreased to a desirable size by making the target angle θ small.

Although there are mechanisms for dissipating heat over the anode, electromagnetic radiation emission only accounts for a small percentage of the energy (typically less than 1%). These released rays are caused by the electron–photon cascade process, which is activated by incident electrons entering the target [16]. There are two different mechanisms by which X-rays are produced. Radiation can be emitted as a consequence of Coulomb interactions with target atoms (bremsstrahlung) or by fluorescence after atomic ionization through electron impact or photon interactions (characteristic X-ray emission). Both of these processes were indicated in Section 2.2, but now will be presented in more detail.

An electron occasionally comes into contact with a positively charged nucleus in the target electrode. Whenever an electron with its corresponding electromagnetic field passes near a nucleus, it experiences an abrupt deflection and deceleration. As a consequence, a portion or all of its energy is dissociated from it and propagates in space as electromagnetic radiation named bremsstrahlung (a German word that translates to "braking radiation" [14]). The energy of the incoming electron dictates the direction and energy of the resulting X-rays. Due to the possibility of one or more bremsstrahlung interactions, each of which can result in a partial or complete depletion of the electron's energy, the resulting X-ray can exhibit energies ranging up to the initial energy of the electron [15]. However, the probability of an electron hitting a nucleus is incredibly low since it constitutes a very small percentage of the atom's volume and the nuclear cross section is very small. Therefore, the subatomic distance between the bombarding electron and the nucleus determines the energy lost by each electron throughout the bremsstrahlung process, because the Coulomb force of attraction increases with the inverse square of the interaction distance [14]. An electron's kinetic energy is completely lost when it collides with the target nucleus, resulting in the maximum X-ray energy. Higher energy X-rays approximately drop linearly with energy up to the maximum energy of the incident electrons, while lower-energy X-rays are more abundant.

On the other hand, the emitted radiation may have discrete energies that are specific to an element, hence the term characteristic X-rays. This type of radiation is produced by fluorescence, that is, when an atom has a vacancy in one of its inner shells and relaxes from its excited state through a radiative transition. Atomic shell vacancies are created

in an X-ray tube target as a result of two forms of particle–atom interactions: inner-shell impact ionization, where an electron penetrating the anode knocks out an inner-shell electron in an inelastic hard collision, and photon–atom interactions, which occur when a bound electron is ejected in a photoelectric absorption or Compton scattering of a generated bremsstrahlung photon [16]. When a vacancy occurs in an orbit, the empty shell becomes energetically unstable, causing an outer orbital electron to fall down to replace it. As this electron transitions to a lower energy state, the difference between the binding energies of the electron shell can be released as a characteristic X-ray photon. The characteristic radiations released by higher atomic number targets and transitions involving inner shells such as K, L, M, and N have high enough energy to be recognized in the X-ray region of the electromagnetic spectrum [15]. Because the two types of interaction processes that create fluorescence are fundamentally different in that they are triggered by charged (electrons) or uncharged (photons) particles, the spatial distributions of X-ray fluorescence in the anode are distinctively different. In the case of impact ionization, the fluorescence is restricted to penetration depths where the electrons retain enough of the incident kinetic energy to exceed the inner shell ionization threshold. In contrast, because of the long mean free path length of bremsstrahlung photons, X-ray fluorescence following ionizations due to photon interactions penetrates much deeper into the target [16]

Bremsstrahlung and characteristic X-rays thus distinguish between two different energy emissions: the first process produces a broad spectrum limited by the energy of the incident particle and the last phenomenon creates discrete peaks that correspond to the binding energies of the atom. However, as shown in Figure 2.7, the output of an x-ray spectrum also truncates low energies. This is because, despite the abundance of low energy X-rays in the bremsstrahlung spectrum, filtration prevents their emission.

Filtration is the removal of X-rays as the beam passes through a layer of material [14] and can occur due to the glass or metal insert at the X-ray tube port (inherent filtration). Since the lower-energy radiation is the least penetrating, it is removed from the beam more quickly [17]. It can also be filtered through sheets of metal intentionally placed in the beam to vary its effective energy. In general diagnostic radiology, added filters attenuate low-energy X-rays, enriching the beam with higher-energy photons. The transmitted beam hardens as the filtration increases, resulting in higher average energy and more penetrating force. Consequently, using filters to absorb these X-rays instead of exposing the

patient to them serves to minimize dose while enhancing the beam's penetration capacity. As the overall beam intensity decreases with greater filtration and rises with voltage, it is imperative to find the right combination of voltage and filtration to achieve the desired beam hardness [15]. Additionally, the choice of an appropriate filter holds crucial significance in the operation of an X-ray machine, as it provides a means to reduce the intensity of X-ray photons that would not contribute to the image. On rare occasions, it may be desired to eliminate the high-energy component of the spectrum, but this is a more challenging operation because the linear attenuation coefficient of all materials decreases with increasing energy. In addition, because materials are generally transparent to their own characteristic radiation, the effect of filtering may be rather striking when the filter is made of the same material as the target anode emitting the X-rays [17].

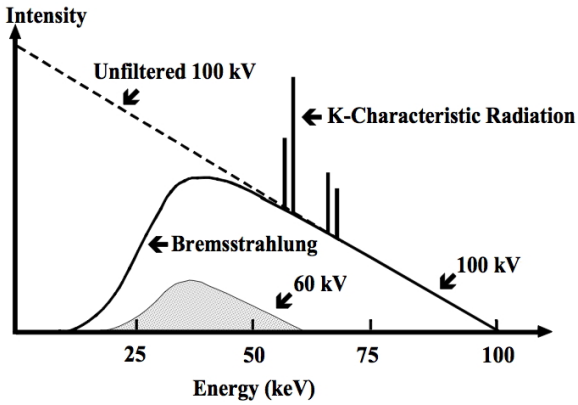

FIGURE 2.7: spectrum[18]

As represented above, if no filtration, inherent or added, of the beam is assumed, the calculated energy spectrum will be a straight line, whose equation is given by:

$$I_E = KZ(E_m - E)$$

This is known as the Kramer's equation [15], where I_E is the intensity of photons with energy E, Z is the atomic number of the target, E_m is the maximum photon energy, and K is a constant. It is clear that, if $E = E_m$, the intensity of photons will be zero, confirming that a bremsstrahlung photon has energy less than or equal to the energy of the incident electron. Hence, the unfiltered bremsstrahlung spectrum exhibits a ramp-shaped correlation between the quantity and the energy of the generated X-rays, where the peak voltage (kVp) applied to the X-ray tube determines the highest X-ray energy. When filtration is employed, lower-energy X-rays are selectively absorbed, resulting in an

average X-ray energy that is roughly one-third to one-half of the maximum X-ray energy present in the spectrum [14].

2.3.1 SpekPy

The SpekPy toolkit is available for free under the MIT software license. The model accesses data using empirical normalizations and assumes a uniform angular distribution for bremsstrahlung emission. Furthermore, when calculating the X-ray contribution using simple semi-empirical models, the model does not exclude the characteristic emissions by the target. The National Institute of Standards and Technology (NIST) tabulations are the source for the default photon coefficients (both for mass attenuation and mass energy absorption).

It is essential to use the standard NumPy and SciPy Python libraries because of their easy compatibility with the Python programming language. Furthermore, the "Matplotlib" package can be helpful in visualizing results effectively. Communication with the toolkit is based on command inputs present in Appendix B.1. The toolkit's main class is Spek. The user creates instances of that class, each representing a separate X-ray tube. There are several keyword parameters that may be used when constructing a specific spectrum. With the extra tools supplied, it is possible to filter X-ray spectra, compute alternative X-ray beam metrics, create new materials, and save SpekPy states.

The Diagram 2.8 presents a succinct illustration of the process for creating a simple X-ray spectrum, leading to a graphical representation similar to the one portrayed in Figure 5.7. Initially, the **spekpy** package is imported; then, the spectrum is generated with the necessary specifications and filtration, and finally, the fluence is calculated alongside the energy bins.

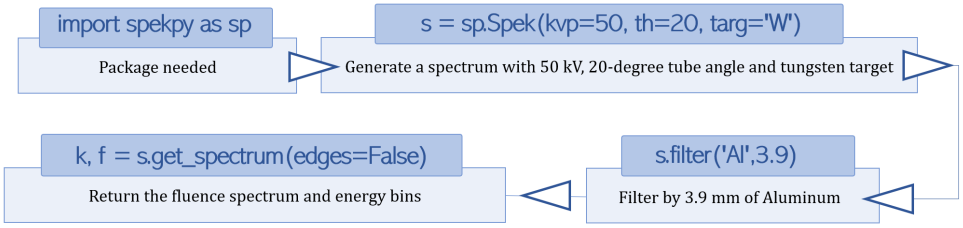

FIGURE 2.8: Diagram illustrating the process of generating an X-ray spectrum using the SpekPy package in the Python programming language.

2.4 Dosimetry

In nature, many physical processes are considered random because the position and time of a specific particle interaction can't be anticipated. Contrarily, when considering radiation interactions, since there are numerous particles present, the spatial and temporal dimensions of interest allow for a huge number of processes that can be characterized in terms of mean or expectation values. Thus, at the macroscopic level radiation interactions are well approximated by non-stochastic descriptions, where the quantities can be predicted by calculations based on a "point function" defined in an infinitesimal volume [9]. When considering radiation fields, it is assumed that a large number of particles is involved and particle interactions have well-defined probability distributions. Dosimetric quantities describe the amount of energy the radiation beam deposits in a given medium and, most of the times, they are calculated using radiometric quantities and interaction coefficients [7].

2.4.1 Radiometric quantities

Radiation fields can be simply described by non-stochastic quantities that consider the number and energy of particles constituting the radiation beam, known as radiometric quantities.

One important radiometric quantity is **particle fluence** (ϕ), which accounts for the expectation value of the number of particles dN striking a finite sphere during a time interval. If the sphere is reduced to an infinitesimal with a cross sectional area of dA, the particle fluence is given by the expression below, for all values of t through the time interval:

$$\phi = \frac{dN}{dA} \tag{2.12}$$

Furthermore, there is a simple field-descriptive quantity which takes into account the energies of the individual rays, called **energy fluence (ψ)** [9]. Considering R as the expectation value of the total energy (excluding rest energy), sometimes called "radiant" energy, of the incident particles striking a sphere with cross-sectional area dA, energy fluence is given by:

$$\psi = \frac{dR}{dA} \tag{2.13}$$

Sometimes, it is useful to use particle fluence rate ($\dot{\phi}$) and energy fluence rate ($\dot{\psi}$), defined as the ratio $d\phi/dt$ and $d\psi/dt$, respectively.

2.4.2 Interaction coefficients

Radiation field quantities fall naturally into pairs, because there are always two different entities referring either to the number of particles or the energy transported by them. Interaction coefficients can be defined, considering this pairing.

For photons, two important interaction quantities are defined using the concept of mass attenuation coefficient, referred to in Chapter 1. Considering $\bar{E}_{tr}$ as the mean energy transferred from incident photon to charged particles averaged over all possible photon interactions, it is possible to express the mass energy transfer coefficient (μ_{tr}) for an absorber material of density ρ and for incident uncharged particles of energy E_i:

$$\frac{\mu_{tr}}{\rho} = \frac{\mu}{\rho}\frac{\bar{E}_{tr}}{E_i} \tag{2.14}$$

When charged particles come to rest in the medium, a typical percentage of their kinetic energy (and any secondary charged particles created by them) is lost in radiative processes such as bremsstrahlung, fluorescence, and annihilation in flight. This means that, to a first approximation, a fraction of the radiative energy can be thought of as escaping the local volume, resulting in energy not locally absorbed. Considering $\bar{g}$ as the radiation yield averaged over the spectrum of energies of the charged particles liberated by monoenergetic photons [11], the mass energy-absorption coefficient is defined by equation 2.15.

$$\frac{\mu_{ab}}{\rho} = \frac{\mu_{tr}}{\rho}(1-\bar{g}) \tag{2.15}$$

For electrons, the most important interaction coefficient is the mass stopping power, already defined in this chapter. The collision term has a greater impact since it involves more energy transfer. This term represents the average rate of energy loss experienced by a charged particle in both hard and soft collisions. Hard collisions may produce sufficiently energetic rays that transport their kinetic energy further away from the primary track. Hence, the mass collision stopping power will overestimate the outcome when calculating the dose in a thin body traversed by electrons. Sometimes, it is useful to introduce the concept of restricted stopping power, which corresponds to the fraction of

the collision stopping power that accounts for collisions emitting delta rays with energy below a threshold.

2.4.3 Energy deposition

The most important quantity in radiation dosimetry is the absorbed dose, which is defined by equation 2.16a, where dE_{ab} is the mean energy imparted by ionizing radiation to a certain mass [7]. Mathematically, dose is a point quantity representing the limit of the mean specific energy as the mass tends to zero [11]. As previously stated, for photon fields, energy must be transferred from indirectly ionizing radiation to energetic electrons before the medium absorbs a fraction of the kinetic energy imparted by charged particles. This first step results in KERMA ("Kinetic Energy Released per unit MAss"), which is given by equation 2.16b. KERMA occurs at the point of interaction between the incoming uncharged particle and the absorber atom, whereas dose is distributed across a broader mass element (dm), whose size is critical. If dm is too small, there are statistical fluctuations, and if dm is too large, spatial resolution is less than optimal.

$$D = \frac{dE_{ab}}{dm} \tag{2.16a}$$

$$K = \frac{dE_{tr}}{dm} \tag{2.16b}$$

In the second phase of the dose delivery process for indirectly ionizing radiation, electrons experience repeated Coulomb interactions with the atoms of the absorber medium, gradually losing kinetic energy in two ways. As described in section 2.2, energetic secondary charged particles can interact with either the orbital electrons or the nuclei of absorber atoms. In the first case, it results in a collision loss, where energy per unit mass is called collision kerma (K_{col}) and local deposition occurs. The second scenario leads to radiation loss in the form of bremsstrahlung or photons produced by annihilation in flight of positrons, resulting in radiation kerma (K_{rad}). Therefore, total KERMA is divided into two distinct quantities that vary according to the type of energy losses suffered by electrons ($K = K_{col} + K_{rad}$). Because the collisional kerma does not account for radiative losses, there is an expression analogue with equation 2.15, resulting in:

$$K_{col} = K(1 - \bar{g}) \tag{2.17}$$

Besides, assuming that N photons of energy fluence ψ transfer a mean energy NdE_{tr}, equation 2.14 can be rearranged and divided by dm (see appendix A), yielding the expression below:

$$K = \psi \frac{\mu_{tr}(E)}{\rho} \tag{2.18}$$

According to these definitions, KERMA refers to the kinetic energy transferred to secondary electrons at the moment of release, whereas absorbed dose refers to the energy lost by electrons along their paths [11]. Though, the radiation loss is more probable to escape the volume of interest (V), not contributing to radiation absorbed dose. As a consequence, the collisional kerma equals the dose when a perfect energy balance in volume V prevails and the condition of "charged particle equilibrium" (CPE) is verified. This condition is possible when the atomic composition and density of the medium are homogeneous, when the field of indirectly ionizing radiation is uniform, and the volumes considered have a radius which is higher than the range of the secondary electrons. Under CPE, each charged particle of a given type and energy leaving volume V is balanced by a particle of the same type and energy entering, in terms of expectation values [9]. Considering expressions 2.18 and 2.17, the condition $D = K_{col}$ is then valid in CPE conditions, that is:

$$D = \psi \frac{\mu_{ab}(E)}{\rho} \tag{2.19}$$

It should be emphasized that KERMA is specified exclusively for uncharged particles. For electron fields, a quantity that might be regarded is CEMA ("Converted Energy per unit MAss"), defined by the fraction between E_{col} and dm, that is, it considers the mean energy lost in electronic interactions in a mass of a material by the primary charged particles, excluding knock-on electrons [11]. Instead of relating to attenuation coefficients, CEMA can be written in terms of the stopping power:

$$\text{CEMA} = \phi_{prim} \frac{S_{col}(E)}{\rho} \tag{2.20}$$

The unit of KERMA, dose and CEMA is J Kg^{-1}, that has the special name *Gray* (Gy).

Furthermore, equal doses of different types of radiation do not produce equal biologic effects. For example, 1 Gy of neutrons produces a greater biologic effect than 1 Gy of X-rays [10]. It is typical to use X-rays as the reference radiation when comparing other

forms of radiation. For this, it was defined the concept of relative biologic effectiveness (RBE), that corresponds to the dose ratio between X-rays and the test radiation required for equal biologic effect.

Chapter 3

Gold Nanoparticles and radiosensitizing effects

As previously stated, this work focus on a method for irradiating tumors while preserving healthy tissues. This method involves the use of "radiosensitizers", which are substances designed to increase the sensitivity of cancer cells to radiation without affecting the sensitivity of normal tissues. One of the materials often employed to achieve this goal is gold, represented in the periodic table by the symbol Au, with an atomic number of 79 and a density of 19.3 g/cm^3.

In cancer therapy applications, it has been observed that nanoparticles naturally accumulate in tumor tissues through a passive mechanism called Enhanced Permeability and Retention effect (EPR), without targeting ligands. This phenomenon is attributed to the tumor's flawed vascular system, characterized by irregular endothelium, diminished lymphatic drainage, and reduced interstitial fluid absorption. These factors collectively promote the passive retention of nanoparticles in tumor tissues [3].

Hence, the concept of Gold Nanoparticle-Assisted Radiation Therapy (GNRT) has arisen [19]. It's important to highlight that materials at the nanoscale often display unique physical and chemical properties, such as fluorescence, electrical conductivity, or chemical reactivity, that diverge significantly from their larger counterparts. For instance, gold, which typically appears yellow at its most common size, exhibits a blue color at the micrometer scale and a reddish hue when reduced to sizes below 100 nm [3].

3.1 Physics of Gold Atoms

This section explores the physics behind the interaction processes of gold with matter. Firstly, it is essential to examine the photoelectric cross-section of gold, because, as illustrated in Figure 2.2, this effect is clearly predominant for energies below 500 keV. For example, considering an incident photon with energy of 100 keV, gold has a photoelectric cross section accounting for 94% of the total cross section [20].

In order for the photoelectric effect to take place, a photon must have enough energy to overcome the binding energy of the electron in its current orbit. Without meeting this energy requirement, the electron will not be ejected. Hence, as the binding energy threshold for each subshell is reached, the emission of additional photoelectrons becomes energetically feasible. This gradual increase in excitation possibilities leads to the emergence of minor absorption peaks within the photoelectric effect cross-section of gold (Figure 3.1).

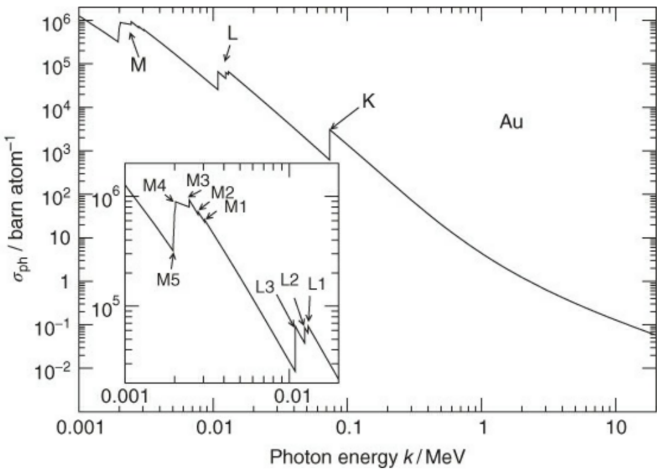

FIGURE 3.1: Cross section of Photoelectric effect as function of photon energy [11].

The noticeable discontinuities in the graph above are indicative of the specific binding energies associated with electronic shells. Interestingly, the structure of these absorption peaks bears a resemblance to the fine structure within the orbital configuration of the gold atom [11]. The photoelectric cross-section is significantly impacted by the atomic number, especially when dealing with incident energies slightly below the absorption peak energies. Consequently, nanoparticles with high atomic numbers, such as gold, facilitate more efficient energy transfer to the surrounding medium through processes like photoabsorption and subsequent electron emission, compared to substances like water. For example, when a 100 keV photon interacts with a gold atom, there is a notable likelihood of ejecting an electron from the K-shell (with a binding energy of approximately 80.7 keV), which

can travel a distance of around 9 µm in water, indicating that the photoelectron possesses enough energy to traverse a cell. Additionally, when the incident energy is 200 keV, the emitted photoelectron can travel approximately 200 µm, allowing it to traverse multiple cells [5].

If the energy of the incident photon is less than $E_B(K)$ (see Table 3.1), it can only result in the ejection of an electron from higher-energy layers. However, at lower energies, the mass absorption and attenuation coefficients for photons in gold closely resemble those for water and soft tissues. As a result, only interactions with the inner layers (K, L, M) of the gold atom contribute significantly to dose enhancement.

Shell	K	L1	L2	L3	M1	M2	M3	M4	M5	N1	N2	N3	N4	N5	N6	N7
Binding Energy (eV)	80725	14353	13734	11919	3425	3148	2743	2291	2206	762.1	642.7	546.3	353.2	335.1	87.6	84.0

TABLE 3.1: Electron binding energies for the gold element (Z=89) [21].

Examining Figure 3.2, a clear distinction between absorption and attenuation in the energy range before the K layer is evident. This difference arises because, for energies higher than this "K-edge", energy transfer primarily triggers fluorescence phenomena [5]. As mentioned in Section 2, photons interact weakly with matter, so the energy carried by fluorescence X-rays is transported away [11]. On the other hand, at energies below the peak of the K layer, interactions with incident photons primarily induce the emission of Auger electrons, i.e., they travel very short distances, and energy is deposited locally. In fact, the probability of Auger electron emission in gold increases from 4.1% (K layer) to 74.6% (L layer), reaching as high as 98.5% (M layer). In the case of gold, a fluorescence phenomenon triggered by a K layer transition gives rise to photons with a mean free path of 5 cm in tissue, whereas Auger electrons with typical energy below 100 eV have a range of 10 nm [5]. Although the behavior of low-energy electrons is not fully understood, it is established that these particles can be rapidly stopped within the nanoparticle due to its high density. Consequently, the size of a gold nanoparticle determines the number of Auger electrons that can escape self-absorption and release their energy into the surrounding medium [5]. Furthermore, Auger electrons demonstrate a relatively high average energy deposition per unit distance traveled, leading to an increased radiobiological effect [11].

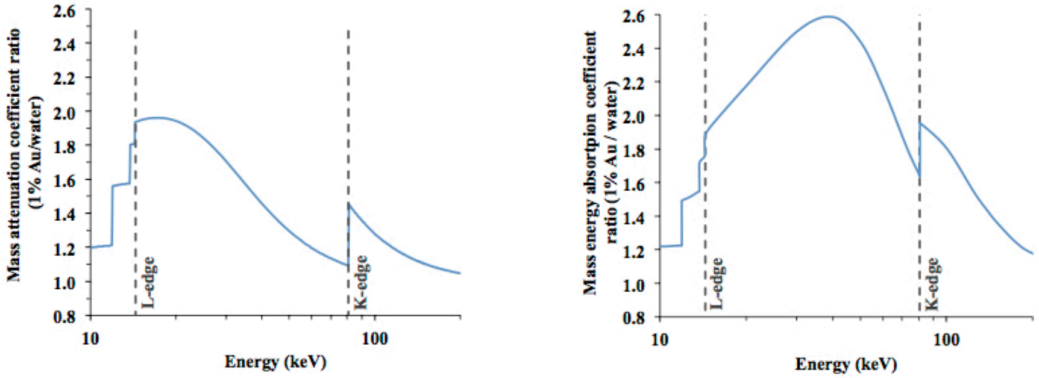

FIGURE 3.2: Left side: Ratio of Mass Attenuation Coefficients (Material with 1% Gold *vs.* Water); Right side: Ratio of Mass Energy Absorption Coefficients (Material with 1% Gold *vs.* Water) [5].

The emission of multiple Auger electrons results in the accumulation of positive charge on the nanoparticle, making it highly reactive with the surrounding medium. Consequently, electrons from water molecules and other biomolecules in the vicinity are drawn towards the nanoparticle. These phenomena involve exchanges of energy and charge, leading to ultra-fast atomic relaxation processes, which, in turn, give rise to the production of additional electrons and an increase in damage around the nanoparticle [19].

Given that the radiosensitizing effect of gold nanoparticles primarily arises from low-energy emitted electrons, it's valuable to understand how the range of these electrons varies with their energy. Figure 3.3 illustrates this relationship for energies spanning from 10 to 10000 eV.

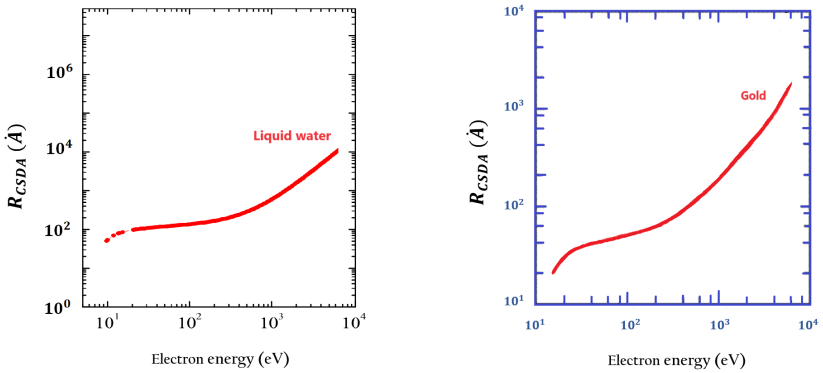

FIGURE 3.3: Range of low-energy electrons in liquid water [22] and in a gold material [23].

The plot was generated using Equation 2.7 and relies on stopping power data for both water and gold materials. Within the energy range of 10 to 100 eV, the electron

range remains relatively constant, at approximately 100 Å* for water and above 50 Å for gold. However, as the energy approaches 500 eV, the range shows an increase, and within the range of 1000 to 10000 eV, it appears to vary nearly linearly with energy. A significant observation is that, for electrons with the same energy, their range in water is approximately twice as extensive as in gold.

3.2 Radiobiology

The interaction between photons or electrons with matter can lead to various mechanisms that involve energy deposition. Understanding the effects of ionizing radiation on biological systems is a crucial aspect of radiobiology. The first documented physiological consequence of radiation was observed by Becquerel when he accidentally carried a radium vial in his jacket pocket. This exposure resulted in cutaneous erythema and ulceration, capturing the scientist's attention [10]. The study of radiobiology had its origins in these early observations at the end of the 19th century.

The presence of a sensitive target inside the cell, DNA, must be considered when evaluating the consequences on tissues. In eukaryotic cells, the nucleus includes the majority of the genes, formed by chromosomes, each one containing a lengthy DNA molecule linked to proteins. The nucleus is involved in regulating cell division and longevity, controlling protein synthesis, producing messenger RNA (mRNA) and delivering it to the cytoplasm, where ribosomes transcribe genetic information into polypeptides [24]. Therefore, maintaining the structural integrity of each DNA molecule is necessary for the correct function of a cell and the faithful transmission of its genetic information. The DNA molecule is composed of two complementary strands, each one formed by a series of nucleotides containing a base (purine or pyrimidine), a molecule of sugar and a molecule of phosphoric acid. The strands are linked by hydrogen bonds between the bases and are twisted together to form a double helix. During the process of replication, each strand serves as a model of the new genetic material [25].

The kind of interaction between the particles and the cells determines how the biological effects of ionizing radiation are studied. Radiation can directly interact with DNA molecules in a cell when it is absorbed by a tissue. In this situation, the atoms in the target can be ionized or excited, resulting in a series of events that might trigger biological changes. These direct action pathways are most common with high LET radiation.

*One Angstrom (Å) corresponds to 10^{-10} m.

Nevertheless, radiation can also have an indirect effect, interacting with other atoms or molecules within the cell instead of the sensitive target. Free radicals, which are molecules or atoms with an unpaired orbital electron in the outer shell, are created in these circumstances. This means that there is one electron in the outer orbit for which no other electron with an opposite spin exists, and hence there is a high level of chemical reactivity [10].

If radiation does not directly interact with the DNA molecule, it is plausible to suppose that the action occurs on water molecules, which make up the majority of the cell's composition. Ionization can occur when a water molecule reacts with radiation, resulting in the formation of an ion radical, which is a molecule with a positive electrical charge. The ion radical reacts with another water molecule to form the highly reactive hydroxyl radical (OH·), which possesses one electron unpaired and can diffuse a short distance to reach a critical target in a cell. This molecule has a lifetime of about 10^{-9} seconds in cells and is thought to cause almost two-thirds of the X-ray damage to DNA in human cells [10].

Damage to DNA caused by ionizing radiation can result in alterations to the genetic material. However, the time gap between the breakdown of chemical bonds and the emergence of biological effects varies depending on the subsequent consequences. Irradiation can lead to a range of lesions in DNA molecules, including strand breaks (both single and double), base modifications, sugar damage, cross-links, and more [25]. In fact, there have been identified 100 different types of lesions but strand breaks are the most common, both in frequency and significance. A significant chromosomal aberration may be caused by just one double strand break in a crucial section of DNA, destroying the cell [26].

A single strand break (SSB) of DNA may occur when cells are exposed to X-rays. If the DNA is denatured and the supporting structure is removed, these breaks may be measured based on the dose. On the other hand, if SSBs occur in intact DNA, they can be quickly repaired through the copy of the complementary strand, being harmless for the cell. Otherwise, a mutation might happen as a result of faulty repair. When the DNA is fragmented into two well-separated strands, repair can still proceed effectively since the two breaks are handled separately. Alternatively, if the breaks in the two DNA strands are near together or directly across from one another, it may result in a double-strand break (DSB). These are considered the most significant DNA damage induced by radiation in chromosomes and are formed in a dose-dependent manner, proving that they are caused by the passage of single ionizing radiation tracks [10]. Two lethal chromosome aberrations

that can occur are the dicentric and the ring. The first results from the interruption of two chromosomes, which causes an exchange between them and the development of a highly malformed chromosome with two centromeres. The second aberration is caused by radiation in each arm of a single chromatid, which results in the sticky ends reconnecting to create a ring and a fragment [10].

The correlation between radiation exposure and the percentage of surviving cells is shown by a cell survival curve. A cell may appear to be physically intact and be capable of producing proteins or DNA, but if it is no longer able to divide indefinitely it has not survived. In order to completely remove a tumor, cells simply need to be "killed" in the sense that they are made unable to proliferate and promote the malignancy's development and spread. It is feasible to create a single-cell solution from a tumor specimen in which the cell membrane has been dissolved. In order to attach these cells to the surface and allow them to develop, they are planted onto a culture plate and maintained there under precise conditions. Trypsin is used to remove the cells off the surface and the majority of them are discarded. The culture flask is then reseeded with a modest number of cells, which swiftly repopulate it. These are called established cell lines. Each cell divides several times, forming a colony that can be seen with the naked eye. The number of colonies counted should equal the number of cells implanted, although ambiguities in counting the cell suspension and poor growing circumstances might arise [10]. These aspects are taken into consideration by using a control dish, allowing the plating efficiency parameter (PE) to be calculated, which measures the percentage of cells implanted that grow into colonies. Thus, the survival fraction (SF) is defined by the equation below:

$$\mathrm{SF} = \frac{\text{Colonies counted}}{\text{Cells seeded}} \frac{1}{PE} \times 100$$

For viruses, bacteria, and haploid yeasts, the surviving fractions are shown to be exponentially dependent on dose, whereas survival curves for mammalian cells are more complexly shaped, also approaching exponential curves [25].

These curves are typically plotted on a logarithmic scale for two main reasons: if the surviving fraction is an exponential function of the dose, it results in a straight line on a semi-log plot, clearer to analyze; a logarithmic scale makes it easier to compare the

extremely low cell survival rates required to achieve a meaningful reduction in tumor size [26].

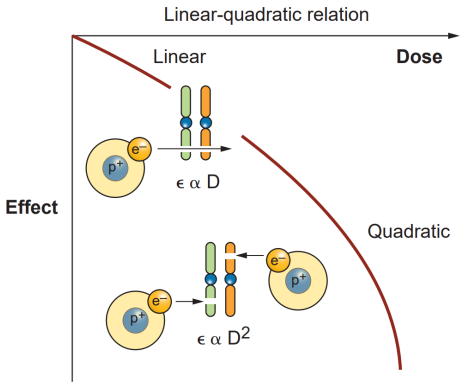

FIGURE 3.4: Two possible lethal chromosome aberrations, depending on the dose [26].

For comparing survival curves it is convenient to represent them by mathematical functions, based on hypothetical mechanisms of cell lethality. It is essential to remember that no single model can describe response across the entire dose range from very low to very high, unless that model is so complex that it is no longer therapeutically helpful [26].

In order to generate a curve that bends continually downward, as observed experimentally, a model is applied that simply fits the cell survival by a second-order polynomial, with a zero constant term to ensure that S = 1 at zero dose. This is known as the linear-quadratic (LQ) model, which is expressed by equation 3.1.

$$S_{LQ} = e^{-(\alpha D + \beta D^2)} \tag{3.1}$$

Biologically, this model proposes two mechanisms for cell death: accumulation of sublethal events or a single lethal event [25]. Assuming that these two mechanisms are independent, the probability of survival is the product of the probabilities of each one. In fact, the exponential term depending on α relates to the lethal events, while the term depending on β refers to sublethal events. Furthermore, the two processes of cell death are associated with the lethal chromosome aberrations, as illustrated in Figure 3.4. The linear component, $e^{-\alpha D}$, refers to dicentric or ring chromosomes formed from a single electron track intersecting both of two adjacent chromosomes. On the other hand, the quadratic component, $e^{-\beta D^2}$, arises from two independent electron pathways, each intersecting one of two connected chromosomes.

The linear component of cell killing replaces the quadratic component of cell killing as the dose rate is decreased. Cell survival curves become straight as the dose rate is

decreased and tend to extend the initial slope of the high dose-rate curve. This is due to the fact that at low dose rates, single-track events will happen further apart in time and there will be little chance that they will interact with each other in two neighboring chromosomes.

Moreover, LET affects the survival curve [10]. For low LET radiation doses, the survival fraction increases in direct proportion to dose, plotting a straight line with a small starting slope. The curving zone extends over a few grayscale dose levels as the curve bends. As dose rises, the curve straightens out once more so the survival fraction changes again exponentially with dose. In contrast, for high LET radiations, the cell survival fraction closely resembles an exponential function of dose over the whole region.

3.3 State-of-the-art

Numerous studies carried out in the latter part of the 20th century illustrated an increase in radiation dose at the boundaries between materials with low and high atomic numbers, especially when exposed to low energy photons. For instance, within the oral cavity, tissue layers adjacent to metallic dental replacement received doses that were as much as 2.6 times greater than that in tissues located further away when irradiated with a Co-60 beam [27].

In 1998, one of the earliest studies was conducted to assess interface effects involving a tissue-equivalent material in proximity to the surface of a metallic gold foil. The study suggested that when cell monolayers are irradiated along single-plane metal scattering surfaces with high atomic numbers (Z), cell death is optimized due to the presence of low-energy backscattered electrons from photon beams. However, this geometric setup is not applicable to the irradiation of solid animal tumors, and therefore, it cannot be employed in medical applications.

With the advancement of technology, gold microspheres with diameters ranging from 1.5 to 3.0 µm began to be commercially available and utilized for dose enhancement. This choice was motivated not only by the fact that particles of this size possess scattering surfaces smaller than the size of human tumor cells but also due to gold's biologically inert properties [28].

In the year 2000, it was observed that suspensions containing up to 3% gold microspheres yielded highly favorable outcomes. However, concentrations exceeding 1% raised specific concerns. Consequently, investigations into interface dose enhancement

were limited to gold particle concentrations up to that threshold. The average dose increase in solutions was approximately 42% for tumor treatments employing 200 kVp X-rays.

Based on these findings, gold has emerged as a highly investigated substance in the realm of cell sensitization for radiotherapy treatments. Nevertheless, a histological examination following a direct intratumoral injection of microspheres yielded no evidence of gold particles in regions densely populated by tumor cells, implying that achieving a uniform distribution with particles of this size would be challenging [29]. In contrast, nanoscale spheres have demonstrated the capability to accumulate a vast number of high-Z atoms within a single cell, along with the potential for tumor molecular conjugation. In practice, a 2 nm-diameter gold sphere is estimated to encompass around 250 atoms, while a 30 nm radiosensitization particle could contain a total of 835000 atoms [30]. Consequently, research into the dosimetric implications of gold has extended to encompass nanoscale geometries.

The initial demonstration of tumor control in vivo by absorbing X-rays using high-Z nanoparticles was documented in 2004 [29]. This experiment involved the intravenous administration of 1.9 nm gold nanoparticles to rats with subcutaneous mammary carcinomas, followed by X-ray irradiation (250KVp), considering a maximum density of 2.7 grams of gold per kilogram of tissue. The study revealed that the small size of the nanoparticles promoted enhanced permeability and energy retention in tumor-related areas. The quantity of gold administered directly correlated with the safe and effective ablation of tumors. Additionally, it was observed that the gold nanoparticles exhibited low toxicity to mice and were predominantly eliminated from the body through the kidneys.

It was crucial to have a comprehensive understanding of the individual physical processes involved in cell radiosensitization by AuNPs, based on experimental findings. With the advancement of computational capabilities, the Monte Carlo method emerged as the predominant technique for dosimetric calculations. The employed models provide valuable insights into the behavior of secondary electronic processes, enabling the computation of the dose enhancement attributed to the presence of AuNPs. This approach allows for the investigation of various scenarios by manipulating factors such as target shape, nanoparticle size and distribution, radiation source energy, and more, generating results that are often unattainable through empirical means.

In 2007, a significant study [31] employed Monte Carlo simulations to offer the initial evidence of how gold nanoparticles influence dose deposition at the molecular level. Although nanoparticles locally absorb X-rays, there was limited information available regarding the deposition of energy by low-energy electrons. The study employed a 100 kVp X-ray tungsten source, 3 nm-diameter gold nanoparticles, and a biological target consisting of super-coiled DNA (scDNA). The results indicated that a substantial portion of emitted electrons could traverse distances beyond the nanoparticle, with many electrons possessing energies below 100 eV being generated during this process. The localized distribution of energy deposition was confirmed through the observation of DNA chain breaks caused by hydroxyl radicals. Additionally, the presence of ten gold nanoparticles resulted in enhanced damage to a 5600 bp (base pair) DNA strand induced by X-rays.

Despite the demonstrated radiosensitization effect, previous estimations of the deposited dose resulting from nanoparticle activity tended to underestimate the actual effects due to the oversight of nanoscale non-homogeneities caused by gold. The initial outcomes, which assessed X-ray-induced cell death and were consistent with experimental observations, emerged in the early 2010s. One such study [32] conducted irradiation of a 20 nm-diameter nanoparticle with 100 KeV X-rays, detecting approximately 0.001 ionizations per Gy deposited in the vicinity. This finding highlights that the dose enhancement is not evenly distributed but rather exhibits peaks located a few nanometers from the nanoparticles. Notably, the dose deposited within a 1 nm-thick shell surrounding the nanoparticle is primarily attributed to Auger electrons, as illustrated in Figure 3.5.

Furthermore, numerous studies have indicated that the proximity of Auger electron generation to the gold surface results in a more substantial dose contribution to that region. Only high-energy electrons possess the necessary range to exit the gold surface and deposit their energy at a greater distance, when ionization events take place within the nanoparticle's bulk. In contrast, at significant distances from the AuNP, the majority of ionization events yield only one or two electrons. In close proximity, there is a more pronounced electron dispersion, with approximately 5% of ionization events producing 10 or more electrons.

The size of nanoparticles is another critical factor determining energy deposition. Research has revealed that when the smaller particles become ionized, they deposit larger doses in their vicinity due to their higher surface-to-volume ratio [32]. For instance, nanoparticles with a 2 nm diameter deposit approximately three times more energy within

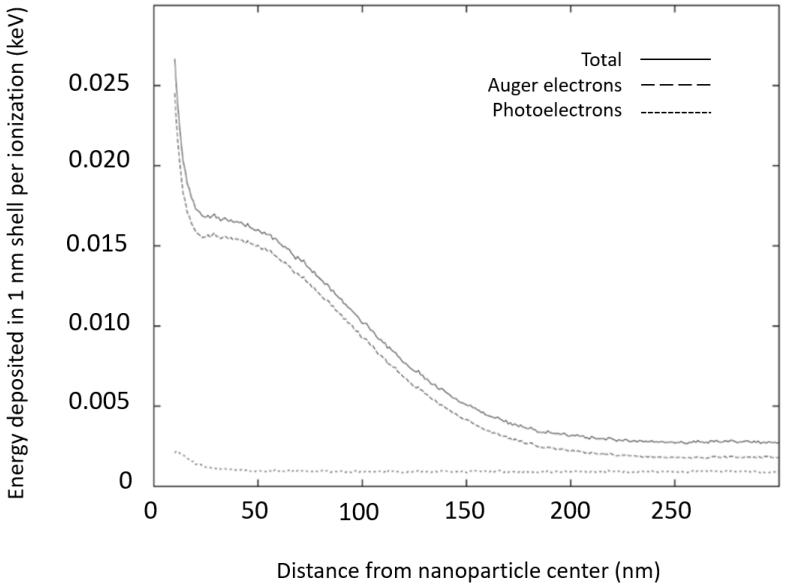

FIGURE 3.5: Contribution of Auger electrons and photoelectrons to dose deposition as a function of distance from the center of the nanoparticle [32].

distances less than 200 micrometers compared to nanoparticles with a 50 nm diameter after a single ionization event. However, larger nanospheres, containing more gold atoms, maximize the photoelectric absorption effect. When considering equivalent incident energy, experimental results showed that the photoelectric absorption rate as a function of nanoparticle size follows a cubic relationship. An increase in size from 5 nm to 100 nm results in a four-order magnitude increase in the photoelectric absorption effect [30]. Therefore, after comparing treatments using nanoparticles of different diameters but the same amount of AuNPs per cell, it was found that energy deposition is more efficient when employing larger diameter particles.

As nanoparticle diameter increases, a significant portion of the energy from Auger and delta electrons is absorbed internally by the nanosphere. Consequently, the dose enhancement ratio (DER) as a function of AuNP size is not precisely proportional to the AuNP radius cubed. Thus, in terms of milligrams of AuNPs per gram of tumor, smaller particles provide a greater dose enhancement per ionization event, allowing more low-energy electrons to escape into the surrounding tissue [30]. Furthermore, there are no significant variations in radiosensitivity at considerable distances from gold because the highest dose contribution consists of the more energetic electrons escaping from the spherical volume, irrespective of its diameter. These findings are corroborated by a 2017 study [33], which presents the dose per ionization event as a function of radial distance and demonstrates

distinct "step-like" patterns due to the substantial number of low-energy Auger electrons emitted from the AuNP.

In addition to ionization event location and cell diameter, the effect of incident energy on radiosensitization by AuNPs has been thoroughly investigated. X-ray irradiations at different kilovoltages have resulted in slightly varied dose enhancements. Generally, it has been observed that a 50 kVp source provides highly effective treatment [34]. However, a 51 KeV monoenergetic beam has a 20% lower likelihood of interacting with gold compared to a 250 kVp beam. A study conducted in 2020 [19] produced similar results regarding the impact of energy and size variations on energy deposition around AuNPs. This study utilized nanoparticles with diameters of 50 and 100 nm and subjected them to irradiation at 50 and 100 kVp. The findings revealed that the enhancement in dose deposition within the first 10 nanometers was greater for the larger AuNPs irradiated with the lower energy source.

While kilovoltage X-rays have demonstrated effectiveness in dose enhancement, investigations into the effects of external sources such as megavoltage and brachytherapy seeds have also been conducted. It has been determined that the number of 30 nm-diameter nanospheres required to induce a single photoelectric event in a cell using a 6 MV source is approximately a thousand times greater than when utilizing an I-125 source. Furthermore, with a 6 MV source, doubling the prescribed dose would necessitate around 1000 mg of gold per milligram of tumor, which is a concentration that is not clinically feasible [30].

Nevertheless, secondary electrons play a significant role in the dose distribution for this type of therapy. When the dose is localized around a 50 nm-diameter nanoparticle, photons account for only 42% of the total dose near the nanoparticle's surface, increasing to 97% at a distance of 10 µm [35]. It has also been demonstrated that for irradiation with a 6 MV photon source, no radiosensitization effects were observed for an extracellular distribution (2% mass weight) of 15 nm-diameter gold nanoparticles. In contrast, with an I-125 source, the nanoparticle diameter affects energy deposition, with the greatest dose enhancement occurring for smaller nanoparticles, unlike the situation with kilovoltage X-ray sources [36].

It has also been demonstrated that when using a radiation source with energy below the K-edge of the gold atom (80.7 keV), photoelectric absorption occurs predominantly

in the external atomic shells. In this energy range, the localization of nanoparticles becomes a crucial factor in cell radiosensitivity because the photoelectrons generated have limited ranges, and Auger electrons contribute significantly to the total escaping energy [37]. Conversely, with a more energetic source like 300 kVp, photoelectric absorption primarily occurs in the K-shell, indicating that the most significant contribution to dose enhancement comes from high-range photoelectrons.

Figure 3.6 illustrates how various sources influence the energy spectrum emitted by a 30 nm AuNP. For lower energy sources, such as Pd-103 and I-125, electron ranges are confined within a single cell, assuming a hypothetical cell radius of 10 µm. In contrast, higher energy sources cause photoelectrons to traverse multiple cells [30].

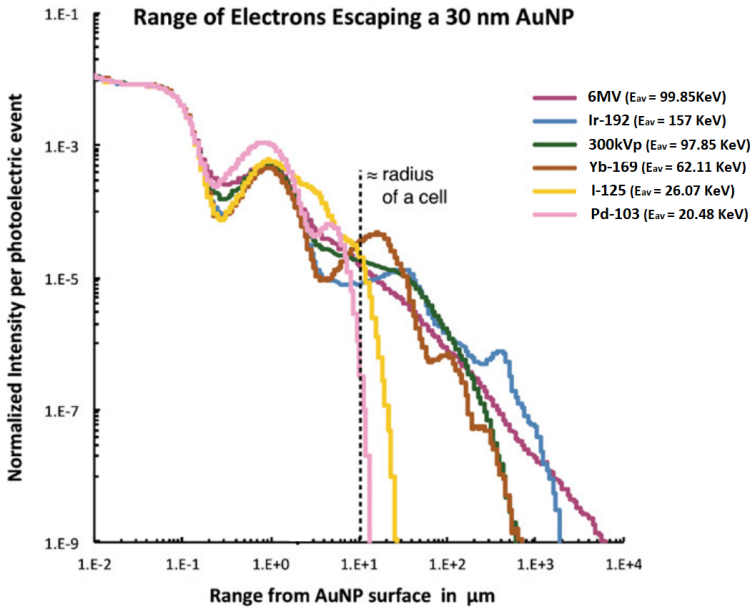

FIGURE 3.6: Range of electrons escaping a gold nanoparticle for different radiation sources [30].

In general, studies have indicated a higher treatment efficacy when using external radiation sources in kilovoltage X-rays. However, there have been limited investigations into the radiosensitization induced by irradiating gold nanoparticles (AuNPs) with protons. In a 2014 study [35], it was reported that, for distances ranging from 1 to 10 µm from the surface of a 50 nm AuNP, monoenergetic proton beams produced a dose enhancement of 14 for all energies studied. Unlike photon irradiation, the dose enhancement was found to be nearly independent of the proton's incident energy. Furthermore, the number of electrons generated per particle fluence was considerably higher compared to a 6 MV

photon source. At a distance of 10 µm, the dose enhancement produced by 250 kVp photon irradiation was approximately 20 times greater than that of a proton source. These results were confirmed by a study published a year later, which showed that although proton irradiation exhibited an increase in energy deposition, it resulted in a substantial reduction in dose and a very low likelihood of interaction with the AuNP compared to a kilovoltage beam [38].

Many studies have traditionally focused on spherical geometry when considering nanoparticles and cells, simplifying the complexities of real-world scenarios. However, this approach may not fully capture the diverse geometries and arrangements of gold nanoparticles and cells in actual biological systems. In a study published in 2016 [36], researchers explored the impact of using an I-125 source enclosed by a gold nanoshell with varying internal and external diameters. The findings indicated that, generally, the dose enhancement was less than 1 for small distances, but it reached higher values when the distance from the nanoshell ranged from 10 nm to 200 nm. This study highlighted that the size of both the internal and external diameters of the nanoshell played a significant role in maximizing dose enhancement.

In terms of cell geometry, a 2017 study [33] assumed the presence of nanoparticles (15 nm) distributed in the extracellular medium. The study concluded that radiosensitization was slightly greater in the case of an elliptical cell with a high eccentricity. Additionally, variations in the distance between the cell's core and membrane were found to influence the radiosensitization effect. Consequently, the distribution of lethal damage within the cell nucleus exhibited heterogeneity, strongly correlating with the distance to the extracellular medium containing nanoparticles. These findings underscore the importance of considering realistic cell geometries and nanoparticle distributions in studying radiosensitization effects.

Another crucial factor in the context of cell radiosensitivity is the localization and concentration of nanoparticles within the cell. Many studies have consistently shown increased radiosensitivity when nanoparticles are in direct contact with the cell nucleus ([34], [37], [38]), emphasizing the significance of localized dose deposition. In cases where nanoparticles are distributed throughout the entire cell, including the nucleus that contains DNA, the vulnerability of the nucleus to the effects of gold is heightened, reducing the relative importance of cell geometry in dose deposition [33].

When cells take up AuNPs, a significant portion of them are internalized through

endocytosis and subsequently reside in the lysosomes, with limited access to the nucleus [35]. For instance, a study conducted in vivo [37] revealed that AuNPs are distributed randomly in the cytoplasm but do not penetrate the nucleus of PC-3 prostate cancer cells. Moreover, a nanoparticle concentration of 2 mg/mL in the cell culture media corresponded to a gold accumulation in the cytoplasm of 0.84 mg/mL, resulting in a concentration uptake ratio of 0.42. In such cases, if a kilovoltage photon source is employed, the irradiated AuNPs can generate electrons with sufficiently long ranges to reach the nucleus.

Figure 3.7 illustrates survival curves for a spherical cell with a spherical nucleus when exposed to a 250 kVp photon beam, a proton beam, and a 6 MV photon beam. All scenarios involve gold nanoparticles with a 50 nm diameter, but the concentration is ten times lower for the kilovoltage source. Interestingly, irradiation with protons and megavoltage photons results in significantly lower cell death [38]. Furthermore, for photon irradiation, the nanoparticle's location within the cell has a prominent impact on dose enhancement. In proton irradiation, concentration becomes a critical factor only when nanoparticles are distributed within the cell nucleus. When nanoparticles are internalized within the nucleus, proton irradiation generates a sufficient number of secondary electrons to induce DNA damage, underscoring the importance of cell uptake in this type of therapy [35].

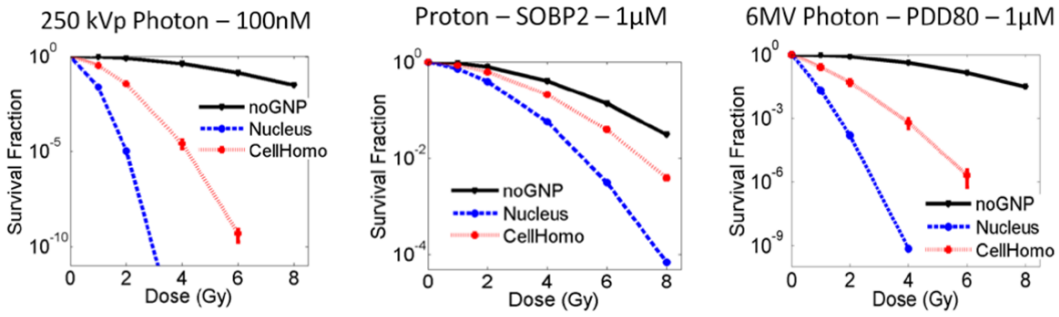

FIGURE 3.7: Survival curves for different distributions of AuNPs (=GNPs) within a cell, considering various radiation sources: kilovoltage photons on the left, protons in the middle, and megavoltage photons on the right [38].

Besides the nucleus, a study conducted in 2006 explored the physical effects induced by ionizing radiation in various cellular compartments, encompassing the cytosol and mitochondria [39]. Cell death from ionizing radiation is traditionally linked to DNA damage, implying that nanoparticles should be placed into the cell nucleus for efficient tumor

tissue destruction. The researchers investigated how gold nanoparticles, which tend to accumulate in the cytoplasm, affect radiation therapy in homogeneous and heterogeneous cellular configurations. For homogeneous cells, the addition of 1% gold was found to increase both energy transfer and the total number of ionizations for all materials studied. In the more realistic heterogeneous cell model, introducing 1% gold into the cytosol significantly enhanced energy deposition by 32% in the mitochondria and 13% in the nucleus. This was due to photoelectrons transferred energy within the cytosol on a submicrometer scale, with a greater impact on mitochondria due to its larger surface area in contact with the cytosol compared to the nucleus. Although gold nanoparticles are mainly found in the cytosol, they could still enhance dose effects in the nucleus and mitochondria, especially in the latter organelle.

3.3.1 Local Effect Model

In recent years, some studies have explored how various factors, including the size of AuNPs, the type of radiation source, cell geometry, and nanoparticle distribution, affect cell radiosensitization. The non-uniform dose distribution induced by gold nanoparticles was a crucial factor in these studies, motivating the implementation of the **Local Effect Model** (LEM).

This model was originally developed for tumor treatment using heavy ions, which have a high relative biological effectiveness (RBE) because of the unique dose distribution within each particle track [40]. Since high local doses create lesions with a reduced likelihood of repair, cell killing is optimized. This principle is also applicable in systems using AuNPs as radiosensitizers because of their unique dose distribution patterns. Therefore, LEM has been tested in this context as well.

As previously stated, gold nanoparticles generate an extremely high dose in their immediate surroundings due to the emission of many secondary electrons. The Local Effect Model takes into account the radial dose distribution formed by the secondary electrons around the primary particle track, which enables accurate estimations of the deposited energy.

In practical applications of the Local Effect Model (LEM), the required input parameters encompass local doses, the cell's geometric model (which includes the volume of the nucleus and the distribution of gold nanoparticles) and the dose-response curve specific to sparsely ionizing radiation [40]. Furthermore, the survival cell curve predicted by

this model contains the radial dose distribution attributed only to the gold nanoparticles added to the uniform dose provided by X-rays that do not interact with the nanoparticles [32].

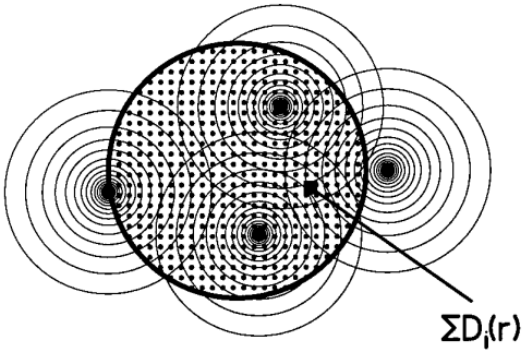

FIGURE 3.8: Exemplification of the LEM principle, where the nucleus is divided into small compartments [41].

After acquiring the aforementioned input parameters, the radial dose distribution generated by the gold nanoparticles is applied to the cell nucleus. The nucleus is subsequently subdivided into compartments with uniform doses, as depicted in Figure 3.8, and the number of lethal lesions is determined using the X-ray dose-effect curves, as follows.

For irradiation without gold nanoparticles, cell killing is induced by a homogeneous dose, and the mean number of lethal events is determined by Equation 3.2, which takes into consideration the survival fraction (S). As mentioned in Section 3.2, when a tissue is exposed to ionizing radiation, the fraction of surviving cells is described by the linear-quadratic model (Equation 3.1). The LQ model depends on parameters such as α and β along with the mean dose computed on a macroscopic scale, averaged across a volume of cells.

$$\bar{N}_X(D) = -\log(S[D]) = \alpha D + \beta D^2 \tag{3.2}$$

In the case of using AuNPs as radiosensitizers, a similar dose leads to a higher number of cells killed, hence the need to consider inhomogeneous radiation for lethal events. In the Local Effect Model (LEM), it is assumed that lethal events can occur independently of interactions between sublethal damages over relatively large distances on the order of micrometers [41]. Another fundamental assumption in LEM is that the event densities*

*The lethal event density corresponds to the fraction between the number of lethal lesions and the target volume.

resulting from photon irradiation, with or without the presence of gold nanoparticles, are equivalent for the same local dose. This implies that the local biological effect remains consistent regardless of the specific type of radiation responsible for the local dose. Therefore, when considering $\nu_g(\vec{r})$ and $\nu_x(\vec{r})$ as the lethal event densities at a specific point ($\vec{r}$) for irradiation in the presence and absence of gold nanoparticles, respectively, the equation $\nu_g(\vec{r}) = \nu_x(\vec{r})$ holds true [41]. Consequently, for a subvolume ΔV, the average number of lethal lesions can be expressed as:

$$\bar{N}_{\text{AuNP}} = \nu_g(\vec{r})\,\Delta V = \nu_x(\vec{r})\,\Delta V = \frac{\bar{N}_{\text{X}}(D[\vec{r}])}{V}\,\Delta V \tag{3.3}$$

Thus, for an inhomogeneous radiation field, the total number of lethal events N_{tot} can be calculated by the lethal events produced by an homogeneous dose at each point $\vec{r}$ integrated over the whole target volume [40]. By combining this consideration with expressions 3.2 and 3.3, it follows:

$$N_{tot} = \int_V -\frac{\log(S[D])}{V}\,dV \tag{3.4}$$

Finally, with the lethal events induced by the dose distribution caused by the gold nanoparticles, the survival fraction (S_g) resulting from its inhomogeneous field is determined by Equation 3.5.

$$S_g = e^{-N_{tot}} \tag{3.5}$$

It should be noted that the linear-quadratic (LQ) model tends to overestimate the response at high doses above a threshold dose, and sometimes the linear-quadratic-linear (LQL) model is employed as an alternative [38], but in this work, only the LQ model will be used.

Additionally, this method relies on the dose distribution induced solely by the gold nanoparticles, which is not directly obtained from Monte Carlo simulations. Typically, the data are expressed in terms of Gy/history, neglecting the probability of interaction between the particles emitted by the source and the gold nanosphere. For example, Figure 3.7 depicts survival curves using LEM, where the dose was calculated by multiplying the dose from a single ionizing event by the number of AuNPs, the interaction probability per Gray, and the prescribed dose.

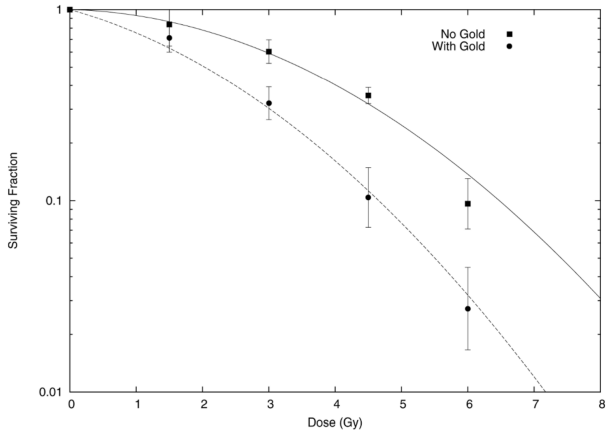

FIGURE 3.9: Comparison of the survival curves derived from experimental data with the predictions made by the LEM model, revealing a high degree of concordance [32].

Despite the additional assumptions and uncertainties introduced by LEM, they are preferred because standalone Monte Carlo simulations often underestimate radiation effects when compared to experimental results, possibly due to a lack of consideration for chemical interactions [6]. The Local Effect Model has displayed promising results, showcasing a strong agreement between its predicted curves and those derived from experimental irradiations, as depicted in Figure 3.9. Nevertheless, it's imperative to highlight that for an emerging theoretical approach like LEM, thorough validation is essential before its application in medical therapy. Additionally, it's important to acknowledge that the results obtained carry a degree of uncertainty, emphasizing the need for cross-validation using various simulation codes to ensure the robustness and reliability of the outcomes.

Chapter 4

Computational Techniques

4.1 Monte Carlo

The scientific approach to understanding nature involves two fundamental components: conducting observational experiments and creating theoretical hypothesis. Various mathematical, computational, and simulation techniques aid in the collaboration between these components. The Monte Carlo method effectively encompasses and utilizes these diverse approaches.

Stochastic sampling methods were known long before the computer era. In 1777, Comte de Buffon proposed a method resembling Monte Carlo to determine the outcome of an "experiment". This involved repeatedly tossing a needle onto a sheet of paper filled with lines and calculating the probability of the needle crossing one of the lines [42]. In 1947, the first suggestion to use stochastic sampling methods for radiation transport calculations was documented. Two years later, Metropolis and Ulam, who were engaged in nuclear weapons projects at Los Alamos, coined the term "Monte Carlo" to define a class of numerical methods relying on random number usage [8]. Today, the Monte Carlo method is a numerical technique employing repetitive random sampling to simulate the behavior of intricate systems.

In practice, pseudo-random number generators are used. Unlike rolling dice or spinning a roulette wheel, pseudo-random algorithms generate deterministic sequences that depend on initial values, known as seeds. Simulations with different random seeds ensure simulations with independent statistics, while identical seeds produce identical simulations. Thus, pseudo-random number generators allow the creation of sequences with

arbitrary behavior, and using the same seed becomes a valuable tool for code validation, program installation verification, and error correction.

The main drawback of the Monte Carlo method lies in the statistical uncertainties associated with the random nature of the generated sequences. Reducing these uncertainties involves increasing the sampled population and, consequently, the computational calculation time. Nevertheless, Monte Carlo simulation has evolved into a widely used tool in radiation physics research due to its capability to estimate parameters related to particle transport within specific mediums. In medical physics, this approach proves exceptionally valuable across diverse applications, including predicting patient dose deposition, enhancing X-ray image reconstruction, optimizing radiotherapy procedures, and calculating radiological protection metrics [16].

The fundamental concept that defines radiation transport simulation is the trajectory of a particle. As radiation passes through the medium, it interacts with its constituents, causing the initial particles to change their direction, lose energy, and occasionally generate secondary particles. A particle's history encompasses its entire path, consisting of a sequence of successive random flights resulting from the interaction events it experiences.

For a photon, its history is defined by a low average number of interaction events. As previously mentioned, a single photoelectric event, pair production event, or a few Compton interactions are adequate for a photon to completely lose its energy. Consequently, simulating photon transport using the Monte Carlo method is relatively straightforward.

On the contrary, a high-energy electron can undergo millions of elastic scattering events before it stops. This meticulous analysis, which involves tracking every interaction in the trajectory of such particles, is referred to as *analog* simulation and requires a considerable amount of computational time. To address this, techniques have been devised to simulate condensed histories, which optimise electron transport by encompassing the effects of multiple interactions within each step of the simulation [8].

4.1.1 Radiation Transport in Therapy

The trajectory of a specific particle is determined by its state immediately after an interaction, meaning it is defined by its position coordinates $\vec{r} = (x, y, z)$, energy E, and propagation direction $\hat{d} = (u, v, w)$. The mean free path $< s >$ between collisions, the interaction mechanism at play, angular deflection, and energy loss are all random variables

extracted from their respective probability distribution functions using various random sampling techniques [8].

In particular, the length s, which represents the distance covered between interactions, is computed using the inverse-transform method. This technique employs the inverse of the cumulative distribution function to sample a variable with a known probability distribution. It is established that s follows a continuous random distribution as described by Equation 2.3. The cumulative probability function corresponding to this distribution, denoted as $F(s)$, varies between 0 and 1 and is defined as:

$$F(s) = \int_0^s p(s)ds = \int_0^s \mu\, e^{(-s\mu)}ds = 1 - e^{(-\mu s)} \tag{4.1}$$

The cumulative distribution function is a function that increases monotonically with the variable s, and as a result, it possesses an inverse function denoted as $F^{-1}(\zeta)$ (as illustrated in Figure 4.1.a). If there exists a random variable ζ such that $\zeta = F(s)$, then its distribution follows a uniform pattern between 0 and 1. This principle also works in reverse: if ζ is a random variable that is uniformly distributed between 0 and 1, and s is another random variable linked by the relation $s = F^{-1}(\zeta)$, then the distribution of s corresponds to the function $p(s)$.

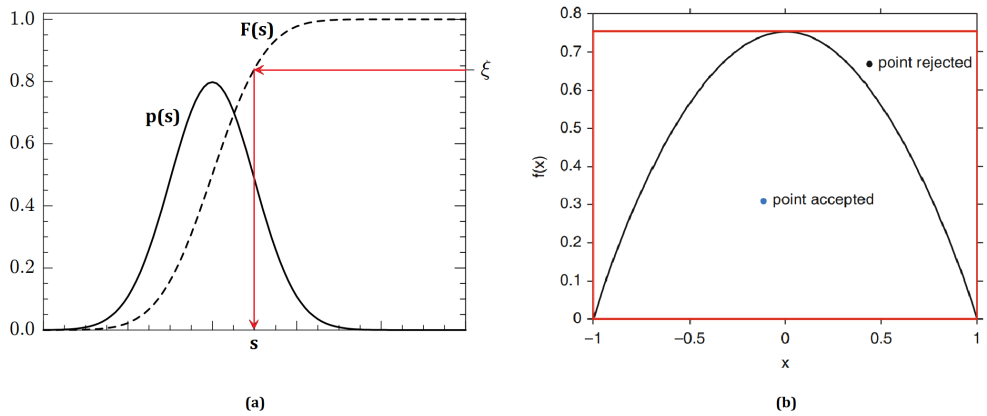

FIGURE 4.1: Representation of two different Monte Carlo sampling techniques. a) Random sampling from a distribution $p(s)$ using the inverse-transform method [8] b) Random sampling using a simple rejection method.

Equation 4.1 provides the means to sample the distance s between interactions. To maintain notation appropriate for varying geometries [42], the introduction of the variable λ is advantageous. This variable signifies the accumulation of the number of mean free paths (MFP) in each medium i, and it establishes a relationship with Equation 2.4 in the following manner:

$$\lambda = \sum_i \frac{s_i}{< s_i >} = \sum_i \mu_i s_i \tag{4.2}$$

Consequently, the distance traveled between interactions can be sampled using a uniformly distributed random variable ζ within the interval [0,1], as illustrated below*:

$$\zeta = 1 - e^{-\lambda} \Leftrightarrow \lambda = -ln(1-\zeta) \cong -ln(\zeta) \tag{4.3}$$

Apart from calculating the distance covered between collisions, it's equally crucial to identify the specific interaction to be simulated. As explained in Section 2.1, the most common interactions within the domain of radiation therapy's energy range include Photoelectric absorption (A), Rayleigh scattering (R), Compton scattering (C), and pair production (P). Hence, the linear attenuation coefficient encompasses the cumulative impact of all these effects.

$$\mu_{tot}(E) = \mu_A(E) + \mu_R(E) + \mu_C(E) + \mu_P(E) \tag{4.4}$$

It's worth noting that the probability of a specific event occurring is calculated by dividing the characteristic attenuation coefficient of that particular interaction by the total attenuation coefficient. By utilizing a randomly generated number ζ_2 uniformly distributed in the range [0, 1], the interaction type can be determined as follows [42]:

$$\zeta_2 \in \begin{cases} [0, \frac{\mu_A}{\mu_{tot}}] & \rightarrow \textit{Photoelectric absorption} \\ [\frac{\mu_A}{\mu_{tot}}, \frac{\mu_A+\mu_R}{\mu_{tot}}] & \rightarrow \textit{Rayleigh scatter} \\ [\frac{\mu_A+\mu_R}{\mu_{tot}}, \frac{\mu_A+\mu_R+\mu_C}{\mu_{tot}}] & \rightarrow \textit{Compton scatter} \\ [\frac{\mu_A+\mu_R+\mu_C}{\mu_{tot}}, 1] & \rightarrow \textit{Pair production} \end{cases}$$

Once the interaction type and the distance between collisions are determined, values for energy loss (denoted as W) and the characteristic deflection angles (θ and ϕ) need to be established.

*This equivalence arises from the fact that $1-\zeta$, akin to ζ, is a random number uniformly distributed between [0,1], thereby avoiding one subtraction and leading to slightly faster computation [8]

Because the molecules in the medium are randomly oriented, the differential cross-sections are unaffected by the azimuthal angle. This suggests that the azimuthal angle at each collision is uniformly distributed throughout the range $[0, 2\pi]$. Given that $d\Omega = \sin(\theta)d\theta d\phi$ and that σ is obtained by integrating the double differential cross-section, as described in Equation 2.2, the random variables θ and W have well-known probability distributions [8], which can be efficiently sampled using appropriate methods. It is important to emphasize that both probabilities and cross-sections are affected by the particles' starting energy.

$$p(\phi) = \frac{1}{2\pi}$$
$$p(\theta, W) = \frac{2\pi \sin(\theta)}{\sigma} \frac{d^2\sigma(\theta, W)}{d\Omega dW} \tag{4.5}$$

After sampling these variables, the particle's energy is reduced, and its movement direction is changed to $\hat{d}_n = (u', v', w')$ through rotations of the initial direction $\hat{d}_{n-1}$. As a result, the positions of a specific collision depend on the previously generated variables, namely $\vec{r}_{n+1} = \vec{r}_n + s\hat{d}_n$. This principle operates under the assumption that particle transport follows Markov processes, where 'future values of a random variable (interaction event) are statistically determined by present events and depend only on the event immediately preceding' [8].

The rejection method is a notable Monte Carlo technique for sampling variables with probability density functions (PDF) such as those presented in Equations 4.5. This algorithm can be comprehended through straightforward graphical explanations, exemplified in Figure 4.1.b.

The rejection method samples a random variable from a different distribution than $p(x)$ and then puts it into a random test to decide whether it should be accepted or rejected for future applications [8]. When a PDF $\Gamma(X)$ generates a random value x, a corresponding random value y is uniformly distributed in the interval $(0, c\Gamma(X))$, where c is a positive constant. The points (x, y) created in this manner are clearly evenly distributed in an area A below the curve $y = c\Gamma(X)$. If (x, y) are uniformly distributed in the area A and $c\Gamma(X) \geq p(x)$, then the locations where $y \leq p(x)$ have their x-coordinate scattered according to $p(x)$. This is equivalent to rejecting the point where $y \geq p(x)$; hence,

expressing $p(x) = c\Gamma(x)r(x)$, where $\Gamma(x)$ is a PDF that is simple to sample, $c > 0$, and $0 \leq r(x) \leq 1$, a rejection process is properly specified.

With this technique, it is possible to sample from any probability density function in a flexible way. However, it might not always be the simplest or most effective course of action. The simple rejection method offers a direct algorithm, but its efficiency compared to the inverse-transform method depends on the properties of the specific distribution [42].

4.1.2 Analog simulation *vs.* condensed history

The trajectory of a particle is determined by calculating specific parameters that are sufficient to generate the particle's path. With each collision, new variables are computed, and all steps are iterated, as depicted in Figure 4.2. The simulation ends when the particle exits the region of interest or when its energy falls bellow a certain value (E_{cut}), indicating absorption.

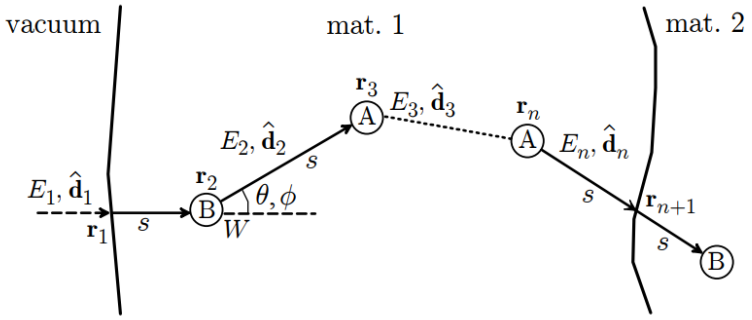

FIGURE 4.2: Illustration depicting the generation of random trajectories using a detailed simulation approach [8].

The outlined process takes into account all interactions taking place within the geometry of interest, along with all deviations experienced by the simulated particle. This approach is referred to as *analog* simulation. This method is applicable to photons due to the fact that the average distance between two interactions in the therapeutic energy range is comparable to the dimensions of the considered geometries [42].

However, the same principle doesn't apply as effectively to electrons. For radiotherapy energies, electrons follow intricate paths, undergoing numerous collisions within the medium. As a result, determining electron transport parameters using analog simulations is computationally time-intensive and unfeasible. Despite this, in the case of electrons,

nearly all collisions are either elastic or semi-elastic, involving small energy transfers to the surrounding medium and slight deviations in the initial direction at small angles.

To accelerate computational processes, a strategy known as the *condensed history* technique is employed. This approach, introduced in 1963, involves grouping multiple soft interactions into a single event, effectively replacing numerous small deflection angles with a single larger multiple scattering angle. As a result, the simulation implicitly considers soft collisions, where charged particles progressively transfer energy to the medium. On the other hand, hard collisions are explicitly simulated, following a methodology similar to that used for photons [42]. Distinguishing between these types of interaction is based on assigning arbitrary values, denoted as W_{CC} for collision mechanisms and W_{CR} for bremsstrahlung processes. In practical terms, "soft collisions" refer to events where collisional interactions transfer energy within the range $E \in]0, W_{CC}]$ to secondary particles. Consequently, the parameter W_{CC} sets a threshold for the maximum range of charged secondary particles within the medium under consideration. Ensuring the accuracy of simulation outcomes sometimes requires that the chosen value for W_{CC} is smaller than the spatial resolution of the geometry. However, extremely small values of W_{CC} result in longer computational times, so a careful balance must be taken into account. Similar considerations apply to the bremsstrahlung production threshold, W_{CR}.

In addition to the defined energy thresholds, another parameter called the "maximum step size" (DS_{max}) is introduced, which imposes a limit on the distance covered between consecutive condensed history steps. If the distance sampled exceeds this predefined maximum value, the particle's trajectory is adjusted to cover a distance of DS_{max}, deviating from the originally sampled value. Upon completing this adjusted distance, the particle's energy and direction remain unchanged, resulting in what is termed a "delta interaction" [8]. This maximum step size becomes particularly relevant when dealing with very thin volumes. In such cases, if a lengthy distance is randomly sampled, the particle might traverse a thin medium without undergoing significant interactions, ignoring the medium's influence. The introduction of DS_{max} ensures that the conclusion of a condensed history step is determined either by reaching the maximum step size or encountering the next hard interaction.

4.2 PENELOPE

The Monte Carlo algorithm and computer code used for simulating coupled electron–photon transport in this study is the 2018 version of PENELOPE. The name stands for "PENetration and Energy LOss of Positrons and Electrons", which was established in 1996. Subsequently, enhancements were made to include photon interactions, as well as improvements aimed at enhancing the code's reliability and flexibility [8]. The core of the system is based on a set of Fortran * subroutines designed to handle the complexities of the transport process. As a result, the programs should be compatible with any platform equipped with a Fortran 90 or later compiler. It's important to emphasize that measurements are presented in centimeters for lengths, degrees for angles, electronvolts (eV) for energies, and seconds for times.

The interaction models employed, along with their associated databases in PENELOPE (refer to Appendix C.1), facilitate the simulation of electron/positron and photon transport over a wide energy range spanning from 50 eV to 1 GeV [8]. Furthermore, PENELOPE provides users with the capability to develop their own simulation programs, incorporating custom geometries and scoring methodologies, all without necessitating a profound grasp of the theoretical intricacies of scattering and transport theories.

To better comprehend the importance and practical application of Monte Carlo techniques in radiation transport simulations, the following succinct explanation elaborates on how the PENELOPE system employs these methods to generate specific quantities during photon interactions. Equations 2.8, 2.9, 2.10, and 2.11 are employed to describe the differential cross sections of the photon processes.

The initial step involves using these equations to construct the probability density function of a variable X in the form: $p(X) = \Gamma_i(X)\, g_i(X)$, as illustrated in Table 4.1 for the case of the photoelectric effect. The functions for other interactions are presented in the Appendix C.1.

	$\boldsymbol{\Gamma(X)}$	$\mathbf{g(X)}$
Photoelectric (i = 1, X = ν)	$\Gamma(\nu) = \frac{A+(A+2)^2}{2}\frac{\nu}{(A+\nu)^3}$	$g(\nu) = (2-\nu)\left[\frac{1}{A+\nu} + \frac{\beta\gamma}{2} + (\gamma-1)(\gamma-2)\right]$

TABLE 4.1: An example of the PDFs employed for simulating Photoelectric absorption in PENELOPE.

*Fortran is a high-performance parallel programming language, representing an optimal tool to perform fast arithmetic computation over large numeric arrays [43].

Then, for each interaction, Monte Carlo techniques such as the inverse-transform method, rejection method, or RITA algorithm * are utilized to generate random values from the probability distribution $\Gamma(X)$. For instance, in the case of the photoelectric effect, the variable $\nu = 1 - \cos(\theta)$ ranges from 0 to 2. Here, the function $g(\nu)$ is always positive and reaches its peak at $\nu = 0$, while the function $\Gamma(\nu)$ is also positive and normalized to unity. A random variable ζ can be generated using the inverse-transform method as follows:

$$\zeta = \int_0^{\nu} \Gamma(\nu')d\nu$$

$$\Leftrightarrow \zeta = \int_0^{\nu} \frac{A(A+2)^2}{2} \frac{\nu'}{(A+\nu')^3} d\nu' \Leftrightarrow \zeta = \frac{(A+2)^2}{2} \frac{\nu^2}{2(A+\nu)^2}$$

$$\Leftrightarrow \left(\frac{4\zeta}{(A+2)^2} - 1 \right) \nu^2 + \left(\frac{4\zeta}{(A+2)^2} 2A \right) \nu + \frac{4\zeta A^2}{(A+2)^2} = 0$$

This approach allows for the generation of the variable X, in this case ν, using the distribution $\Gamma(\nu)$:

$$\nu = 2A \frac{2\zeta + (A+2)\zeta^{\frac{1}{2}}}{(A+2)^2 - 4\zeta} \tag{4.6}$$

Finally, random sampling can be performed using the rejection method, in which a random number U is generated and then compared to the function $g(\nu)$ to decide if it is accepted or rejected. This action eventually results in the angular deflection of the photoelectron. The process described is illustrated in Figure 4.3, which provides a schematic representation applicable to all photon interactions.

4.2.1 PenEasy

PENELOPE cannot operate independently; it functions as a subroutine package and therefore requires a steering main program to simulate specific problems. For this purpose, the main program utilized in this study is penEasy, responsible for defining the essential parameters required for the simulation. PenEasy employs an input file with the

*Rational Inverse Transform with Aliasing, developed by PENELOPE to simulate elastic collisions of electrons and positrons, and coherent (Rayleigh) scattering of photons

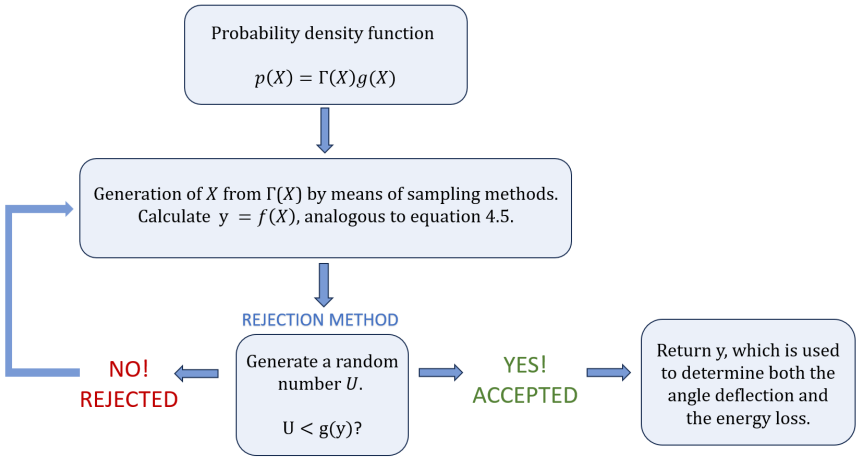

FIGURE 4.3: A schematic representation exemplifying how PENELOPE operates during photon simulations.

extension *.in, structured into distinct ordered sections to enhance the user's simulation experience. The layout of this text file is depicted in Figure 4.4.

Upon executing the input file, the program generates an output file that allows users to monitor the simulation's progress and verify the processed data against the initially anticipated input. Furthermore, by reviewing the final sections of the PenEasy output file, users can promptly identify potential errors or discrepancies in data entry.

Additionally, *dump* files and *dat* files are generated. The former provides a snapshot of the code's state at regular time intervals at the end of the simulation. This feature is particularly useful when simulations conclude before attaining the desired statistical precision. With *dump* files, users can resume calculations from the precise point at which they were interrupted. The latter, *dat* files, contain data derived from dosimetric calculations based on the performed tallies.

The subsequent sections will focus on four significant parts of the input file: source models, geometry, transport parameters and tallies. However, only the settings relevant to this study will be highlighted, with some details omitted.

4.2.2 Source Models

There are two distinct methods for specifying the simulation source: Source Box-Isotropic-Gauss-Spectrum (BIGS) and Source Phase Space File (PSF). If both models are enabled simultaneously, an error will occur and the code will terminate.

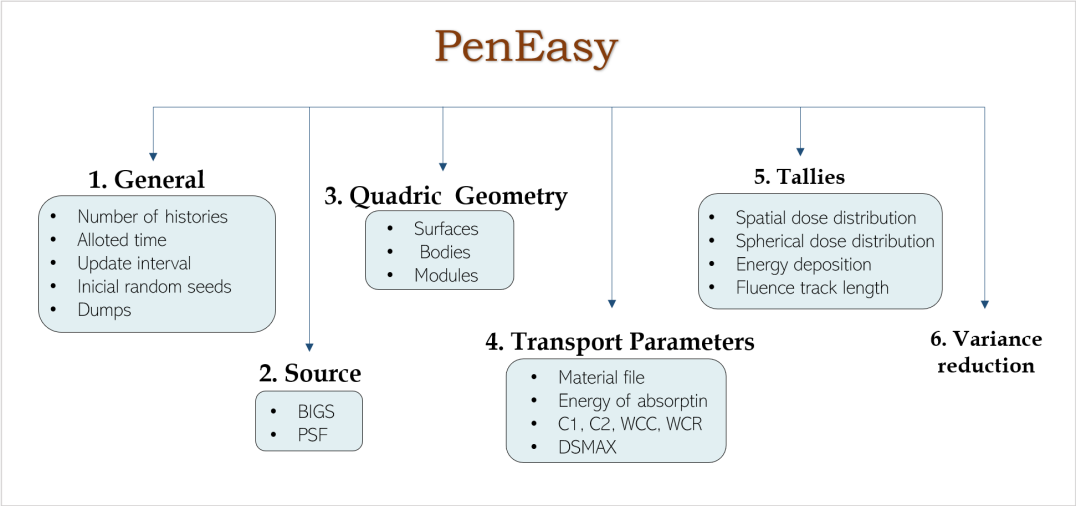

FIGURE 4.4: Tree diagram illustrating the structure of the PenEasy input file.

The key distinction between these two models is that the PSF source necessitates the incorporation of an external file, whereas the BIGS source is established within the program by defining several parameters. Moreover, the BIGS source can be conveniently replicated to generate multiple primary particles per iteration, making it a more versatile model.

Source Box-Isotropic-Gauss-Spectrum (BIGS)

When defining a radiation source, it's crucial to specify the particle type of the initial radiation. In PENELOPE coding, electrons, photons, and positrons are respectively represented by the numbers 1, 2, and 3.

Next, it is mandatory to describe the spatial position of the radiation source. The BIGS model assumes that particle positions are generated inside a cuboid, known as the source box, whose center coordinates and size must be determined. One advantage of the BIGS model is that it allows the rotation and translation of the box center position, covering a wide range of possible configurations of the source.

Due to the possibility of the box source overlapping with various geometry components of different materials, PenEasy includes a setting called "source material" that modifies the portion of the box that actually serves as the source. As a result, the source can encompass the entirety of the box, regardless of the material in which it is positioned, or it can be limited to the region aligned with the specified material. In scenarios where the source box contains multiple geometries constructed from the same material, the "source

material" option can be employed to adjust the source volume and achieve the desired shape.

Additionally, the emitted particles from the source must possess a specific emission direction. This direction is characterized by three sets of coordinates: the "direction vector", followed by the "direction polar angle interval", and finally, the "direction azimuthal angle interval". The initial set determines the coordinates of the reference vector, from which the angles are calculated. The spherical window established by the angle limits ensures isotropic particle emission. The polar angle set comprises two values, θ_0 and θ_1, both falling within the interval of $[0°, 180°]$, while the azimuthal angle set is determined by ϕ_0 and $\Delta\phi$, which can assume values within the range of $[0°, 360°]$.

Energy is another fundamental aspect of the source. The primary particles generated possess an energy spectrum defined by two columns of numbers: one indicating the initial energy of a channel and the other representing the unnormalized probability. As long as the probabilities remain non-negative, the software proceeds to normalize them. If a negative probability is encountered, the list is terminated, indicating the completion of the energy spectrum construction.

Through the particle type, spatial position, emission direction, and energy spectrum, the source attains complete definition.

Source Phase Space File (PSF)

The initial particle states in this source model are obtained from an external phase-space file (PSF), as indicated in the PSF FILENAME field. This file is constituted by fifteen columns, indicated in Table 4.2. The position vector and flight direction of each particle are obtained from the PSF and are rotated depending on the Euler angles. After the rotation, all particle locations may be modified by applying a translation.

The current history number N is adjusted by the Fortran code of the PSF source model to match the value in the "parent" simulation. For this, PenEasy has established the variable "dn" to represent the increase in the history number compared to the previous record. Since the main program automatically increments N by one unit, it is essential to subtract one unit from N every time the source routine is invoked. For instance, N will rise by 4 units if dn=5 [44].

Columns	Meaning
K	Type of particle
E	Particle energy (eV)
X, Y, Z	3 position coordinates (cm)
U, V, W	3 direction cosines of the direction of movement
WGHT	Particle weight when using variance reduction methods
Delta N	Increment in history number with respect to the previous record
ILB(5)	5 labels that describe the origin of secondary particles

TABLE 4.2: Labels of the columns presented in a Phase Space File produced by PenEasy.

As indicated in the final row of Table 4.2, five labels provide a description of the origin of secondary particles. This becomes especially valuable when examining partial contributions from particles.

The initial element, ILB_1, can assume the value of 1 if it relates to a primary particle or 2 if the particle is a direct descendent. In the latter case, ILB_2 denotes the parent particle's type (1, 2, or 3), while ILB_3 stands for the interaction mechanism responsible for generating the particle (labeled in accordance with table C.3). Moreover, ILB_4 takes a numerical value calculated through Equation 4.7, where Z is the atomic number, and IS_i represents the labels of the active atomic electron shells (referred to in the Table C.2). Lastly, ILB_5 is an arbitrary label defined by the user to identify the particle's descendants.

$$ILB_4 = Z \times 10^6 + IS_1 \times 10^4 + IS_2 \times 100 + IS_3 \tag{4.7}$$

4.2.3 Geometry

During practical simulations of radiation transport, the inclusion of geometrical operations are crucial for defining the active medium and its alteration, when particles traverse interfaces. In the context of PENELOPE, these operations are executed by a dedicated Fortran subroutine package called PENGEOM [8]. This section focuses exclusively on the quadric geometry model despite the available of alternative geometry models.

The quadric geometry model characterizes any geometry as a system comprising homogenous bodies enclosed by quadric surfaces. These bodies can be organized into modules, which can then be interconnected with other modules to construct larger, more intricate structures, enhancing computational efficiency. This approach allows the creation of a 3D body with assigned material.

Within the PENGEOM package, bodies are universally bounded by quadric surfaces. Using simple analytical functions to define surfaces simplifies the computation of interface crossings [8]. Consequently, the master equation that governs all surfaces is provided by the "implicit" Equation 4.8.

$$G(\vec{r}) = A_{xx}x^2 + A_{xy}xy + A_{xz}xz + A_{yy}y^2 + A_{yz}yz + A_{zz}z^2 + A_x x + A_y y + A_z z + A_0 \quad (4.8)$$

The geometry's structure demands the use of three separate operations: scaling (S), translating (T) and rotating (R), described by equations 4.9a, 4.9b and 4.9c.

$$\mathbf{S}(\alpha)\vec{r} = (\alpha_x x, \alpha_y y, \alpha_z z) = (x', y', z') \quad (4.9a)$$

$$\mathbf{T}(\mathbf{t})\tilde{\mathbf{r}} = \vec{r} + \vec{t} = (x + t_x, y + t_y, z + t_z) \quad (4.9b)$$

$$\mathbf{R}(\omega, \theta, \phi)\vec{r} = \begin{pmatrix} \cos\phi & -\sin\phi & 0 \\ \sin\phi & \cos\phi & 0 \\ 0 & 0 & \end{pmatrix} \begin{pmatrix} \cos\theta & 0 & \sin\theta \\ 0 & 1 & 0 \\ -\sin\theta & 0 & \cos\theta \end{pmatrix} \begin{pmatrix} \cos\omega & -\sin\omega & 0 \\ \sin\omega & \cos\omega & 0 \\ 0 & 0 & 1 \end{pmatrix} \quad (4.9c)$$

Through the application of these operations, a new surface can be generated, although the order of the transformations should be scale-rotate-translate. This is because the product of the same factors in reverse order transforms the initial vector into a total different result.

These spatial operations can also be applied to the Equation 4.8 in order to obtain a reduced form of the analytical equation of a quadric surface, given by the equation 4.10.

$$G(\vec{r}) = I_1 x^2 + I_2 y^2 + I_3 z^2 + I_4 z + I_5 \quad (4.10)$$

In this reduced form, the indices I_i can only take the values $-1, 0$ or 1. Besides, the equation have central symmetry about the z-axis.

A surface can be defined in implicit form by the function $G(\vec{r}) = 0$, which represents the boundary of two regions. When creating the geometry file, it is important to correctly identify which side of the surface the body encounters. This characterization depends on a parameter called "surface side pointer" (SP). If SP $= -1$ for a point with coordinates b

contained in a body, then $G(b) \leq 0$, indicating that the body is inside the surface. Otherwise, if SP $= +1$, $G(b) > 0$ and the body is outside the surface. Consequently, as a particle crosses a surface, its SP changes. The SP values of the surfaces at the particle's present position must be checked in order to appropriately identify the body through which the particle is traveling.

In the course of a simulation, the computation of where particle track segments meet with boundary surfaces is the primary geometric process that must be repeated many times over. The program determines if the particle track segment crosses any of the surfaces by solving the equation below:

$$G(\vec{r_0} + s\hat{d}) = 0 \tag{4.11}$$

This equation assumes that a particle starts a free flight from a point with coordinates $\vec{r_0}$ and travels a distance s in the direction $\hat{d}$ until it intersects the surface. As a result, $G(\vec{r_0} + s\hat{d})$ is the value of the surface function along the ray. This indicates that a particle will interact with the surface during its free flight of length s_0 if there exists a solution s for Equation 4.11 where $s \leq s_0$. In addition, only intersections ahead of the ray must be considered, hence $s > 0$.

Quadric surfaces are flexible enough to model many material structures because their equation for the ray intersections (Eq. 4.11) is quadratic. For a plane surface, there is only one root, but for other types of surfaces, quadric surfaces consider three potential solutions: if the particle intersects the surface twice, the ray equation has two real roots; if it grazes the surface, there is only one real root with a multiplicity of two; finally, the equation may not have any real roots and the particle does not hit the surface.

Input geometry file

The geometrical model mentioned above introduces its elements through a plain text file named *.geo, made up of a series of blocks that specify the various elements. For the geometry to be correctly read, a separate line filled with zeros must precede and succeed each of the blocks.

Following the "zero segment", there is a 8-character string indicating the type of element (surface, body, or module)*, followed by a 4-character string label present between

*There are other possible types, but they won't be mentioned.

parenthesis. It is imperative to ensure the correct number of characters in each component, even if it is a white-space character because it is critical to successfully define the system. Since modules are constituted by bodies, which are defined through surfaces, the geometry file must have its blocks ordered accordingly.

First, the surface element must have a segment specifying the indices of the quadric structure. If the reduced form (Equation 4.10) is employed, a line like "INDICES=(I1,I2,I3,I4,I5,I6)" must be written, followed by the scaling, rotating and translating transformations mentioned before. When using the implicit form, all indices are set to 0, and the parameters present in Equation 4.10 should be defined below. In this case, there is no need for scaling operations but the other transformations are defined after a line filled with ones. In both cases, these parameters can be entered in any sequence and even more than once, accepting only the last input value. A detail that must be noted is that every numerical parameter must be expressed as a 22-character string; thus when written in scientific notation, a number must have 15 decimal places (format E22.15). Also, each number is enclosed in brackets and has a corresponding 4-character string, separated by a comma, that must be set to zero for the parameter value to be valid.

Secondly, the body should be described through the previously mentioned surfaces. After the definition of the body and its associated label, there is a line specifying the material number. This value should agree with the convention adopted in the "transport parameters" of the simulation, presented in Section 4.2.4. Then, each limiting surface with its side pointer must be written in a line. It is not necessary to declare the limiting bodies because they are supposed to be specified in ascending order. However, all of the components that really restrict the body must be clearly declared in order to speed up computations.

Finally, there is a block for building modules that has the same structure as the body block, with the exception that a module can suffer rotation and translation. These operations must be separated from the remaining components with a line filled with ones.

This arrangement can be repeated to set up the required geometry system. Besides, before the first "zero segment", the document can begin with informative text, as many lines as needed. Also, a brief description can be written at the end of the first line of each element. Additionally, comment lines, starting with "C", "c" or "#", can be included anywhere in the file for a rapid understanding of the geometry.

After executing the input file with the particular geometry attached, an output file including all geometric system information is created. If the geometry file is incorrectly defined, an error warning is displayed in the output, and the simulation does not begin. The PENELOPE distribution package includes an application named GVIEW2D that may be used as a tool to debug the geometry definition file. This utility creates an output file called *geometry.rep* that precisely defines the same geometry as the input file. The programs are terminated when an wrong input format is detected or when an obvious mismatch in the definition file is discovered. Error messages are also written to that file, making it extremely easy to identify discrepancies. When the input file structure is correct, the algorithms continue and the geometry is shown for additional study. Therefore, GVIEW2D enables the detection of faults and inconsistencies in the geometry specification file that may impact the outcomes of real simulations. The image displayed is a map of the bodies or materials that the window plane intersects. The window plane's orientation, as well as the position and size of the window view, may be modified interactively. GVIEW2D enables arbitrary magnification inspection of the system's internal structure, restricted only by the intrinsic resolution of the PENGEOM algorithms.

It is important to note that, even if no error notice is shown, the application may not be considering the geometry correctly. Because the software permits overlapping bodies to be created without causing an error, only one of them is considered in the coincident volume. The bodies that are taken into account depend on how the geometry file was created.

Consider the basic scenario of a tiny sphere trapped within a bigger one. This geometry is as simple as creating two spherical surfaces with varying radius. As previously stated, the bodies are expected to be defined in ascending order to prevent an incorrect specification of volumes. As a result, the smallest sphere must be created first, or else it will not be recognized.

The sequence of definitions of the spheres, however, is insufficient to yield the required geometry. To include the smaller sphere inside the bigger volume, the geometry file may be written in two distinct ways: by defining the value of the SPs to prevent ambiguity of the specified bodies (4.5 on the left) or by including the smaller body at the end (4.5 on the right).

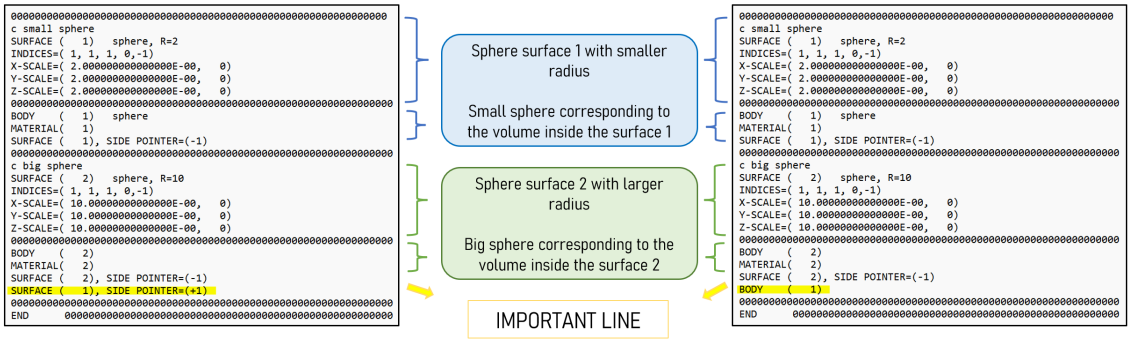

FIGURE 4.5: Two distinct ways of representing the identical geometry file, emphasizing the significance of accurately specifying the superimposed bodies.

4.2.4 Transport Parameters

Apart from geometry, the input file must encompass transport parameters. PenEasy dedicates a section to these configurations, featuring a table with one material per line.

The initial column designates the material index (”MAT#”), represented as a consecutive integer commencing from 1. This index corresponds to the material label specified in the geometry file and is crucial for correctly linking the material to the designated body.

The second column refers to the material data file, which PENELOPE reads to obtain the necessary physical information about each substance. This file, which is commonly identified by the extension ”*.mat,” is created by the auxiliary program ”material,” which makes use of atomic interaction data extracted from the database. This generation process can alternatively involve inputting composition data via keyboard. This entails selecting the number of elements in the molecule and entering their weight percentages (or the chemical stoichiometric formula).

The parameters contained within the remaining columns influence the speed and precision of the simulation for electrons and positrons.

There is a designated column for absorbed energy (EABS) for each particle type. This value is determined either by the specific characteristics of the experiment or the desired spatial resolution [8]. Yet, only radiation possessing energy greater than this threshold can be tracked because the interaction cross-section database covers the energy range above 50 eV. Using different absorption energies in nearby bodies may cause observable artifacts in the way the absorbed dose is distributed spatially. In order to reduce these impacts, it is thus advised to keep absorption energy levels across the region of interest roughly constant.

Two additional columns are designated for parameters associated with hard elastic events. The parameter C1 represents the average angular deflection (C1 $\approx 1 - < \cos\theta >$) resulting from multiple elastic scatterings between successive hard elastic events. This parameter is tied to the corresponding mean free path. Subsequently, the simulation parameter C2 indicates the maximum average fractional energy loss in a single step and it is effective only at high energies. These two settings determine the computer time needed to simulate each track and, ideally, they should not have any influence on the accuracy of the simulation results. PENELOPE admits values of C1 and C2 from 0 up to 0.2, being recommended using the values C1=C2=0.05.

The simulated energy distributions are primarily influenced by the cutoff energies W_{CC} and W_{CR} associated with hard inelastic collisions and hard bremsstrahlung emissions, respectively. Larger cutoff energies speed the simulation, but if they are too large, they might have an adverse effect on the simulated energy distributions. In practice, these values exert a minor influence on the result accuracy as long as they remain below the bin width utilized for computing energy distributions. Consequently, the maximum allowable cutoff energies are determined by the desired energy resolution.

The final necessary parameter is DS_{MAX}, which has already been elucidated in Section 4.1.2. DS_{MAX} determines the maximum permissible step length for electrons and positrons. If this column is left unfilled, PenEasy defaults it to infinity (10^{30}).

To conclude the "Transport parameters" section, there is a column labeled "COMMENTS", designed for users to provide descriptions or notes to enhance comprehension of the simulation details.

4.2.5 Tallies

Generally, the purpose of radiation simulations is the calculation of dosimetric quantities. The act of obtaining data from particle tracks to estimate observable quantities is known as "tallying" and the estimators used for this purpose are known as "tallies" [42].

When using PenEasy, the section for defining the tallying is divided into different types of tallies, each one starting with a STATUS switch that can be ON or OFF. An OFF tally is inactive and won't generate any data reports, while an ON tally creates new files according to the required information. Another feature common to the tallies involving spatial distributions is that they define volume elements, called spatial bins, where the energy deposition is collected. These volumes do not exist in the geometrical description

of the material object given in the GEO file and, therefore, they do not represent a hard boundary for the transport of particles [44]

In this chapter, it will be presented some of the tallies available in PenEasy that were used for this work.

4.2.5.1 Tally Spatial Dose Distribution

Activating this tally permits the calculation of the absorbed dose distribution per history. In this work, it is tallied a 3D distribution, where the intervals and bins for the cartesian coordinates are defined. The mass density of each small volume is given by the material in the center of each bin, assuming it is homogeneous. The file created contains eight columns: six indicating the low and middle positions of each bin for x, y and z axis; one for the dose in the corresponding bin; and the last for the uncertainty of the determined dose. The units of dose are given in eV/g per history.

4.2.5.2 Tally Spherical Dose Distribution

Instead of defining bins in cartesian coordinates, it is possible to calculate the absorbed dose distribution in the radial interval using the Tally Spherical Dose Distribution. Thus, the file created by this tally gives the dose (and respective uncertainty) calculated in a spherical shell defined by low (r_l) and high (r_h) end position. It is printed the average radius of each shell volume given by the expression below.

$$r_{\text{avg}} = \frac{3}{4}\frac{r_h^4 - r_l^4}{r_h^3 - r_l^3}$$

4.2.5.3 Tally Energy Deposition

When the section Tally Energy Deposition is ON, it is created a file with three distinct columns: the first column indicates the label of the material where the tally is being calculated; the second consists in the energy absorbed per history in each material measured in eV; and the third columns represents the uncertainty of the value displayed. To obtain the dose absorbed by a specific material, the values of the second column must be multiplied by the charge of an electron, to convert the energy to Joule, and then divided by the mass of the specific body.

4.2.5.4 Tally Fluence Track Length

This tally creates a file that displays the distance traveled by each particle in a specific material as a function of the energy. The user must define the energy interval and the number of bins that should be considered in the calculation. Since the output of the Tally Fluence Track Length relates to the fluence spectrum integrated over a particular volume, the units correspond to the product between the differential fluence in energy and the volume, that is, $\frac{1}{\text{eVcm}^2} \times \text{cm}^3 = \text{cm/eV}$.

4.2.5.5 Tally Phase Space File

When this tally is activated, a Phase Space File is written, considering the dynamic state of all particles that entered or were created inside a specific material. In this work, the standard PenEasy text format is selected, originating a plain text file where each variable is separated from the next by one or more spaces. Although accessing recorded data takes up a significant portion of the simulation, using the standard format is easier for human reading. Another particularity that should be taken into consideration when using this tally is that the detecting material should be a perfect absorbent. It is undesirable for a scoring particle to create secondary particles downstream, which might then reach and be scored by the detecting material, because when the created PSF is used as a source to a subsequent simulation, these secondary particles would be tallied twice [44]. Thus, all absorption energies for the detecting material must be set to a large number, otherwise the simulation will not start and an error message will be displayed.

Chapter 5

Monte Carlo simulations: results and discussion

5.1 Gold nanoparticle surrounded by water

The first step in this work consisted on evaluating the radiosensitization impact of a single AuNP in water after being exposed to an X-ray beam. The input parameters used were based on another article [19], allowing for comparison and validation of the results.

In terms of the source, an X-ray emitting circle larger by 10 nanometers than the nanoparticle was positioned at a distance of 100 micrometers from its center. Figure 5.4.a provides a clear visual representation of this geometric configuration. Due to PENELOPE's limitation in producing two-dimensional objects, the circular source was constructed by overlaying a sphere with the same radius onto the previously mentioned source box described in Section 4.2.2. In the PenEasy input file, a source box was defined with its center positioned at coordinates $(0, 0, -100)$ µm, and its sides defined within the xy plane. The particle's direction was set to be parallel to the z-axis, resulting in every polar and azimuthal angles set to zero, and the "source material" parameter corresponded to the material of the sphere with the same size and position as the box. In the geometry input file, it was necessary to assign different material labels for this sphere and the external medium, even though both are composed of water. This approach was crucial to ensure that the source emissions were confined to the overlapping region, thus forming a circle. However, this method led to an output error upon executing the PenEasy program. Fortunately, the issue was originated from a few lines of text within the Fortran package (showed in Appendix D.1), which could be easily removed from the file.

As stated in Section 2.3, the output spectrum of an X-ray tube is heterogeneous in energy, showing a continuous distribution of energies for the bremsstrahlung photons superimposed by characteristic radiation of discrete energies. To obtain these spectra, SpekPy was used. Two tube voltages, 50 kVp and 100 kVp, were examined, while maintaining a fixed anode angle of 20° and utilizing a filtration setup of 0.8 mm of beryllium (Be) and 3.9 mm of aluminum (Al). In order to obtain similar spectra to those considered in a reference article [19], the curves obtained for the probability of emitted photons were multiplied by arbitrary factors, resulting in the spectra represented in Figure 5.1. Because this was the first PENELOPE simulation, input parameters were intended to be very similar to those in the article to ensure that the methods implemented might be validated.

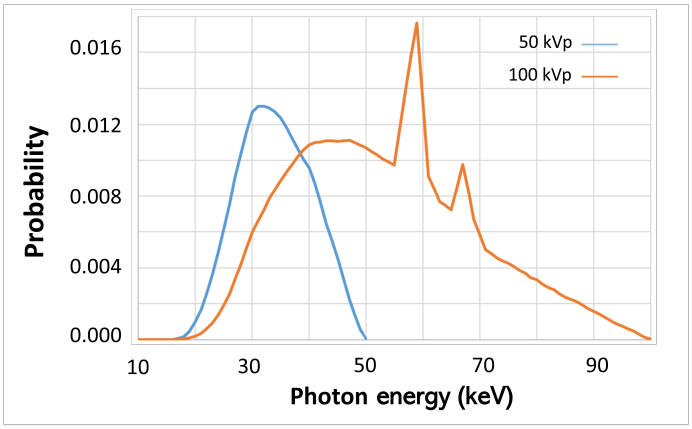

FIGURE 5.1: Output spectra generated using SpekPy for tube voltages of 50 kVp (blue) and 100 kVp (orange).

The system's geometry comprises two concentric spheres with different radii, and its input file resembles the one depicted in Figure 4.5. One sphere represents the gold nanoparticle, with a diameter of 50 or 100 nm, while the other is the external medium, which is water and has a much larger diameter (40 cm). The respective materials, gold and water, were obtained from the database available in PENELOPE.

In Appendix D.2 the input parameters used for these simulations are given. There are two things that are important to mention. Essentially, the absorbed energy of all particles must be adjusted to a minimum of 50 eV. This is due to the fact that gold atoms are expected to optimize the impact of local deposition by generating particles with an extremely low range, i.e., very low energy. Hence, if the absorbed energy is large, materials will absorb energy before these low-energy particles are created, neglecting the local impact of energy deposition. Secondly, the parameter "DSMAX" for gold material should be

small enough to ensure that, in the Monte Carlo simulation, particles do not pass through the nanosphere without noticing it.

The dose around the AuNP was scored in shells (1µm thickness) up to 50 µm from the nanoparticle's center, using the "Tally Spherical Dose Distribution". Absorbed dose was scored in 1000 shells (10 nm thickness) in order to optimize the local energy deposition of Auger electrons close to the AuNp. These data were also tallied in the absence of gold to evaluate the effect of the nanoparticle. Figure 5.2 shows the dose enhancement ratio (DER) (Equation 5.1) for both nano and microscales, considering all possible combinations of energy source and diameter of AuNP.

$$\text{DER} = \frac{\text{Dose in the presence of AuNP}}{\text{Dose without AuNP}} \tag{5.1}$$

Bar errors in each graph were determined with the general propagation of error expressions (see Appendix D.3). Considering D_1 and D_2 as the absorbed dose* in the presence and absence of gold, respectively, with the corresponding uncertainties† (u_1 and u_2), the error (u) for DER is given by:

$$u_{\text{DER}} = \sqrt{\left(\frac{u_1}{D_2}\right)^2 + \left(\frac{D_1}{D_2^2}u_2\right)^2}$$

Figure 5.2 displays the results. The first obvious observation is that the nanometric scale results have much larger associated error than the micrometetric scale ones. This was expected because the dose values calculated by PENELOPE represent an average over the considered volume. In smaller shells, there is a reduced number of particles depositing their energies within the volumes, leading to a reduced number of parcels contributing to the calculation of the mean absorbed dose. Consequently, the associated uncertainties are greater for the values obtained in the nanometric scale.

Furthermore, the shape of the DER curves as a function of radial distance differs slightly between the two scales analyzed. At the nanometric scale, the 50 kVp source shows greater improvement in dose for both sizes of nanoparticle. For distances up to 1 µm (=1000 nm) from the sphere center, the AuNP with 100 nm diameter has a DER about two times greater compared to a diameter of 50 nm. Also, for both sphere sizes, the dose ratio varies more dramatically near the spherical surface. When the 100 kVp source

*To simplify, the term "absorbed dose" will be simply referred to as "dose".

†Uncertainties u_1 and u_2, related to the doses with and without the gold nanoparticle, are obtained in the output tally file created by PenEasy.

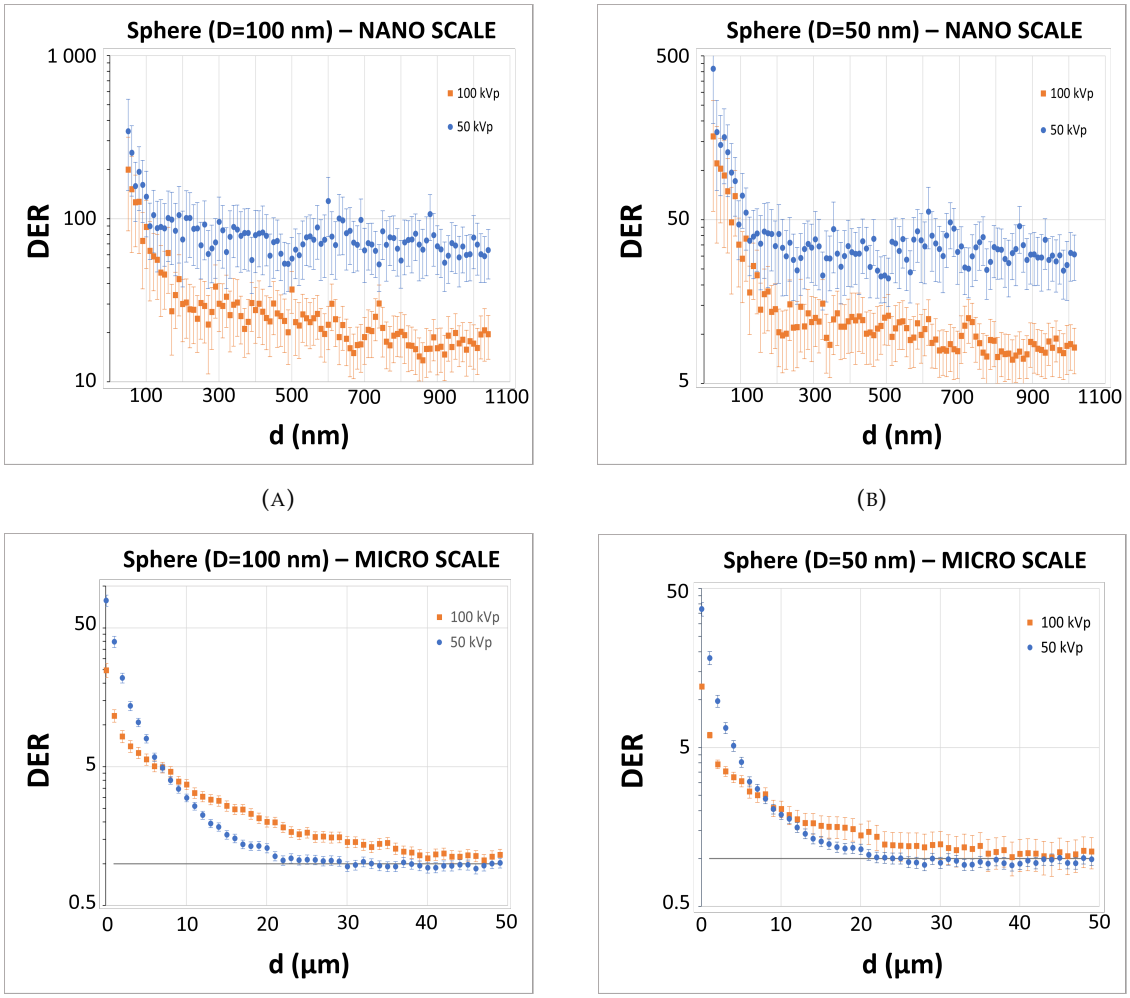

FIGURE 5.2: Dose enhancement ratio for different combinations of energy source and nanoparticle size. a) nanometric scale for $D_{NP} = 100$nm; b) nanometric scale for $D_{NP} = 50$nm; c) micrometric scale for $D_{NP} = 100$nm; d) micrometric scale for $D_{NP} = 50$nm.

is used, DER diminishes by about 85% of its original value in the first 200 nm. If the 50 kVp source is employed, DER decreases by approximately 75% in the first 100 nm. After this notable decline, DER varies slowly until 1 µm distance.

At the micro scale, the size of the AuNP has less impact on the DER, but the large diameter still produces better dose improvement. It turns out that for both AuNP, the 50 kVp source produces more energy at closer distances to the gold sphere and, at distances greater than 10 µm, the most energetic source optimizes dose deposition. Actually, the influence of the gold nanosphere is insignificant from 25 µm, for the less energetic source, while for 100 kVp source, the effect of the AuNps only stops being noticed at distances around 50 µm.

Aside from DER, the electron fluence inside the AuNP was also computed by using

"Tally Fluence track length". Because the output data file created by PenEasy has units of cm/eV, as indicated in Section 4.2.5.4, each value was divided by the AuNP volume and then multiplied by the sectional area irradiated by the source. In this way, the final data corresponds to the probability of emitting an electron per unit energy, which is plotted in Figure 5.3 for both sizes of nanosphere.

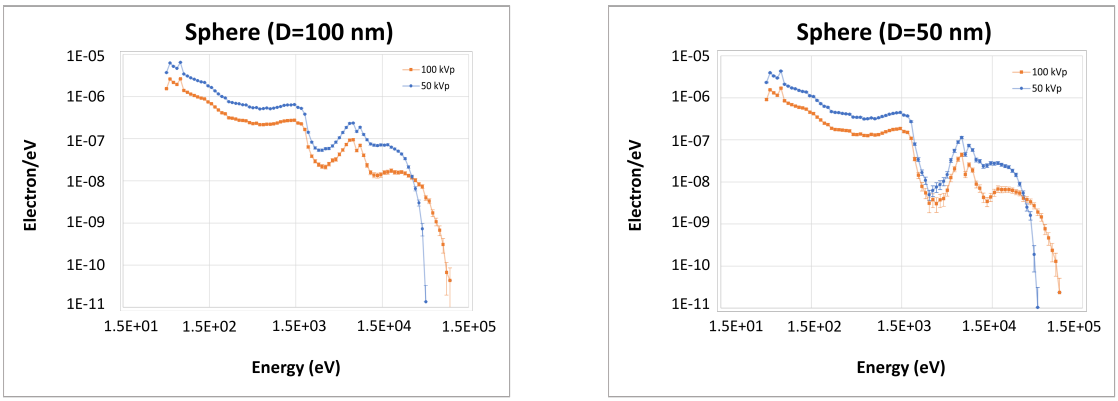

(A) (B)

FIGURE 5.3: Probability of electron emission, considering an irradiation with 50 kVp and 100 kVp X-rays. a) diameter of 100 nm; b) diameter of 50 nm.

It is clear that with both AuNPs, the source of 50 kVp exhibits greater emission probabilities for the same energy bins. This is not valid for energies above 50 keV because the mean energy of the 100 kVp spectrum is higher. Certainly, when the maximum photon energy from a 50 kVp source is 50 keV, it becomes evident that photoelectrons cannot possess energies exceeding this limit. Besides, the distribution has a similar shape for all cases, where less energetic electrons have higher probability (above 10^{-6}) of being emitted. There is a valley observed between [1.5, 5] keV, however the diameter of 50 nm displays a more significant depression. In this region, probabilities go below 10^{-7} and 10^{-8} for diameters of 100 and 50 nanometers, respectively. Following this significant decrease, all graphs exhibit a peak with a characteristic shape at energies ranging from [5, 10] keV.

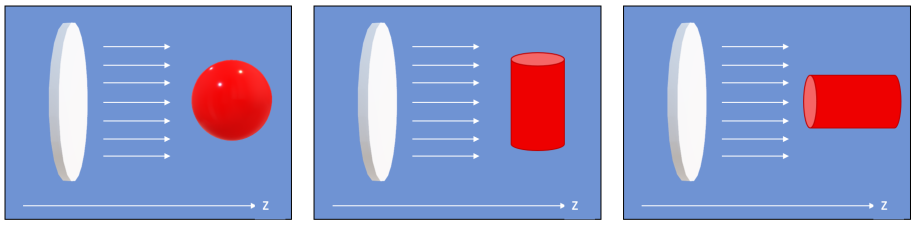

FIGURE 5.4: Geometry setups considered, where the source has a circular shape. a) irradiation of a sphere; b) irradiation of a cylinder through its transversal axis; c) irradiation of a cylinder through its longitudinal axis.

These findings were consistent with the research used for comparison, which had identical input parameters. Thus, the two tallies computed with nanospheres were also applied in a different setup where the AuNP geometry corresponds to a cylinder with diameter of 10 nm and length of 40 nm, that is, with aspect ratio (AR*) equal to 4. The energies of irradiation were the same as the ones used for spheres, the spectra of which are represented in Figure 5.1, and the geometry source was also equivalent. In order to evaluate if the sectional area exposed by the X-ray beam influences the improvement of dose, the nanorod was positioned in two distinct configurations: one with the beam's direction parallel to the transversal axis (5.4.b) of the cylinder and the other with the beam parallel to the longitudinal axis (5.4.c).

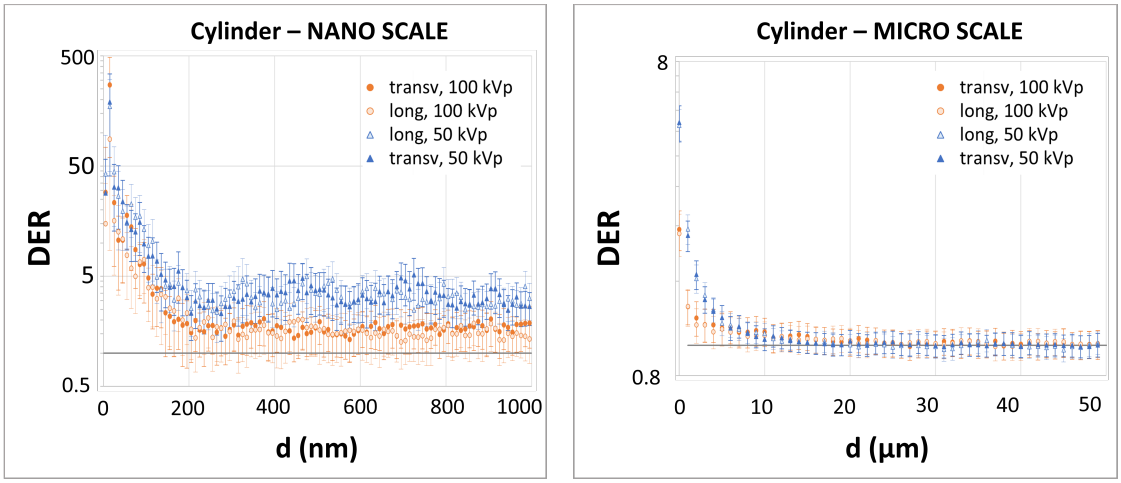

(A) (B)

FIGURE 5.5: Dose enhancement ratio for cylinder irradiations and different energy source. a) 100 shells up to 1 µm distance; b) 50 shells up to 50 µm distance.

The results obtained for DER for both energies and dispositions are illustrated in Figure 5.5. Similarly to nanosphere irradiation, the 50 kVp source is displayed in blue and the

*AR corresponds to the ratio between the length and diameter of the cylinder, also known as a nanorod.

100 kVp source in orange. Irradiation across the nanorod's transversal axis is shown by solid marks, whereas longitudinal irradiation is represented by hollow points. Even at the nano scale, there is no significant difference between the two geometric forms throughout the whole radial distance range. Nevertheless, the less energetic source still shows a better improvement in energy deposition in the vicinity of the AuNP surface. Similarly to what happens with nanospheres, the 50 kVp source is more efficient in dose enhancement up to a distance of 8 µm. Furthermore, at the micro scale, it is visible that the gold nanorod has no effect on energy deposition at distances greater than 10 µm for both sources.

Because longitudinal and transversal irradiation did not show substantial differences in energy improvement near the gold surface, the study of electron emission was limited to transversal irradiation. Figure 5.6 represents the probability of electron emission as a function of energy.

The graph plotted has a similar shape to that obtained for nanospheres, but the probabilities are about one order of magnitude lower. Low-energy electrons still have greater emmission probabilities, and there is also a noticeable decline followed by a distinct peak at the energy interval [1.5, 10] keV. Besides, the maximum energy of the electrons emitted is bigger for spheres.

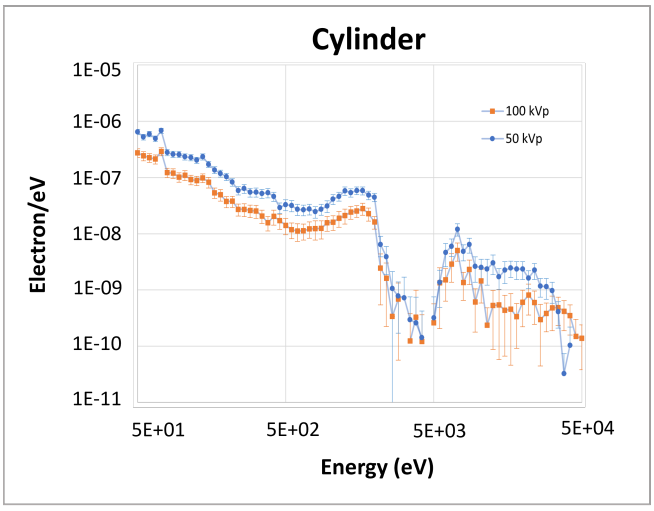

FIGURE 5.6: Probability of electron emission for irradiation through the transversal axis of a cylinder.

For both spherical and cylindrical geometries, the shape of the electron spectra can be correlated with the binding energies of the electrons, as detailed in Table 5.3. When

an electron is emitted with an energy of 150 keV, the photon responsible for its ejection must possess energy at least equal to that energy plus the binding energy of the electron shell. Hence, it becomes more likely for electrons to have considerably lower energy levels since photons with energies as low as a few keV can ionize electrons from the outer shells, specifically O and N. The probability of emitted electrons decreases as their energy increases because there are fewer photons with enough energy to ionize the inner shells. The pronounced dip seen in all cases results from the energy gap between ionizations of the L and M shells. After the valley, there is an increase in emitted electrons with energies around 10 keV. This happens because photons with energies exceeding this limit can ionize the L shell, which contributes to the emission of electrons. Moreover, when the 50 kVp source is employed, the K shell does not contribute to the probability of emitting electrons because its binding energy exceeds the maximum energy of the incident photons. When utilizing the 100 kVp source, ionizations from the K-shell can lead to emitted electrons with a maximum energy of 20 keV. This could provide a plausible explanation for the observed proximity of the spectra at this energy level in Graphs 5.3 and 5.6.

Besides, the almost steady DER at distances from 200 to 700 nm can be attributed to the high probability of electron emission from the outer shells. The energy deposition in those shells is primarily caused by low-energy electrons that end their tracks at those specific distances. From the left side of Figure 3.3, electrons having ranges from 200 to 700 nm have energies approximately in the interval [300, 1000] eV. Electrons with these energies are generated mainly by ionizations from the outer shells.

Given that AuNPs appear to enhance the deposited dose in their immediate surroundings when surrounded by water, and the obtained results align with those in the referenced article [19]), the code used was validated. The subsequent phase involved investigating the influence of gold nanospheres in breast tissue.

5.2 Radiossensitization effect of a single AuNP in breast tissue

The initial step in simulating a single nanoparticle surrounded by breast tissue was to create the material file because this kind of tissue is not included in the PENELOPE material database, contrarily to substances like water and gold.

As mentioned in Section 4.2.4, materials can be generated through the software ”material”, indicating the fraction by weight of each element. This was executed to create the

file "breast.mat", where the composition of tissue was taken from ICRU Report 44 (1989) [45].

In terms of source, the spectrum was generated by SpekPy, using a tube voltage of 50 kVp and equal filtration as indicated in the section above. Though, in simulations with breast tissue, the previously applied multiplication factor was not considered because there was no need to strictly compare results with another study for code validation purposes. Figure 5.7 illustrates the resulting spectrum, which was employed in all simulations involving an external source irradiating AuNPs in a breast tissue medium. The section BIGS was activated, forming a square source with a side of 110 nm defined in the xy-plane. It was positioned at 100 µm distance from the AuNP center with the beam parallel to the z-axis, that is, with direction vector $(0, 0, 1)$ and $\theta_0 = \theta_1 = \phi_0 = \Delta\phi = 0$ (see Section 4.2.2).

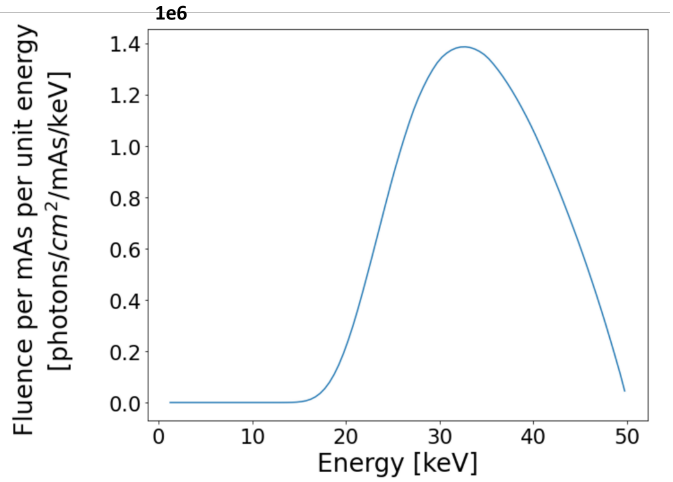

FIGURE 5.7: X-ray spectra obtained by SpekPy, using a tube voltage of 50 kVp.

In the Appendix D.4.1, the input parameters used in simulations involving breast tissue are presented. The setting for absorbed energy ($EABS$) is kept the same as in the simulations with water, as this parameter is crucial for ensuring accurate results, as explained earlier. The parameter "DSMAX" for gold material was adjusted to a lower value than previously employed due to the smaller diameters of nanoparticles considered in these simulations. The "DSMAX" of the breast material does not need to be so small because, although dose is computed in extremely thin shells, in reality, they are not part of the geometry system*. Therefore, to enhance computational efficiency, this parameter,

*Indeed, the body composed of breast tissue material has dimensions much larger than the diameter of the gold nanoparticles.

along with the other parameters, was adjusted to a larger value than previously chosen, while still maintaining output accuracy.

These input settings were consistent for nearly all of the simulations developed when examining the effect of AuNPs in radiosensitizing breast tissue.

5.2.1 Dose enhancement ratio

The geometry file consists of two concentric spheres, one representing the AuNP and the other representing the exterior medium made of breast tissue. The external sphere has a diameter of 20 cm, while the gold sphere has varying diameters of 100, 50, 25, and 12.5 nm. In contrast to the water situation these simulations assumed a tally spherical dose distribution with 1000 concentric shells of 10 nm thickness around the AuNP.

Given that several shells were computed, the PenEasy output data file was read and analyzed in Python. A function called "radial_dose", which is available in Appendix D.4.2, was developed. Its input parameter corresponds to the name of the data report, with "tallySphericalDoseDistrib.dat" as default from PenEasy. The file content is then copied to a string variable **a**. Because there is a qualitative description at the beginning of the document, only the lines with numerical data (from line 12 to 1012) are saved. The variable **L** results from a customized Python function called "split", dividing the entire line into a list, with each list item being a numerical parameter. In this manner, the second, fourth, and fifth columns* are copied to the **R**, **dose** and **error** variables, respectively. Finally, these values are combined into an array and returned as an output.

Figure 5.8 depicts DER data for each diameter of nanoparticle: 100 (dark blue), 50 (green), 25 (red) and 12.5 (black) nanometers. In order to adequately appreciate the differences between every size of AuNP, each graph shows a separate range on the x-axis.

The plot on the left displays DER up to 1 µm, demonstrating that nanoparticles optimise the delivered dose to their surroundings. Their impact is particularly noticeable at the first 200 nm distance, where DER is defined by a sharply sloped line. Larger diameters clearly have a higher DER, since at the first nanoshell around the AuNP energy deposition improves by roughly 300 times. This value is much lower for the diameter of 12.5 nm, which has a DER of 10 in the first nanoshell. For distances between 200 and 700 nanometers, DER seems to be characterised by a steady line. This constant step corresponds to a DER of about 75, 11.5, 2.6 and 1.2 for AuNPs with diameters of 100, 50, 25 and

*Python begins counting indices at zero, thus the first column has index 0, the second has index 1, and so on.

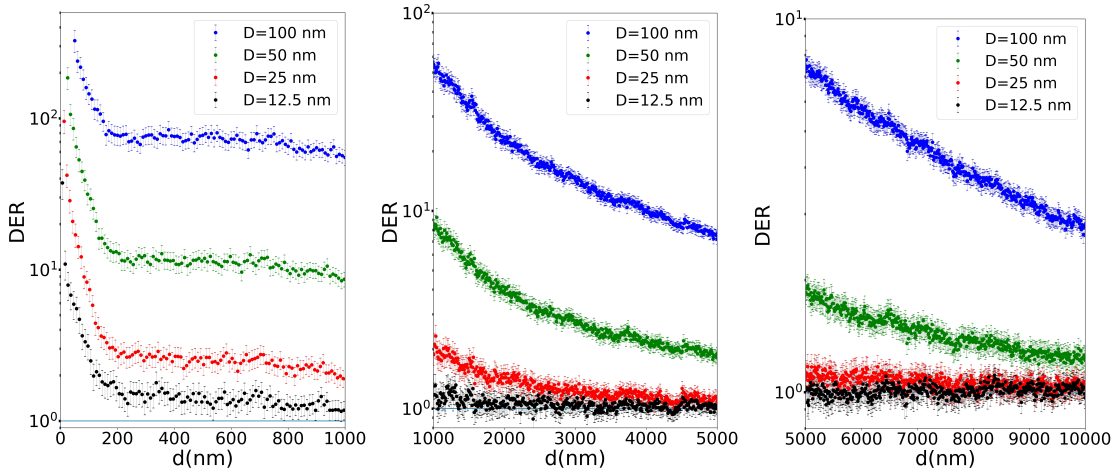

FIGURE 5.8: Dose enhancement ratio in the vicinity of a gold nanoparticle surrounded by breast tissue. a) distances up to 1000 nm; b) distances between 1000 and 5000 nm; c) distances further than 5000 nm.

12.5 nm respectively. Beyond 700 nm, dose enhancement continues to decrease, but at a slower rate compared to shorter distances.

Graph 5.8b focuses on distances ranging from 1 to 5 µm. The energy maximisation is still noticeable for the two largest nanoparticles, with the DER increasing by a factor of 5 when the diameter is doubled from 50 nm to 100 nm. Meanwhile, for shells above 1500 nm distance, the smaller AuNP exhibits negligible dose enhancement. Besides, at 2500 nm, a nanosphere with a diameter of 25 nm begins to have a DER considerably similar to the one obtained with a diameter of 12.5 nm.

Finally, Figure 5.8c shows DER for external shells at distances above 5 µm. Again, the largest AuNP has a considerable impact on energy deposition in the medium. At 10 µm, this nanosphere increases the dose by a factor of 3, a value that is even greater than that observed for a 25 nm diameter particle at half distance. Also, the impact of the two smallest nanospheres becomes indistinguishable at shells distanced further than 7 µm, approximately.

5.2.2 Surrounding Halo

In order to investigate the effects occurring in the vicinity of a AuNP due to interactions between tissue atoms and gold, a Phase Space File (PSF) was generated using the following method.

First, it's crucial to consider that the "Tally Phase Space File" requires a detection material that acts as a complete absorber. Therefore, when the goal is to create a PSF within a halo encompassing the AuNP, the simulation must be divided into two stages. Without this division, when irradiating a nanoparticle using an external source, the particle would be absorbed by the halo before even reaching the gold material. To provide a clearer understanding of the simulation process, refer to Figure 5.9.

The same geometry as the one used in the DER analysis was established to generate a PSF within the AuNP. In the section of transport parameters, the absorption energy for the nanosphere's material was configured to a large value of 5.0E50. This choice ensures the absorption of all particles (see Section 4.2.5.5), thereby recording detailed information about particles entering the nanosphere.

The setup for the second stage included the AuNP and a surrounding halo with an external diameter 20% larger than that of the nanoparticle. In this scenario, rather than utilizing an external source with the spectrum depicted in Figure 5.7, a PSF source corresponding to the file created in the previous simulation was employed. After designating the halo material as a perfect absorber, it was employed as the detection material for generating a second Phase Space File (PSF2).

Combining these two simulations is equivalent to assuming an external X-ray source irradiating a single nanoparticle and then recording particles that exclusively come from the AuNP and enter the halo.

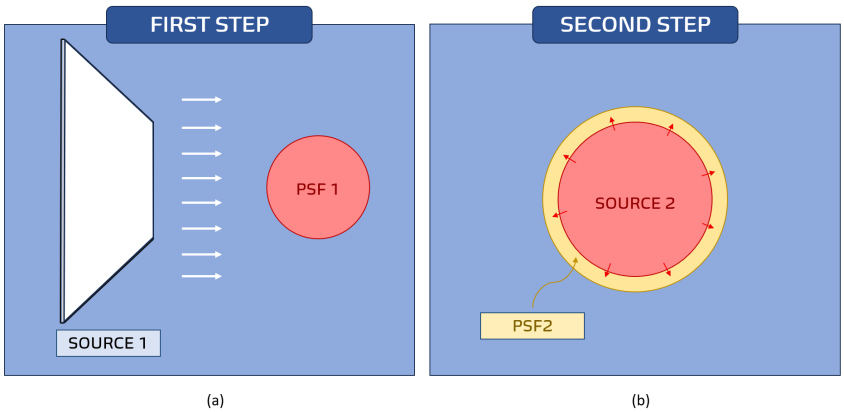

FIGURE 5.9: Scheme for better understanding the method used in the creation of PSFs.

To compare the effects of gold presence and absence, the described process was repeated twice: once with the AuNP and another with the nanosphere's material replaced by tissue. Similar to the DER analysis, diameters of 100, 50, 25, and 12.5 nm were considered. For all sizes, the initial source emitted approximately 1.43×10^8 photons through

the z-axis toward the nanoparticle. Due to the large size of the generated PSF, Python software was employed to analyze the recorded particles. Indeed, Jupyter Notebook might crash or fail to open due to the extensive memory required to store data. Alternatively, such issues might arise from bugs caused by improper closure of the Jupyter file. This problem was resolved by developing new code sourced from [46], available in Appendix D.3.

Apart from those challenges, the examination of the PSF2 was sped up by using the custom function "read_psf" provided in Appendix D.4. The Python "split" function was utilized once again to generate a list for each line in the file. The elements of interest within each list are designed by indices 0, 1, 10, 11, 12, and 13, which correspond to the parameters K, E, ILB_1, ILB_2, ILB_3, and ILB_4, respectively. Further details on these variables can be found in Section 4.2.2.

There are two* basic conditions for each line in the file: either the particle being read is a primary particle (when $\mathrm{ILB}_1 = 1$) or it is not (when ILB_1 differs from 1). In the first scenario, the variable **prim**, which starts at 0, increments by one. Consequently, upon completing the file reading, this variable represents the total count of primary particles. In the second scenario, multiple operations are performed. Specifically, each ILB_3 value is assigned to a variable denoted as **icol**, and all ILB_4 values are appended to a list. Moreover, besides categorizing the particle type, where $K = 1$ denotes electrons and $K = 2$ represents photons, the parent particle's type was also assessed based on the value of ILB_2: if it equals 1, the parent is categorized as an electron, and if it equals 2, it is classified as a photon. Depending on the parent–daughter (PD) combination, the value stored in the variable **icol** is added to one of the following lists: $\mathbf{icol_{ee}}$, $\mathbf{icol_{ep}}$, $\mathbf{icol_{pe}}$, or $\mathbf{icol_{pp}}$, corresponding to PD combinations of electron–electron, electron–photon, photon–electron, and photon–photon, respectively. In this manner, every **icol** list is formed by eight elements, each one corresponding to the counts of a *collision interaction* as described in C.3. These lists maintain the order of PENELOPE, with the first entry referring to ICOL=1, the second to ICOL=2, and so forth. Finally, the mean energy of the secondary particles is determined and separated into two groups: electron energy (**E1**) and photon energy (**E2**).

The input for the function described corresponded to the PSFs generated within the halo. Table 5.1 provides a summary of the results obtained when considering gold in the various cases. The **icol** lists were found to have most of their elements equal to zero.

*The first "if" condition in the function is designed to filter out lines that contain qualitative information rather than quantitative data.

Therefore, in the table, only the processes that were counted are represented. It's important to emphasize that the labels of these processes should be interpreted in relation to the parent particle. In other words, the recorded collision interaction refers to the one responsible for generating the daughter particle.

GOLD						
			D = 100 nm	D = 50 nm	D = 25 nm	D = 12.5 nm
Total of primary particles			92615594	23174117	5797321	1449116
Mean energy of secondary electrons			~ 12 keV	~10.5 keV	~ 8.9 keV	~7.5 keV
Mean energy of secondary photons			~ 9.6 keV	~ 9.5 keV	~ 9.5 keV	~ 9.1 keV
Electrons as parent	Sec. Electron	Hard I.C.	8612	1587	214	18
		Inner-shell I.I	3638	528	65	4
	Sec. Photons	Hard Bremss. Em.	187	13	2	-
		Inner-shell I.I	96	4	1	-
Photon as parent	Sec. Electron	Compton	222	55	16	3
		Photoelectric	238032	35142	4441	333
	Sec. Photons	Photoelectric	40387	5030	514	34
Total of secondary particles			291 174	42 359	5 253	392

TABLE 5.1: Data obtained in the surrounding halo of a gold nanoparticle.

The first thing to note is that the nanosphere with a diameter of 100 nm interacts with more particles due to its larger volume during the initial step of PSF creation. Consequently, it is predicted that the largest AuNP will have a higher number of primary particles recorded in the surrounding shell, which was confirmed. Despite this, the number of detected secondary particles is also higher for the larger diameter, constituting approximately 0.31% of the total detected particles. To put this into perspective, this percentage decreases to 0.18%, 0.08%, and 0.03% for diameters of 50, 25, and 12.5, respectively.

Additionally, the mean energy of the secondary electrons decreases with nanoparticle size, ranging from approximately 12 keV, in the case of the largest size, to 7.5 keV, for the smallest sphere. Conversely, the mean energy of the secondary photons does not vary significantly, maintaining a value of about 9.5 keV, except for the nanoparticle with D = 12.5 nm, which exhibits a value of 9.1 keV.

Regarding the collisions, all diameters produced secondary particles through the same types of interactions. Electrons can be produced through distinct mechanisms. They may originate from an electron parent undergoing a hard inelastic collision or inner-shell ionization interaction. Alternatively, they can be generated when a photon parent is involved

in Compton scattering or photoelectric absorption. Across all the sizes investigated, a consistent pattern emerges: photoelectric absorption yields the greatest quantity of secondary electrons. The left graph in Figure 5.10 visually illustrates this fact for a nanosphere with diameter of 50 nm. The percentages were calculated across all the studied sizes and the interactions bear a similar weight in all cases. Therefore, the graph remains consistent for all sizes and is not represented separately, as it would be redundant to do so.

Previous studies have indicated that, for equivalent incident energy, the rate of photoelectric absorption as a function of nanoparticle size follows a cubic relationship. Indeed, in this study the number of electrons generated by a photoelectric mechanism is proportional to the diameter of the AuNP raised to an exponent of 3.1. However, when considering the total number of generated electrons, the contribution of the photoelectric absorption is approximately the same for all the studied nanoparticle diameters. In the case of the smallest AuNP, it accounts for approximately 93% of the total electrons generated. This percentage shows a slight increase as the nanoparticle size grows, eventually reaching 95% for the largest diameter. The number of electrons produced by inner-shell impact ionization also decreases with the diameter of the nanosphere, representing a percentage ranging from 1.12% to 1.45%. On the other hand, both hard inelastic collisions and Compton scattering produce fewer particles as the nanosphere size increases. Hard inelastic collisions contribute to between 3.44% and 5.03% of the total secondary electrons, whereas Compton scattering produces a number of particles equivalent to 0.09% of the total secondary electrons for the larger AuNP and 0.84% for the smaller one.

In the case of photon generation, the processes leading to their production include hard bremsstrahlung emissions, inner-shell impact ionizations and photoelectric absorptions*. The last process, photoelectric absorption, is the one that produces a larger number of particles, contributing to the generation of more than 99% of the total secondary photons for all diameters. Although the other two processes contribute minimally to photon generation, hard bremsstrahlung emissions generate a slightly higher number of photons.

The PSF generated when replacing gold with breast tissue was also examined and the results are presented in Table 5.2. The table closely resembles the one created for gold, but it excludes the rows corresponding to secondary photons generated by electron parents. The reason for this omission is that these entries were consistently empty for all diameters. The results indicate that the total number of primary particles detected is slightly higher

*These mechanisms may not directly produce the secondary photon but instead initiate de-excitation processes that result in the emission of a photon.

for all AuNP sizes, whereas the total number of secondary particles is significantly lower. The number of secondary photons produced is practically zero, with only a single photon detected at an energy of 0.5 keV for the larger nanoparticle. Regarding secondary electrons, their mean energy does not appear to exhibit a clear relationship with the diameter of the nanosphere. In fact, their energy is higher for diameters of 50 and 12.5 nanometers in the case of breast tissue material, while it is lower for the remaining diameters.

TISSUE						
			D = 100 nm	D = 50 nm	D = 25 nm	D = 12.5 nm
Total of primary particles			92749108	23190569	5798902	1449218
Mean energy of secondary electrons			~ 10.7 keV	~ 11.8 keV	~ 8 keV	~ 13 keV
Mean energy of secondary photons			~ 0.5 keV	-	-	-
Electrons as parent	Sec. Electron	Hard I.C.	5	6	-	-
		Inner-shell I.I	1	1	-	-
Photon as parent	Sec. Electron	Compton	135	33	11	3
		Photoelectric	78	24	4	1
	Sec. Photons	Photoelectric	1	-	-	-
Total of secondary particles			220	64	15	4

TABLE 5.2: Data obtained in the surrounding halo of a nanoparticle made of tissue.

Furthermore, in the case of the two smaller sizes, only a limited number of secondary electrons are detected in the outer shell, primarily resulting from Compton scattering and photoelectric absorption. In contrast, the two larger diameters exhibit secondary electrons produced through similar processes as observed in the case of gold material. However, the contribution of these processes differs from what was previously observed, with varying percentages for each process across different sizes. Nevertheless, it remains consistent that Compton scattering is the primary mechanism responsible for generating the majority of secondary electrons, followed by photoelectric absorption, hard inelastic collision, and inner-shell impact ionization. The right graph in Figure 5.10 illustrates the contribution of these processes to the generation of secondary electrons when considering breast tissue and a diameter of 50 nm. At this size, Compton scattering has a relatively minor contribution compared to the other processes, yet the differences compared to the gold case are substantial. The graphs for the remaining diameters can be found in Appendix D.5. The primary conclusion is that in the presence of gold atoms, the photoelectric phenomenon is maximized, leading to a significant number of emitted electrons, regardless of the nanoparticle's diameter.

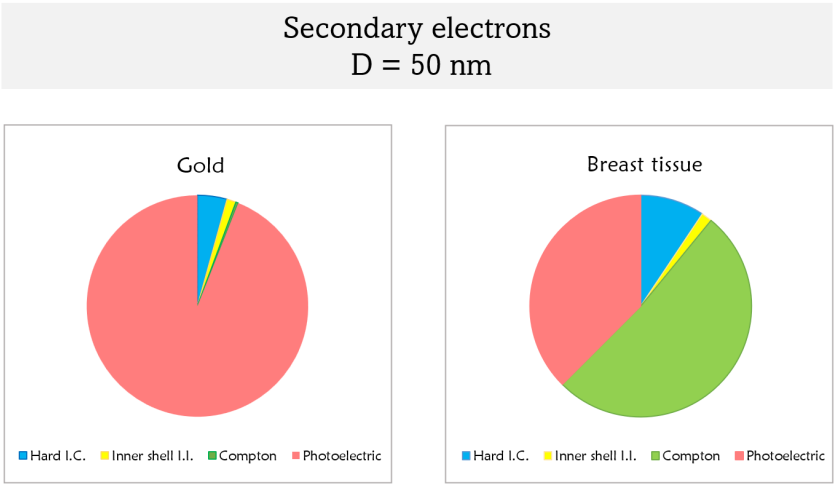

FIGURE 5.10: Contribution of the different interactions for secondary electrons generation in gold (left) and in breast tissue (right).

In addition to the data presented in the aforementioned tables, the "read_psf" function also provides the ILB_4 values. For each material and nanoparticle size, ILB_4 data were analyzed using a custom function called "transitions", which can be found in Appendix D.6. This function initiates by identifying the unique elements within an array, employing Python's built-in function called "unique". Consequently, the variable **labels** captures the ILB_4 list values without any duplicates, while the variable **counts** records the frequency at which each label occurs. Following this, two lists, **co** and **lab**, are generated. The former stores the counts, while the latter stores the corresponding labels. These lists are created exclusively for cases where the counts surpass a specified minimum value, which is determined by the function input parameter represented as **mini**.

Accordingly to Equation 4.7 and assuming that the variable **labs** corresponds to the ILB_4 value, the following relationships can be established*:

$$\begin{cases} z = \text{labs}//10^6 \\ i_1 = (\text{labs} - z10^6)//10^4 \\ i_2 = (\text{labs} - z10^6 - i_1 10^4)//10^2 \\ i_3 = \text{labs} - z10^6 - i_1 10^4 - i_2 10^2 \end{cases}$$

*The symbol "//" corresponds to the floor division, which rounds the result down to the nearest whole number.

The function "transitions" also append the values of z, i_1, i_2, and i_3 to the lists Z, IS_1, IS_2 and IS_3, respectively. In this way, the lists created have integer elements, each one corresponding to a label of a shell, as mentioned in Section 4.2.2. To obtain the labels of the ionization transitions, a function named "shell" was created. This function is available in Appendix D.7 and essentially associates the input numerical label with the corresponding shell.

The atomic transitions associated with the release of the detected particles are displayed in the Tables D.3, D.4, and D.5. These Tables represent only a portion of the total transitions detected. Given the considerably high number of transitions observed when considering gold for all diameters, specific threshold values were chosen for the variable **mini**. These values were 500, 100, 15, and 2 for diameters of 100, 50, 25, and 12.5 nm, respectively. When considering breast tissue material, this minimum threshold was set to 1, displaying all the transitions that occurred. As previously mentioned, these particles are emitted as a result of atomic relaxation events triggered by photoelectric absorption, leading to an initial vacancy in the decaying atom.

For the two smaller sizes, nanospheres made of breast tissue do not produce particles through atomic relaxation. Conversely, for the two larger diameters, particles are emitted due to K-L-L transitions, with the largest diameter showing 2 transitions of the K-L-M type. However, it's important to note that the total number of particles emitted from atomic relaxation is considerably lower when compared to the scenario involving AuNPs. With AuNPs, the number of K-L-L type transitions remains relatively stable, but there is a noticeable increase in transitions among outer shells.

Considering the greater number of particles detected in the halo for larger AuNP sizes, it was expected that the total counts of the shell transitions would also be higher. For instance, the total count of transitions decreased by approximately 500 times when changing from a diameter of 100 nm to 12.5 nm. The counts within the same transition are higher for larger diameters, and there is also an increased number of distinct transitions. However, there is a commonality among the three larger diameters: the L3–M5 transition predominates. In the case of the AuNP with a 100 nm diameter, this transition contributes to 9.9% of the total counts. This percentage decreases to 7.7% for the 50 nm diameter, and further reduces to 5.3% for the 25 nm diameter. In the case of the smaller AuNP, the dominant transition is M5–N6–N7, accounting for 11.7% of the total counts, and the transition L3–M5 comes in second with a contribution of 10.1%.

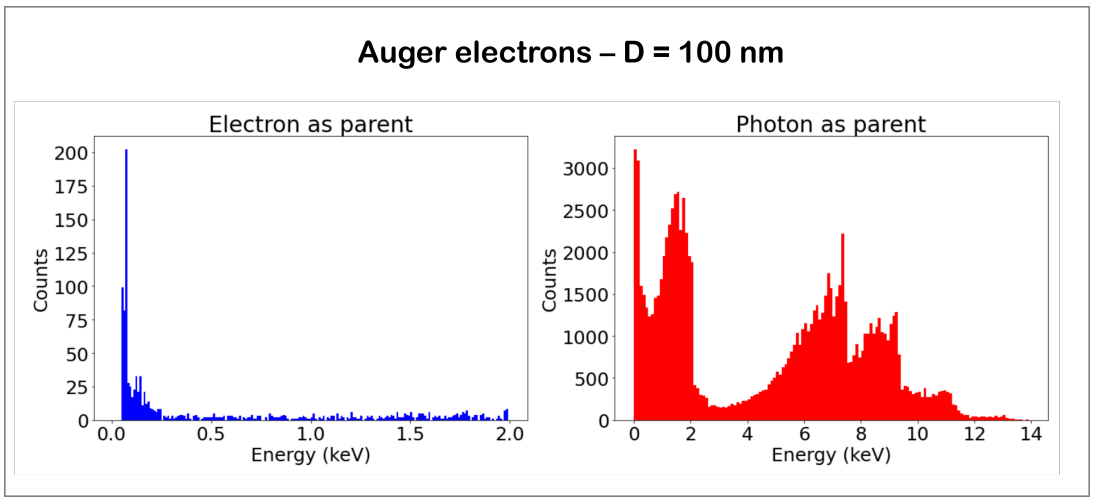

FIGURE 5.11: Spectra of Auger electrons that were detected in the halo surrounding a AuNP with 100 nm diameter.

As the largest AuNP emitted a significant number of electrons, Auger electron spectra were obtained from the surrounding halo. Specifically, electrons recorded in the PSF with a non-zero ILB_4 value were selected, and their energies were extracted. These values were subsequently categorized based on the parent particle responsible for generating the Auger electron. The resulting spectra are illustrated in Figure 5.11. The energies of particles generated by electron parents are considerably lower compared to those generated by photon parents. This implies that mechanisms originating from a photon parent result in transitions that emit a greater amount of energy, subsequently transferred to the emitted Auger electrons. However, it's clear from both graphs that there is a peak in the number of detected electrons at lower energies. The distinctive shape of the right graph can be attributed to the binding energy of atomic shells, given that the majority of Auger electrons are released as a result of cascade processes initiated by the photoelectric effect.

5.3 Survival curves

This section provides a preliminary estimation of survival fractions influenced by the presence of gold nanoparticles. The approach used in this study is based on the Local Effect Model, incorporating certain approximations and simplifications.

The method involves evaluating the spherical dose distribution generated by the gold nanoparticle. These values were obtained from the simulations conducted for DER calculations, specifically, the doses within a sphere with a radius of 1.0E-3 cm around the

AuNP were considered. There were 1000 shells, each one associated with a dose value (d_i).

The doses were divided into bins, meaning that the shells were grouped to create thicker shells with homogeneous doses ($\bar{D}_i$). The survival fraction for each $\bar{D}_i$ was calculated by summing the contributions of every subshell in the following manner. Firstly, each d_i is applied in the linear-quadratic model. Subsequently, an additional term takes into account the fraction f. This value is determined by Equation 5.2, which corresponds to the volume exposed to a specific dose (d_i) divided by the volume of the grouped shells that receive the homogeneous dose.

$$f = \frac{dV_i}{\sum dV_i} = \frac{dV_i}{V_t} \tag{5.2}$$

To better understand this division, please refer to Figure 5.12, which provides a simple example. The thicker shells with homogeneous doses are highlighted in yellow, pink, and blue. Inside the pink shell, three subshells, with doses d_1, d_2, and d_3, are explicitly displayed (where $\bar{D}_2$ corresponds to the average value). These doses are associated with volumes V_1, V_2, and V_3, respectively, and the total volume V_t is the sum of these volumes. Therefore, to calculate the survival curve for the homogeneous dose $\bar{D}_2$, the linear-quadratic model is applied individually to each value of d_i, and then the results are summed.

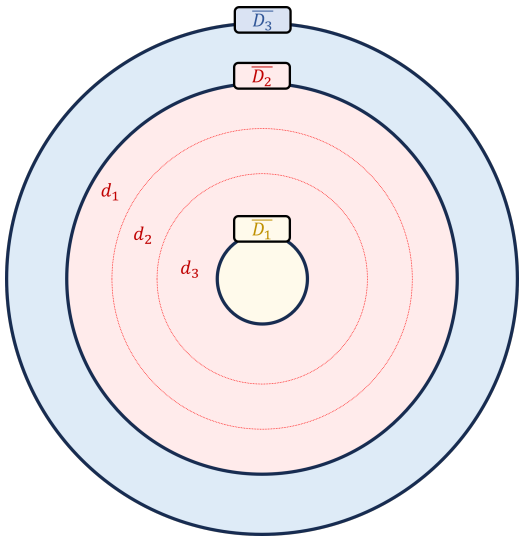

FIGURE 5.12: Diagram illustrating the partitioning in spherical shells surrounding a gold nanoparticle for the application of a model based on LEM.

However, the dose distribution obtained from the Monte Carlo simulation is determined when an external source irradiates the AuNP at 100 µm from its center. In this

way, there are photons emitted by the source that may contribute to the dose without even interacting with the gold nanosphere. For these reason, the exponential factor given by the LQ-model is multiplied by the term ΔN, which is related to the particles that actually interact with the AuNP. Since a single AuNP in the considered volume is not sufficient to draw a curve for all the diameters studied, the number of nanoparticles (NP) is also taked into account in order to obtain reasonable survival curves. In this way, for each group of subshells where the dose could be considered homogeneous, the lethal events are given by Equation 5.3.

$$N_{\text{lethal}}(\bar{D}) = \Delta N \times \text{NP} \times \sum_i (\alpha\, d_i + \beta\, d_i^2)\, \frac{dV_i}{V_t} \tag{5.3}$$

It should be noted that, although this approach is based on LEM, it does not follows the exact same principle. Instead of subdividing the target into a grid, as illustrated in Figure 3.8, a certain volume was divided into groups of shells and the damage induced in that volume was determined based on the spherical dose distribution of just one AuNP. Subsequently, it was assumed that various nanoparticles are concentrated at the center of a tissue sphere, superimposing the effects of each AuNP over the entire tissue volume. The number of lethal events is then proportional to the number of particles and to the particles that interact with them, as each subshell contributes NP times to the calculation.

The value ΔN was determined based on the following assumptions. Firstly, the number of particles that interact with the gold nanoparticle without being absorbed correspond to:

$$\Delta N = N_0[1 - e^{-\mu_{ab} x}]$$

Where μ_{ab} is the linear absorption coefficient of gold, x is the diameter of the AuNP, and N_0 is the total number of particles emitted with direction through the gold nanoparticle. In this case, the number of particles contributing to the deposition of 1 Gy in the tissue was chosen. Thus, the expression above is equivalent to Equation 5.4.

$$\Delta N = N_{1\text{Gy}} \times \frac{\text{AuNP area}}{\text{Source area}} \times \left[1 - \exp\left(-\rho\, x \left(\frac{\mu_{ab}}{\rho}\right)^{\text{Au}}_{30\text{ keV}}\right)\right] \tag{5.4}$$

The mass absorption coefficient is related to an energy of 30 keV, as it corresponds to the mean energy of the X-ray spectrum used as the source. The value for this coefficient, as well as for other materials and energies, can be obtained from [47]. Since the source is

much larger than the gold nanoparticle, the fraction between their areas was considered to discard the emitted particles that travel far away from the gold atoms.

Finally, $N_{1\text{Gy}}$ was determined based on the principle of charged particle equilibrium, where the collisional kerma equals the absorbed dose within the studied cell volume. This assumption is valid because the range of the secondary electrons is smaller than the size of the spherical volume considered, with a radius of 1.0E-3 cm. Additionally, it was assumed that ψ in Equation 2.13 is equivalent to the product of particle fluence (ϕ) and the mean energy of the particles' source ($< E >$). Thus, Equation 2.19 can be expressed as follows:

$$\left(\frac{\mu_{ab}}{\rho}\right)^{t}_{30\text{ keV}} \phi < E >= D \tag{5.5}$$

The mass energy-absorption coefficient is associated with breast tissue (t) and calculated for the specific energy $< E >$. It is important to recall that ϕ represents the number of particles impacting a specific area. Consequently, it yields:

$$\left(\frac{\mu_{ab}}{\rho}\right)^{t}_{30\text{ keV}} \frac{N_0}{A} < E >= D$$

$$\Leftrightarrow N_0 = \frac{A\,D}{< E >}\left[\left(\frac{\mu_{ab}}{\rho}\right)^{t}_{30\text{ keV}}\right]$$

Since primary particles can only interact within an area equivalent to that of the source, $A = A_{\text{source}}$. Based on the values presented in Table 5.3, it can be determined that 1998 particles are emitted by the source in order to deposit 1 Gy in the breast tissue material. This number is significantly lower than the typical number of particles used in dosimetry calculations, mainly due to the nanometric dimensions involved in this case. Finally, the number of particles that interact with the AuNP is obtained using Equation 5.4, where certain values are substituted with those provided in Table 5.3*, and the sizes of the gold nanoparticles studied in the previous section are assumed.

ρ_{Au}	A_{source}	D	$< E >$	$\left(\frac{\mu_{ab}}{\rho}\right)^{Au}_{30\text{ KeV}}$	$\left(\frac{\mu_{ab}}{\rho}\right)^{t}_{30\text{ KeV}}$
19.32 gcm^{-3}	1.21 E-10 cm^2	1 Gy	30 KeV	23.49 cm^2g^{-1}	0.1260 cm^2g^{-1}

TABLE 5.3: Numerical values used for calculation of the Equation 5.3.

*To obtain the correct unit for the number of particles, it is necessary to convert the dose to joules per gram (J/g) and the energy to joules (J).

At this stage, Equation 5.3 can be solved for a specific value of NP, considering each group of subshells with a dose approximately at a constant value. The division into groups was carried out using Python software, with a function named "group", which can be found in Appendix D.8. This function requires three input parameters. The term **bins** represents the dose that delineates a cluster of subshells. In this study, a list ranging from 0 to 10 Gy was employed, with intervals of 0.01 Gy. The **bins** list contains one more element than the number (N) of shells because it includes the null dose. For instance, in Figure 5.12, there are three thick shells, and the **bins** list is defined as $[0, \bar{D}_1, \bar{D}_2, \bar{D}_3]$. It's worth noting that, as PenEasy provides spherical doses in eV per history, these values were multiplied by an arbitrary factor to ensure a sufficient range of dose points, extending up to 10 Gy. This adapted dose list was utilized as the **dose** input parameter in the "group" function. The final input is a list of volumes corresponding to the subshells where the doses were tallied. With these parameters, the function generates two lists, **g** and **dV**, where each element corresponds to the doses and volumes of a cluster of subshells, respectively. Consequently, these variables are created with N elements, each having a length corresponding to the respective number of subshells. In the case illustrated in Figure 5.12, **g** and **dV** appear as follows:

$$g_{\text{group}} = \left[[\bar{D}_1],\ [d_1, d_2, d_3],\ [\bar{D}_3] \right]$$

$$dV_{\text{group}} = \left[[V_{\text{yellow}}],\ [V_1, V_2, V_3],\ [V_{\text{blue}}] \right]$$

This approach allows for the calculation of N_{lethal} according to Equation 5.3 for each thicker shell. Summing the contributions from all subshells, the survival fraction can be computed for each $\bar{D}$ using Equation 5.6.

$$S(\bar{D}) = e^{-N_{\text{lethal}}(\bar{D})} \tag{5.6}$$

The graph in Figure 5.13 displays the data points $(\bar{D}, S(\bar{D}))$ for each of the studied nanoparticle diameters. The variable **NP**, representing the number of nanoparticles, was assigned values of 1, 4, 16, and 64 for nanoparticle diameters of 100, 50, 25, and 12.5 nm, respectively. The legend of the figure expresses this information in terms of concentration,

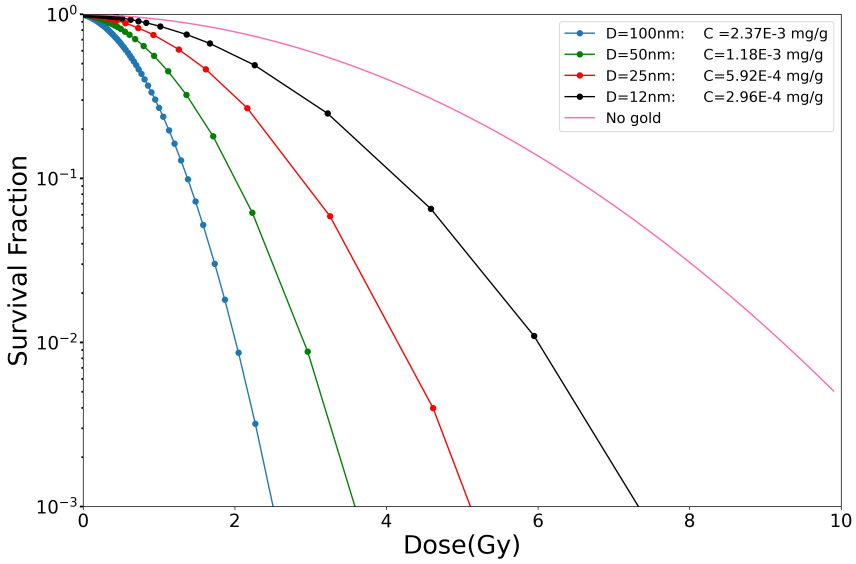

FIGURE 5.13: Survival curves obtained based in the DER around an unique AuNP.

measured in milligrams of gold per gram of tissue (mg/g). It is also illustrated the survival curve for the LQ model applied in breast tissue, using the parameters $\alpha = 0.019$ Kg/J and $\beta = 0.052$ Kg^2/J^2, sourced from [34].

	100 nm	**50 nm**	**25 nm**	**12.5 nm**
α	0.446	0.223	0.112	0.056
β	1.221	0.611	0.306	0.153
SER	5.723	3.815	2.583	1.770

TABLE 5.4: Values obtained for parameters α, β and the calculated SER.

The parameters α and β characteristic of the curves in the presence of gold were determined using Excel. Following this, the area under the curves was calculated to derive the *Sensitizer Enhancement Ratio* (SER). This ratio is obtained by dividing the area under the curve when gold is absent by the area under the curve when gold nanoparticles are present. The results are displayed in Table 5.4.

While the method assumes a concentration of AuNPs at the center of a sphere, superimposing their effects uniformly over the analyzed volume, the results obtained are not necessarily unreasonable. In a study that generated the plots in Figure 3.7, a concentration of 100 nM with 50 nm diameter nanoparticles was assumed, resulting in a SER of 5.97 for a distribution within the nucleus and a SER of 1.77 for a distribution in the cytoplasm.

These values showed a slight decrease with an increase in the energy source. In comparison, this work uses a much higher concentration* and a slightly lower energy source. Additionally, the model employed here does not assume a uniform distribution in the volume of interest. Given the significant differences in environmental parameters and the arrangement of nanoparticles within the cell, the value obtained for the 50 nm nanoparticles cannot be directly compared to that study. Nevertheless, the obtained value of 3.815 is higher than that of the cytoplasm distribution case, which is expected due to the larger concentration used, and still lower than the case of a uniform distribution throughout the nucleus. This is reasonable because the latter scenario induces more damage to the cell. Thus, even with a higher concentration of gold, the radiosensitizing effect does not reach the same level as in the case of an uniform nucleus distribution.

Furthermore, it is evident that the larger nanoparticle size induces more damage in terms of the number of AuNPs per unit volume. Even with just one nanoparticle having a diameter of 100 nm considered, it results in a higher gold concentration within the tissue, leading to a greater survival fraction.

5.4 Distribution of AuNPs in a cell

The subsequent stage of this study involved assessing the impact of a distribution of gold nanospheres within a cell. Based on a previous study [34], an elliptical cell geometry was considered, which is defined by three design parameters: a, b and c radii. These radii define the semi-major and semi-minor axes of an ellipsoid in x, y and z directions, respectively. The cell is defined by the set of all points that satisfy Equation 5.7 with $(a, b, c) = (9.25, 4.25, 1)$ µm.

$$\frac{x^2}{a^2} + \frac{y^2}{b^2} + \frac{z^2}{c^2} \leq 1 \tag{5.7}$$

Instead of a sphere, as in many studies, the nucleus was also described as an ellipsoid with $(a_n, b_n, c_n) = (4, 4, 0.1)$ µm. Figure 5.14(a) shows cell geometry viewed through the z-axis. The input geometry file considers the implicit form defined by Equation 4.8 for the definition of the ellipsoids that limit the cytoplasm (pink) and the nucleus (yellow) of the cell, while the exterior medium (grey) is a sphere described by the induced form (see Appendix D.9).

*The concentration used in this work is about 100 times higher because 100 nM is equivalent to 1.931E-5 mg of gold per gram of breast tissue.

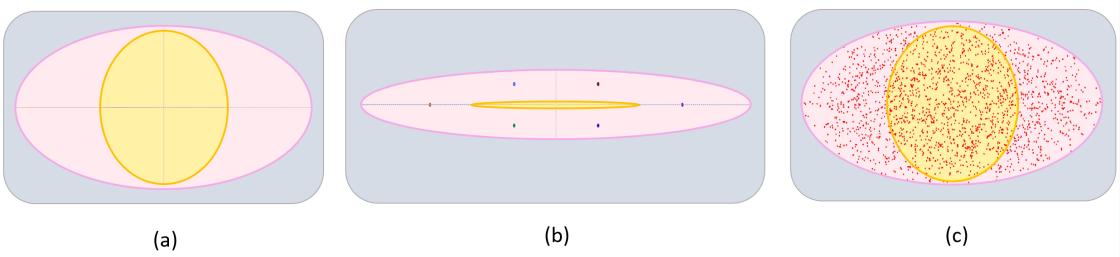

FIGURE 5.14: Cell geometry. a) Vision through the z-axis of a cell in the absence of gold nanoparticles; b) Vision through the y-axis of a cell containing 6 AuNPs; c) Vision through the z-axis of a cell with 2000 AuNPs distributed in the cytoplasm.

The source was located at 100 µm from the cell's centre, forming a square with 20 µm side in the xy-plane and emitting particles with direction parallel to the z-axis. Moreover, section "Tally spatial dose distribution" was activated, dividing the cell's nucleus into 200 voxels and computing the dose deposited in each of them. Both x and y directions were split into 10 bins, while the z direction was divided into two bins.

In Appendix D.10 the Python code used for reading the output data is shown. The function "vox_dose" uses as input the number of histories (**N**), the number of bins for each axis (**xbins**, **ybins** and **zbins**) and the name of the data file. PenEasy creates a document with a 14-line header preceding the numerical data reported in blocks. Similarly to the "radial_dose" function, a variable named **a** corresponds to a string with the document content except the header. Considering **xbins** $= 10$, there are ten lines that modify only the x coordinates while keeping the y and z values constant. When y changes, there is one blank line dividing the blocks; when z changes, there are two blank lines. All the coordinates are in ascending order. The function "vox_dose" creates two matrices with dimensions **xbins** $\times$ **ybins** $\times$ **zbins**. One of the matrices (**mat_dose**) contains the mean dose and the other (**mat_sigma**) contains the corresponding uncertainty. For clarity, Figure 5.15 presents a simplified representation of the output file generated by PenEasy, assuming **xbins** $=$ **ybins** $=$ **zbins** $= 2$. On the right, **mat_dose** is divided into two separate 2D matrices, each having a constant z value. This arrangement mirrors the geometric configuration of the voxel's nucleus.

6 AuNps (D = 100 nm) in the cytoplasm

In the first stage, the dose absorbed in the voxels was compared in the absence of gold and in the presence of six AuNps with diameter of 100 nm. The nanospheres were located in the cytoplasm at coordinates (µm): (-6,0,0), (6,0,0), (-2,0,-0.6), (2,0,-0.6), (-2,0,0.6) and

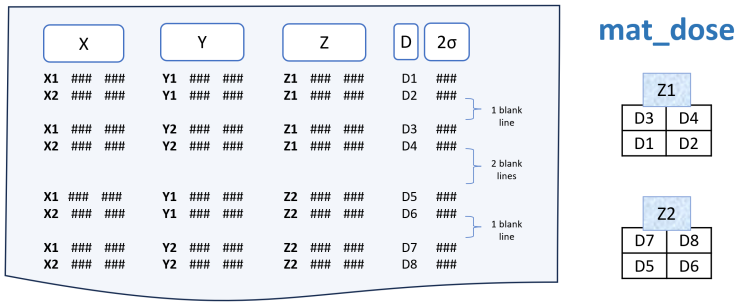

FIGURE 5.15: Example of the structure of a PSF, as well as the creation of the matrix "mat_dose".

(2,0,0.6), as shown in Figure 5.14(b). Mean doses were grouped forming an histogram*, which is represented in figure 5.16.

The dose in each voxel is normally distributed with a mean and a double standard deviation corresponding to the two last columns in the output file (see Figure 5.15). Because the volume of the voxels is very small, only a small fraction of the simulated tracks contribute to the partial scores [8], thus the dose detected has a considerable statistical uncertainty associated with it. As a result, rather than fitting a curve to the histogram with the mean doses, it is reasonable to superimpose all of the probability distributions to get a more plausible curve that reflects the data (including uncertainties). Figure D.11 displays, on the left, an example of 10 dose values with the respective probability distributions and, on the right, the curve resulting from their sum. This method was applied†, resulting the lines traced in Figure 5.16, with the respective means (μ) and standard deviations (σ).

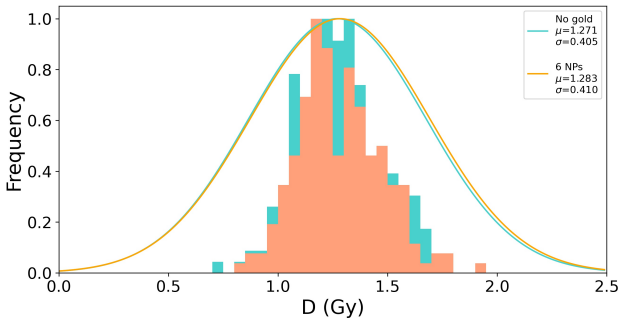

FIGURE 5.16: Histogram of the dose deposited in the voxels that constitute the nucleus for the case of 6 AuNPs distributed in a cell.

*The values given by PenEasy have units of dose per history. It was considered an arbitrary number of 10^7 histories in order to obtain a dose around 1 Gy in the case of absence of gold.

†The probability function considered a confidence of 95.4% for each dose (corresponding to 2σ).

In both scenarios, whether in the absence of gold or in the presence of 6 AuNPs, the dose distribution within the nucleus conforms to a normal distribution. The curves have a center around 1.2 Gy with a standard deviation of approximately 0.4. Although the mean value obtained in the absence of gold is slightly lower, and there is a slight rightward shift in the orange line, these differences are not considered significant.

Despite the presence of only six nanoparticles dispersed in the cytoplasm, their positions are relatively close to the sensitive target. Specifically, the maximum distance to the center of the nucleus is 6 µm. As illustrated in the right plot of Figure 5.8, a gold nanoparticle with a diameter of 100 nm still causes significant damage at such distances. However, it's essential to take into account that the DER calculations were based on a source significantly smaller than the one used for cell irradiation. Consequently, the incident particles were well-directed to interact with the AuNPs, thereby increasing the energy deposition. The doses obtained in this simulation, despite the substantial uncertainties involved, indicate that six nanoparticles with a diameter of 100 nm are insufficient to induce significant damage to the nucleus, even when positioned in close proximity.

2000 AuNPs in the cytoplasm

Since there was no significant dose enhancement observed in the preceding scenario, 2000 nanoparticles were distributed in cytoplasm and the scattering code may be found at Appendix D.12. The coordinates of AuNPs location were determined using the Python package "random.uniform".

Initially, a function named "aleat_cell" was defined, which provides the coordinates of a sample located within an ellipsoid defined by the parameters **a**, **b**, and **c**. To accomplish this, a sample (**num**) with uniform distribution is created over the interval [-1,1]. This sample is then employed to calculate the polar angle as $\boldsymbol{\theta} = \arcsin(\mathbf{num})$. Afterward, the azimuthal angle (ϕ) is generated using a uniform distribution within the range [0, 2π]. Finally, the variable **rad** is computed as the cube root of a sample drawn from a uniform distribution over the interval from 0 to 1. To establish the coordinates $(\mathbf{x}, \mathbf{y}, \mathbf{z})$, the angles and the radius are interrelated through the following equations:

$$\begin{cases} \mathbf{x} = \mathbf{a} \times \text{rad} \times \cos\phi \times \cos\theta \\ \mathbf{y} = \mathbf{b} \times \text{rad} \times \sin\phi \times \cos\theta \\ \mathbf{z} = \mathbf{c} \times \text{rad} \times \sin\theta \end{cases}$$

Because AuNPs are only expected to be scattered in the cytoplasm, a function named "nucleus" was built, which returns 1 if the sample is inside the nucleus and 0 otherwise. Basically, this function verifies if the coordinates $(\mathbf{x}, \mathbf{y}, \mathbf{z})$ given by "aleat_cell" do not follow Equation 5.7 for the nucleus parameters $\mathbf{a_n}, \mathbf{b_n}$ and $\mathbf{c_n}$. If the generated points fall within the ellipsoid that limits the nucleus, that position is rejected, and a new set of coordinates is generated. This iterative process continues until a total of 2000 spots are sampled.

Having the location of each nanoparticle, the input geometry file must be written. Due to the large number of spheres, this file was produced using Python programming rather than being done manually. Basically, the function "sphere" shown in Appendix D.13 returns the lines that must be written to define a single sphere. For that, the function requires six input parameters: body label (**n**), material label (**mat**), sphere radius (**R**) and its positional coordinates (**xx**, **yy**, and **zz**). Depending on the value of **n**, the construction of certain lines, specifically **L2**, **L11**, and **s1**, may undergo alterations. This variability arises because **n** can be a numerical value composed of one, two, three, or four characters, and this must be taken into consideration to ensure the proper spacing of elements within a line. Likewise, lines **L7**, **L8**, and **L9** are built depending on **xx**, **yy** and **zz**, respectively, because the minus character (-) must be taken into account if a coordinate is negative. As indicated in Section 4.2.3, white-space characters are vital to the accurate reading of the input geometry file; therefore, these considerations are very important to execute PENGEOM without errors.

The geometry consisting of 2000 AuNPs is formed by the lines generated through the "sphere" function within a loop. During each iteration of the loop, the variable **n** increases by one unit, while **mat** and **R** remain constant, representing the gold material and the radius of the AuNPs, respectively. The coordinates are determined based on positions sampled by the "aleat_cell" function. After the nanospheres, the cytoplasm and nucleus are defined in the same manner as when AuNPs were not present, using the implicit form. However, because these bodies overlap into the volumes of the spheres, it is crucial to include the "important lines" analogous to the example illustrated in Figure 4.5. When several bodies are inserted in an ellipsoid, it is safer to employ the method shown in Figure 4.5 on the right, which involves writing many "important lines" from 1

to 2000 after defining the cytoplasm. Without this detail, the geometry file won't be read correctly even if there isn't an error message, making it impossible to get accurate results.

The method described results in Figure 5.14.c), that contains a distribution of 2000 nanoparticles viewed through the z-axis. Because the image shows the overlapping of numerous xy-planes, nanospheres are illustrated in the nucleus area, even though their distribution is solely in the cytoplasm.

The cell nucleus was once again divided into small voxels, and the "Tally spatial dose distribution" section was ON. In this stage, nanoparticles with diameter of 50 nm were used, corresponding to a concentration of 15.3 mg of gold per cm^3 of cell. The histogram of the detected doses within the nucleus is presented on the left of Figure 5.17. The soft-colored background results from the superimposition of the probability distributions of each dose, as explained earlier. The line displayed represents the best-fit curve obtained to account for the uncertainties in the distribution.

Although using a diameter of 100 nm results in a concentration of 120 mg/cm^3, which is not applicable in real situations, this scenario was also considered in order to compare dose results between the same number of AuNps with different sizes. As the particles emitted from the source irradiate the entire cell, which is significantly larger than the nanoparticles, the likelihood of a photon interacting with an AuNP diminishes as the size of the AuNP decreases. Consequently, using smaller diameters results in a substantial increase in computational time required to achieve an acceptable level of accuracy. The outcome obtained for nanoparticles with a diameter of 100 nm is depicted at the center of Figure 5.17.

Additionally, the graph on the right side of Figure 5.17 displays the distributions adjusted for the obtained doses. This comparison enables the assessment of the doses detected in the absence of gold in contrast to the presence of 2000 AuNPs.

The doses acquired for the scenario involving AuNPs with a 50 nm diameter follow a normal probability density function, with a mean of 2.41 Gy and a standard deviation of 0.88 Gy. Despite the considerable uncertainty, when compared to the case without gold, nanoparticles of that diameter appear to enhance nucleus damage when distributed solely within the cytoplasm. In the case of particles with a 100 nanometer diameter, the results highlight the effects of gold atoms even more prominently. The histogram exhibits dose values that are widely distributed, forming a relatively flat bell curve, which resembles a log-normal distribution. The parameters *s*, *loc* and *scale* are explicitly explained in

Appendix D.4.5). The data enabled the calculation of a mean dose of approximately 11.8 Gy and a standard deviation of 5.1 Gy, clearly indicating a significant increase in nucleus damage.

In addition to assessing the dose distribution within the smaller compartments of the nucleus, the total absorbed dose by that sensitive target was also determined. Rather than summing the doses detected by the voxels, the "Tally energy deposition" section was used due to its smaller associated uncertainties and the ease of interpretation of the output file. Figure 5.18 illustrates the results for the four previously described situations, with the consideration of 10^7 histories to attain a dose of approximately 1 Gy for the cell without AuNPs.

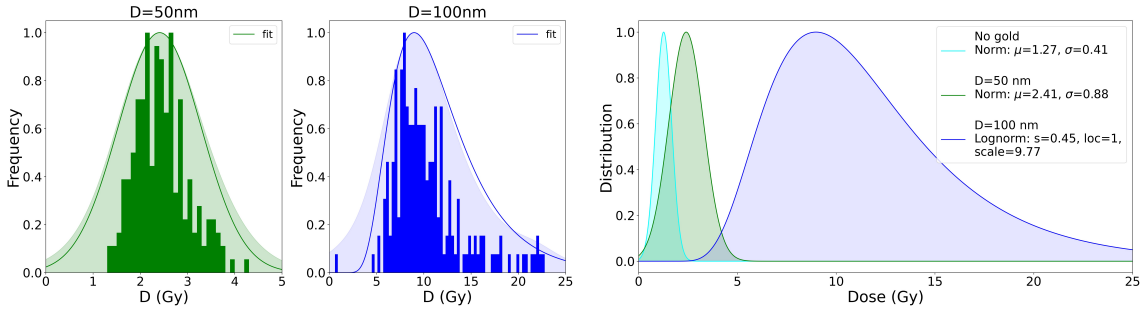

FIGURE 5.17: Histogram and adjusted PDF curve for a distribution of 2000 AuNPs with diameter of 50 nm (left) and 100 nm (center). On the right, their distributions are illustrated together with the case of absence of gold for comparison.

The first noteworthy observation is that the dark blue bar, corresponding to 2000 AuNPs with a 100 nm diameter, is significantly taller than the others, reaching a dose of 9 Gy. Therefore, even though this concentration is not applicable in a real-world scenario, the influence of gold atoms on the radiation increase is evident, as the AuNPs impact a body that is not in direct contact with them. In the scenario involving the distribution of 2000 nanoparticles with half the diameter, the gold concentration consists on a mass weight condition of approximately 1.5%, which is comparable to the gold concentrations achieved in vivo for tumors [29]. Consequently, despite the significant difference in dose compared to the case using the same number of nanoparticles but with a larger diameter, the dose still doubles in comparison to the cell without gold. On the other hand, the orange bar, representing six AuNPs with a diameter of 100 nm, shows no significant differences when compared to the case without gold, confirming the results mentioned earlier.

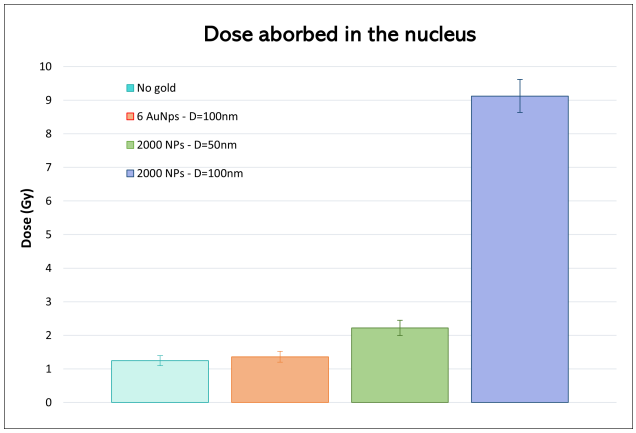

FIGURE 5.18: Energy deposition in the nucleus for different distributions of AuNPs in a cell.

Equivalent mass of nanoparticles

Aside from the simulations described, three alternative scenarios were considered. However, calculating the dose detected by very small voxels through the use of the "Tally spatial dose distribution" demands a significant amount of computational time. Therefore, in the subsequent cases, only "Tally energy deposition" is being utilized.

Considering the impracticality of the scenario involving 2000 large-sized AuNPs and the favorable results obtained with 50 nm nanoparticles, an equivalent concentration of the latter scenario using nanoparticles with a diameter of 100 nm was implemented. This enables a comparison of the radiosensitization effect using the same mass of gold but with two different nanosphere sizes. The results are presented on the left side of Figure 5.19. The dose obtained for the larger nanoparticles with a 100 nm diameter is similar to that obtained for 50 nm AuNPs, both reaching approximately 2.2 Gy in the nucleus.

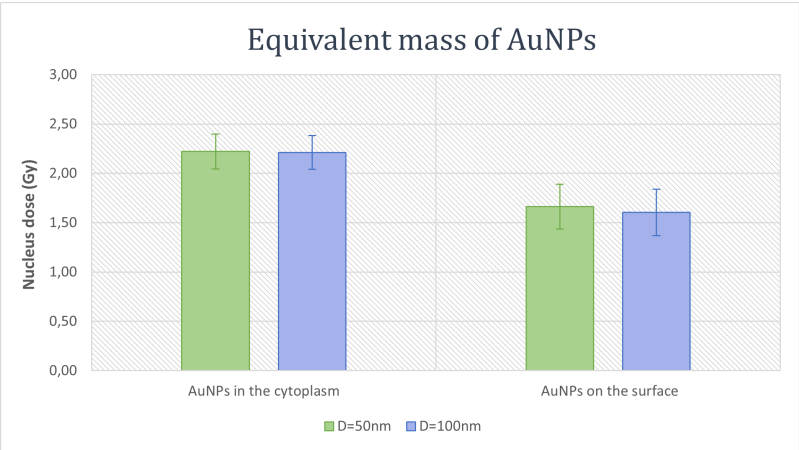

FIGURE 5.19: Dose absorbed by the nucleus for the same concentration of gold nanoparticles with different diameters in the cytoplasm (left) and on the surface (right).

Furthermore, the same concentration for both sizes was employed in a distribution on the cell's surface rather than a distribution within the cytoplasm. In these instances, the absorbed dose was also computed within the nucleus to assess the influence of AuNPs when they are distributed in the external medium, distant from the sensitive target. For the scattering, the same method as previously described was employed, with the exception that the variable **rad** was set to a value of 1 instead of being randomly sampled with a uniform distribution. Subsequently, the positions of the nanospheres are generated, and the function "spheres" is employed to construct the input geometry file. The resulting scattering is illustrated in Figure 5.20, where the left side depicts the distribution within the cytoplasm, and the right side displays the distribution on the surface.

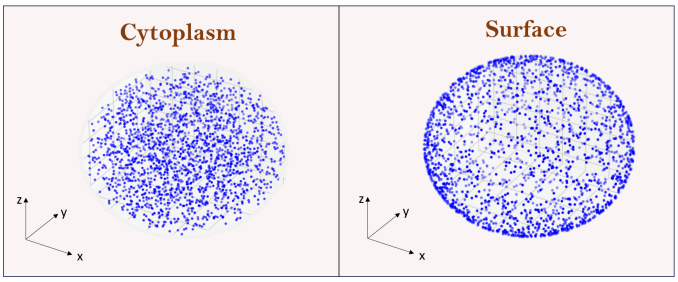

FIGURE 5.20: Scheme representing the distribution of 2000 AuNPs in the cytoplasm (left) and on the surface of a cell (right).

The results comparing the two studied diameters are illustrated on the right side of Figure 5.19. It is demonstrated that, once more, both sizes deliver approximately the same amount of energy to the nucleus. However, distributing nanoparticles on the cell surface has a minor impact on the absorbed dose in the nucleus compared to distributing them within the cytoplasm for both examined sizes. In this geometric configuration, the doses only reach slightly over 1.5 Gy.

Nevertheless, when compared to the first bar in Figure 5.18 (related to the case without AuNPs), all the distributions examined in this subsection demonstrate higher dose values. Consequently, even when nanoparticles are distributed in the external medium, there is clear evidence of dose enhancement attributed to the presence of gold nanospheres.

Chapter 6

Conclusion

This work conducted various simulations that provide evidence of the radiosensitizing effect of AuNPs in their surrounding medium.

Compared to a tube voltage of 100 kVp, the 50 kVp source emits a greater number of low-energy electrons in a water medium, resulting in a higher DER within the first 8 µm distance from the nanoparticle. This observation supports the notion that low-energy electrons have a substantial impact on increasing energy deposition in the vicinity of AuNPs. Additionally, it was observed that irradiating a nanorod with a diameter of 10 nm and a length of 40 nm along its longitudinal axis produces the same DER outcomes as irradiating it along its transverse axis. In the simulations conducted within a water medium, it was also concluded that smaller volumes result in lower enhancement doses and have a lower probability of emitting electrons.

In simulations with breast tissue as the medium, it was observed that the DER rapidly decreases within the first 100 nm around the AuNP, remains relatively constant up to a distance of one micrometer, and then decreases proportionally to the inverse square of the distance. When using the same source size, the constant step value decreases with the diameter of the nanoparticle: for the largest AuNP, it is approximately 100, while for the smallest, that value is around 2. For the 100 nm diameter, the influence of gold is significant even at considerable distances from the nanosphere surface. However, for the 50 nm diameter nanosphere, the impact is only mildly noticeable. As for the two smaller sizes, the effect of gold is negligible at substantial distances from the AuNP surface, which can be advantageous for sparing adjacent healthy tissues.

After examining the PSF within a halo surrounding a single AuNP, it was determined

that the detected electrons were generated through four mechanisms: hard inelastic collision, inner-shell ionization, Compton scattering, and photoelectric absorption. When considering a nanosphere composed of breast tissue, it was observed that the primary mechanism generating the detected electrons was Compton scattering, regardless of the nanoparticle size. However, when gold atoms were introduced, photoelectric absorption became the dominant contributor, accounting for 95% of the total electrons generated within the nanoparticle, for every diameters studied. Furthermore, it was noted that the detected particles originate from transitions that primarily involve the outer electron shells of the gold atoms. Notably, a consistent transition, namely the L3–M5 transition, was observed across all studied diameters.

Revisiting the investigation of effects in the vicinity of a single nanoparticle, a method based on the LEM was employed to predict the survival curves influenced by the presence of AuNPs. In the applied method, a specific volume was partitioned into concentric shells, and the damage induced in that volume was calculated based on the spherical dose distribution generated by a single nanoparticle. This calculation assumed a concentration of AuNPs at the center of a sphere and evenly superimposed their effects across the analyzed volume. The survival curves obtained lead to the conclusion that significant damage is caused by only one nanoparticle with a diameter of 100 nanometers, primarily due to its high gold mass concentration ($\approx$ 2.4E-3 mg/g). Moreover, even with the lowest concentration tested, which amounts to approximately 3.0×10^{-4} mg of gold per gram of tissue and employs nanoparticles with a diameter of 12.5 nanometers, the survival fraction is significantly reduced. In this scenario, the SER reached its minimum value of 1.77, while the maximum value was achieved for the case with the largest nanoparticle diameter. The proposed method, although slightly different from the LEM principle, yielded reasonable results, and conducting experimental tests will be essential to establish practical correlations between theory and medical applications.

Simulations involving the distribution of AuNPs within an elliptical cell were also conducted, and they confirmed that gold nanoparticles can enhance energy deposition in the nucleus, even when they are not in direct contact with it. The enhancement was demonstrated in two different ways: by assessing the dose within small compartments of the nucleus and by calculating the total energy deposited within the entire nucleus. The results obtained from both approaches are consistent. It was concluded that six AuNPs with a diameter of 100 nm are insufficient to induce significant damage to the nucleus,

even when positioned in close proximity. On the other hand, 2000 AuNPs dispersed in the cytoplasm caused noticeable damage, whether using AuNPs with a diameter of 100 or 50 nm. Although the scenario with the largest diameter is not applicable in real life, it demonstrated the undeniable radiosensitizing effect of gold atoms. In the scenario involving the distribution of 2000 AuNPs with a 50 nm diameter, the gold concentration is comparable to the gold concentrations achieved in vivo for tumors, and the results were promising. Using this concentration, the dose absorbed by the nucleus approximately doubled compared to the case without AuNPs, for both nanosphere diameters of 100 and 50 nm. Besides, when considering the same distribution of AuNPs dispersed in the external medium, both studied sizes lead to a similar dose in the sensitive target. It was noticed that even when AuNPs are at considerable distances from the nucleus, a concentration consisting of a mass-weight condition of 1.5% is sufficient to provide the dose enhancement attributed to the presence of gold.

Although this study concludes that the inclusion of gold nanoparticles in a medium enhances energy deposition within that medium, it is important to note that there is still much work to be done in this field. This is primarily due to the significant uncertainties associated with Monte Carlo simulations. In addition to running the simulations with different random number generation seeds, considering the utilization of variance reduction techniques should be a viable option in future work. Furthermore, the influence of nanosphere size on dose enhancement was explored through irradiation using the same source size. This inherently benefits larger AuNPs because more incident photons interact with gold atoms instead of being dispersed in the surrounding medium. Therefore, future tasks could focus on studying smaller nanoparticles with sources that closely match the size of the nanosphere. This investigation will entail exploring new values for the DER, which in turn will influence the survival curve predicted by the method proposed in this work. As the technique used to derive the survival curves relied on several theoretical approximations, it becomes imperative to conduct experimental studies to assess the practicality and validity of the method. Finally, further simulations can investigate the use of various energy sources and nanoparticle sizes. Notably, at the Institute of Physics for Advanced Materials, Nanotechnology, and Photonics (IFIMUP), nanoparticles are produced through laser ablation, leading to diameters that frequently conform to log-normal or normal distributions. Therefore, it would be advantageous to explore distributions of AuNPs with diverse sizes in future research, moving away from a fixed diameter approach.

Appendix A

KERMA expression

Consider N photons, each with an initial energy of k and transferring a mean energy of dE_{tr}. In this context, Equation 2.14 can be expressed as follows:

$$\frac{\mu_{tr}}{\rho} = \frac{1}{\rho\, dl}\frac{N dE_{tr}}{Nk}$$

The total energy transferred to the charged particles in a certain volume V and mass density *rho* is:

$$\begin{aligned} \frac{dE_{tr}}{dm} &= \frac{k\, dl\, \mu_{tr}}{dm} \\ \Leftrightarrow \frac{dE_{tr}}{dm} &= k\left[\frac{dl}{dV}\right]\frac{\mu_{tr}}{\rho} \\ \Leftrightarrow \frac{dE_{tr}}{dm} &= k\phi\frac{\mu_{tr}}{\rho} \end{aligned}$$

If ϕ is the particle fluence and k the energy of each particle, their product is the energy fluence *psi*, thus resulting in Equation 2.16b.

Appendix B

SpekPy settings

Method	Category	Description
filter()	G	Apply a filter of specified material and thickness
multi_filter()	G	Apply multiple filters of specified thicknesses
set()	G	Change a keyword parameter for a spectrum instance
clone()	G	Make a copy of a spectrum instance
get_spectrum()	E	Return the fluence spectrum and energy bins
get_kerma()	E	Air kerma
get_hvl1()	E	First half-value layer (material selectable)
get_hvl2()	E	Second half-value layer (material selectable)
get_hc()	E	Homogeneity coefficient (material selectable)
get_emean()	E	Mean energy of the spectrum
get_eeff()	E	Effective energy of the spectrum (material selectable)
get_matl()	E	Thickness for a specified attenuation (material selectable)
get_flu()	E	Integrated fluence of the spectrum
get_eflu()	E	Integrated energy fluence of the spectrum
get_std_results()	E	Standard results such as beam-quality metrics
make_matl()	M	Create new material (by formula or weight fractions)
remove_matl()	M	Delete a material from the database
show_matl()	M	Show the materials available
load_state()	S	Load a previously saved state
save_state()	S	Save a spectrum instance state
remove_state()	S	Permanently remove a state
show_states()	S	Show the available saved states
export_spectrum()	IO	Export a spectrum to a text file
load_from_file()	IO	Load a spectrum from a text file

TABLE B.1: Available features within SpekPy toolkit [48].

Appendix C

PENELOPE data

C.1 Database for photon interactions

This appendix provides a brief overview of the database and some of the methods employed by the PENELOPE system.

Rayleigh: The atomic cross sections and non-relativistic atomic form factors employed in PENELOPE are sourced from the EPDL (Evaluated Photon Data Library) [49]. Computations of the atomic form factor F(x, Z) are challenging and, due to their reliance on atomic wave functions, they can be analytically performed solely for the hydrogen atom. In the case of all other atoms, these calculations depend on a range of approximations and atomic models.

Photoelectric: The photoelectric absorption database within PENELOPE consists of tables that include total atomic cross sections, as well as cross sections for the K shell, and the L, M, and N subshells. This database covers an energy range from 50 eV to 1 GeV for elements with atomic numbers $Z = 1 - 99$. PENELOPE employs ionization energies obtained through a combination of experimental data and theoretical calculations [50]. The compilation of photoelectric cross section data has been carried out using the Fortran program photacs [51]. This program has the capability to compute partial cross sections for specific subshells up to a predetermined maximum energy, effectively describing the behavior of the cross section near absorption edges. For energies beyond this maximum, the partial cross section was extrapolated from the numerical table using an analytical formula [52], followed by the inclusion of necessary corrections.

Compton: The differential cross section (DCS) for Compton scattering by a free electron at rest is expressed by the familiar Klein–Nishina formula. However, while this simplistic DCS was commonly utilized in older Monte Carlo transport codes, it merely provides a rough approximation for the Compton interactions of photons with atoms. In the context of PENELOPE, Compton scattering events are delineated using the cross section derived from the relativistic impulse approximation [12], which necessitates the incorporation of ionization energies [50]. With the scattering angle of the incident photon known, it becomes possible to compute both the energy of the scattered photon (E') and the angle of the Compton electron.

Pair Production: The polar angles of the directions of movement of the electron and positron ($\theta_{-} and \theta_{+}$) relative to the direction of the incident photon are sampled from expressions obtained from high-energy theory [53].

	$\Gamma(X)$	$g(X)$
Rayleigh ($i = 1; X = q^2$)	$\Gamma(q^2) = \left[4\pi \int_0^\infty \rho(r) \frac{sen(qr/h)}{qr/h} r^2 dr\right]^2$	$g(q^2) = \frac{1 + \left[1 - \frac{1}{2}\left(\frac{qc}{E}\right)^2\right]^2}{2}$
Compton ($i = 1,2; X = \tau$)	$\Gamma(\tau) = \begin{cases} \ln(1+2\kappa)\frac{1}{\tau \ln(1+2\kappa)}, & i = 1 \\ \frac{2\kappa(1+\kappa)}{(1+2\kappa)^2}\frac{(1+2\kappa)^2}{2\kappa(1+\kappa)}\tau, & i = 2 \end{cases}$	$g_{1,2}(\tau) = \left[1 - \frac{(1-\tau)[(2\kappa+1)\tau - 1]}{\kappa^2\tau(1-\tau^2)}\right]\frac{S(E,\theta)}{S(E,\theta=\pi)}$
Pair Production ($i = 1,2; X = \epsilon$)	$\Gamma(\epsilon) = \begin{cases} \left[\frac{3}{2}\left(\frac{1}{2} - \frac{1}{\kappa}\right)^2 \phi_1\left(\frac{1}{2}\right)\right] \frac{\frac{3}{2}\left(\frac{1}{2} - \epsilon\right)^2}{\left(\frac{1}{2} - \frac{1}{\kappa}\right)^3}, & i = 1 \\ \phi_2\left(\frac{1}{2}\right)\left[\frac{1}{2}\left(\frac{1}{2} - \frac{1}{\kappa}\right)^{-1}\right], & i = 2 \end{cases}$	$g_i(\epsilon) = \phi_i(\epsilon)\phi_2\left(\frac{1}{2}\right)$

TABLE C.1: Probability density functions (of the type $\Gamma(X)g(X)$) used by PENELOPE for simulation of photon interactions.

C.2 Number codes used by PENELOPE

label	shell	label	shell	label	shell
1	K $(1s_{1/2})$	11	N2 $(4p_{1/2})$	21	O5 $(5d_{5/2})$
2	L1 $(2s_{1/2})$	12	N3 $(4p_{3/2})$	22	O6 $(5f_{5/2})$
3	L2 $(2p_{1/2})$	13	N4 $(4d_{3/2})$	23	O7 $(5f_{7/2})$
4	L3 $(2p_{3/2})$	14	N5 $(4d_{5/2})$	24	P1 $(6s_{1/2})$
5	M1 $(3s_{1/2})$	15	N6 $(4f_{5/2})$	25	P2 $(6p_{1/2})$
6	M2 $(3p_{1/2})$	16	N7 $(4f_{7/2})$	26	P3 $(6p_{3/2})$
7	M3 $(3p_{3/2})$	17	O1 $(5s_{1/2})$	27	P4 $(6d_{3/2})$
8	M4 $(3d_{3/2})$	18	O2 $(5p_{1/2})$	28	P5 $(6d_{5/2})$
9	M5 $(3d_{5/2})$	19	O3 $(5p_{3/2})$	29	Q1 $(7s_{1/2})$
10	N1 $(4s_{1/2})$	20	O4 $(5d_{3/2})$	30	outer shells

TABLE C.2: Numerical labels for designating atomic electron shells [8].

ICOL	electrons (KPAR=1)	photons (KPAR=2)	positrons (KPAR=3)
1	hinge	coherent (Rayleigh) scattering	hinge
2	hard elastic collision	incoherent (Compton) scattering	hard elastic collision
3	hard inelastic collision	photoelectric absorption	hard inelastic collision
4	hard bremsstrahlung emission	electron-positron pair production	hard bremsstrahlung emission
5	inner-shell impact ionisation		inner-shell impact ionisation
6			annihilation
7	delta interaction	delta interaction	delta interaction
8	auxiliary interaction	auxiliary interaction	auxiliary interaction

TABLE C.3: Code number for the interaction events (ICOL) [8].

Appendix D

Implemented simulations - additional information

D.1 Fortran error within source material

When the 'source material' parameter is set to a non-zero value, it results in an error in the Fortran file 'sourceBoxIsotropicGaussSpectrum' To resolve this issue, the lines 195, 196, 272, and 273 shown in Figure D.1 should be removed.

```
 ! Check sampling efficiency and issue warnings and errors:
 if (nsec.ne.0) nSuccess = nSuccess+1            ! The stack is not empty, source succeded to produce valid particles
 if (.not.warned.and.                            ! Low success rate
&    dble(nhist).gt.max(nSuccess*invWarnLimit,1.0e3))
&  then
   write(*,*) ''
   write(*,'(a,f0.1,a)') 'BIGSpennuc:WARNING: '//
&    'source sampling efficiency lower than ',warnlimit*100,
&    '%.'
   write(*,'(a,f0.0,a,f0.0,a)') 'After ',nhist,
&    ' histories the sampling efficiency is ',
&    nSuccess/dble(nhist)*100.0,'%'
   write(*,'(a)') 'This may result in long simulation times.'
   write(*,'(a)') 'Enlarge the source aperture appropriately.'
   warned = .true.
 endif
```

Line 195
Line 196

```
    ! Sampling efficiency; issue warnings and errors if limits are exceeded:
    if (.not.warned.and.            ! Low success rate
&      dble(ntrials).gt.max(nhist*invWarnLimit,1.0e3))
&    then
      write(*,*) ''
      write(*,'(a,f0.1,a)') 'samplePosition:WARNING: '//
&       'source sampling efficiency lower than ',warnlimit*100,
&       '%.'
      write(*,'(a,f0.0,a,f0.0,a)') 'After ',ntrials,
&       ' trials the sampling efficiency is ',
&      nhist/dble(ntrials)*100.0,'%'
      write(*,'(a)') 'This may result in long simulation times.'
      write(*,'(a)') 'Redefine source parameters appropriately.'
      warned = .true.
    endif
```

Line 272
Line 273

FIGURE D.1: Fortran code that generates errors when specifying the 'source material' in PenEasy input file.

D.2 Water medium

The section of transport parameters in PenEasy input file correpsonds to Table D.1, for all the combinations of source energy and nanoparticle size.

```
[SECTION PENELOPE v.2019-08-06]
 MAT# FILE___(max 20 char) EABS(e-)  EABS(ph)  EABS(e+)  C1      C2      WCC     WCR     DSMAX    COMMENTS
  1   gold.mat             50        50        50        0.0001  0.0001  0.5     0.05    1.0e-5   nanoparicle
  2   water.mat            50        50        50        0.0001  0.0001  0.5     0.05    1.0e-5   source
  3   water.mat            50        50        50        0.0001  0.0001  0.5     0.05    1.0e-5   exterior
 -1 (SET MAT=-1 TO END THE LIST)
[END OF PEN SECTION]
```

TABLE D.1: Transport parameters used for all the simulations that considered a medium of water.

D.3 Propagation of uncertainties

Consider that y is related to n independent measured variables $X_1, X_2, ..., X_n$ by a functional representation:

$$y = f(X_1, X_2, ..., X_n)$$

Then, the uncertainty Δy is given by the following Equation:

$$\Delta y = \sqrt{\left(\frac{\partial f}{\partial X_1}\Delta x_1\right)^2 + \left(\frac{\partial f}{\partial X_2}\Delta x_2\right)^2 + ... + \left(\frac{\partial f}{\partial X_n}\Delta x_n\right)^2} \tag{D.1}$$

The variables Δx_1, Δx_2, ..., Δx_n are the uncertainties of X's around $\bar{x}_1$, $\bar{x}_2$, ..., $\bar{x}_n$ [54].

D.4 Breast tissue medium

D.4.1 Transport Parameters

The section of transport parameters in PenEasy input file corresponds to Table D.2, for all the combinations of source energy and nanoparticle size.

```
[SECTION PENELOPE v.2019-08-06]
 MAT# FILE___(max 20 char) EABS(e-)  EABS(ph)  EABS(e+)  C1    C2    WCC   WCR   DSMAX    COMMENTS
  1   gold.mat             50        50        50        0.1   0.1   1     1     1.0e-8   AuNP
  2   breast.mat           50        50        50        0.1   0.1   1     1     1        tissue
 -1 (SET MAT=-1 TO END THE LIST)
[END OF PEN SECTION]
```

TABLE D.2: Transport parameters used for the simulations using a medium of breast tissue.

D.4.2 Code for reading Spherical dose

```
def radial_dose(file):
    data = open(file, "r")
    a=data.readlines()
    data.close()
    dose=[]
    error=[]
    R=[]
    for i in range(12,1012):
        line=a[i]
        L=line.split()
        R.append(float(L[1]))
        dose.append(float(L[3]))
        error.append(float(L[4]))
    return np.array([R,dose,error])
```

FIGURE D.2: Code implemented for reading data files of spherical dose.

```
from nbformat import read, write

def Remove_Output(Book):
     for cell in Book.cells:
        if hasattr(cell, "outputs"):
             cell.outputs = []
        if hasattr(cell, "prompt_number"):
             del cell["prompt_number"]

Book= read(open("PSF.ipynb"), 4)
Remove_Output(Book)
write(Book, open("psf_new", "w"), 4)
```

FIGURE D.3: Function that can resolve some issues related with the large extent of Phase Space Files in Jupyther Notebook.

D.4.3 Creation of PSF

```
def read_psf(file):
    prim=0
    Ee=0
    Ep=0

    icol_ee=np.zeros(8)
    icol_ep=np.zeros(8)
    icol_pe=np.zeros(8)
    icol_pp=np.zeros(8)

    ILB4=[]



    with open(file, "r") as f:
        for line in f:
            lis=line.split()
            if lis[0]=='#':
                continue

            if float(lis[10])==1: #ILB1
                prim+=1

            if float(lis[10])!=1:  #secondary particle

                icol=int(lis[12])
                ILB4.append(float(lis[13]))

                if float(lis[11])==1:  #parent is an electron

                    if float(lis[0])==1: #particle is an electron
                        icol_ee[icol-1]+=1
                        Ee+=float(lis[1])
                    if float(lis[0])==2: #particle is a photon
                        icol_ep[icol-1]+=1
                        Ep+=float(lis[1])


                elif float(lis[11])==2: #parent is a photon

                    if float(lis[0])==1: #particle is an electron
                        icol_pe[icol-1]+=1
                        Ee+=float(lis[1])
                    if float(lis[0])==2:  #particle is a photon
                        icol_pp[icol-1]+=1
                        Ep+=float(lis[1])


    print('Number of primary particles:', prim,'\n')

    print('Electrons created by electron parents:')
    print('Icol_ee', icol_ee)
    print('Photons created by electron parents:')
    print('Icol_ep', icol_ep,'\n')

    print('Electrons created by photon parents:')
    print('Icol_pe', icol_pe)
    print('Photons created by photon parents:')
    print('Icol_pp', icol_pp,'\n')


    E1=Ee/(sum(icol_pe)+sum(icol_ee))
    E2=Ep/(sum(icol_ep)+sum(icol_pp))

    return E1,E2, ILB4
```

FIGURE D.4: Funtion used for reading and examinign the Phase Space Files.

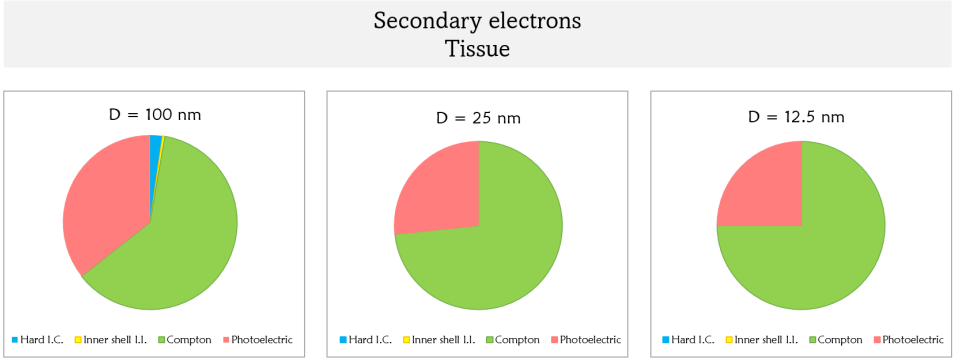

FIGURE D.5: Contribution of the different mechanisms for secondary electrons generation in tissue, assuming an AuNP with diameter of 100 nm (left), 25 nm (center) and 12.5 nm (right).

```
def transitions(ILB4,mini):

    labels, counts = np.unique(ILB4,return_counts=True)

    co=[]
    lab=[]
    Z=[]
    IS1=[]
    IS2 = []
    IS3= []

    for i in range (len(counts)):
        if counts[i]>=mini:
            co.append(counts[i])

            labs=labels[i]
            lab.append(labs)

            z=labs//10**6
            Z.append(z)

            i1=(labs-z*10**6)//10**4
            IS1.append(i1)

            i2=(labs-z*10**6-i1*10**4)//100
            IS2.append(i2)

            IS3.append(labs-z*10**6-i1*10**4-i2*100)

    #label into string
    IS1=shell(IS1)
    IS2=shell(IS2)
    IS3=shell(IS3)

    return co,Z,IS1,IS2,IS3
```

FIGURE D.6: Function used to determine the principal shell transitions involved in atoms ionization.

```
def shell(label):
    result=[]
    cascas=('K','L1','L2','L3','M1','M2','M3','M4','M5','N1','N2','N3','N4','N5','N6','N7','O1','O2','O3',
            'O4','O5','O6','O7','P1','P2','P3','P4','P5','Q1','outer')
    for num in label:
        if num==0:
            result.append(0)
        else:
            result.append(cascas[int(num)-1])
    return result
```

FIGURE D.7: Function developed to transform the number code used by PENELOPE in shell labels.

D = 100 nm

WITH GOLD

Counts	IS1	IS2	IS3
851	L1	M2	0
950	L1	M3	0
663	L1	M4	M5
589	L2	M1	M2
679	L2	M2	M2
1680	L2	M2	M3
882	L2	M2	M4
1376	L2	M2	M5
885	L2	M3	M4
9505	L2	M4	0
789	L2	M4	M4
3303	L2	M4	M5
662	L2	M4	N5
1836	L2	N4	0
998	L3	M1	0
1177	L3	M1	M3
1985	L3	M2	M3
821	L3	M2	M5
2809	L3	M3	M3
2992	L3	M3	M4
4095	L3	M3	M5
545	L3	M3	N2
1242	L3	M3	N3
692	L3	M3	N4
933	L3	M3	N5
1690	L3	M4	0

Counts	IS1	IS2	IS3
7671	L3	M4	M5
1207	L3	M4	N5
14672	L3	M5	0
5192	L3	M5	M5
683	L3	M5	N3
1400	L3	M5	N4
1856	L3	M5	N5
2721	L3	N5	0
606	M4	N3	N4
658	M4	N4	N4
1311	M4	N4	N5
771	M4	N4	N6
951	M4	N4	N7
881	M4	N5	N6
1620	M4	N6	0
889	M4	N6	N6
2731	M4	N6	N7
847	M5	N3	N5
1380	M5	N4	N5
752	M5	N4	N7
1525	M5	N5	N5
1229	M5	N5	N6
1993	M5	N5	N7
3469	M5	N6	N7
2525	M5	N7	0
2477	M5	N7	N7

WITHOUT GOLD

Counts	IS1	IS2	IS3
1	K	L1	L3
1	K	L3	L3
2	K	L1	L1
4	K	L2	L3
1	K	L3	0
2	K	L3	L3
2	K	L2	L3
1	K	L2	M1
1	K	L2	M3

TABLE D.3: Principal transitions detected in the surrounding halo of a nanoparticle with 100 nm diameter.

D = 50 nm

WITH GOLD

Counts	IS1	IS2	IS3
106	L1	M2	0
131	L1	M3	0
230	L2	M2	M3
195	L2	M2	M5
112	L2	M3	M4
1120	L2	M4	0
108	L2	M4	M4
421	L2	M4	M5
228	L2	N4	0
122	L3	M1	0
167	L3	M1	M3
316	L3	M2	M3
116	L3	M2	M5
364	L3	M3	M3
407	L3	M3	M4
543	L3	M3	M5
158	L3	M3	N3
117	L3	M3	N5
215	L3	M4	0
1019	L3	M4	M5
160	L3	M4	N5
1841	L3	M5	0
664	L3	M5	M5
191	L3	M5	N4

Counts	IS1	IS2	IS3
205	L3	M5	N5
335	L3	N5	0
140	M4	N3	N4
145	M4	N4	N4
285	M4	N4	N5
194	M4	N4	N6
230	M4	N4	N7
189	M4	N5	N6
206	M4	N6	0
206	M4	N6	N6
604	M4	N6	N7
126	M5	N1	N5
125	M5	N2	N5
227	M5	N3	N5
345	M5	N4	N5
162	M5	N4	N7
367	M5	N5	N5
282	M5	N5	N6
498	M5	N5	N7
840	M5	N6	N7
307	M5	N7	0
528	M5	N7	N7
106	N4	N6	N7
135	N7	O5	O5

WITHOUT GOLD

Counts	IS1	IS2	IS3
1	K	L1	L1
2	K	L2	L3
1	K	L3	L3

TABLE D.4: Principal transitions detected in the surrounding halo of a nanoparticle with 50 nm diameter.

D = 25 nm

WITH GOLD

Counts	IS1	IS2	IS3
16	L1	M3	0
21	L2	M2	M3
18	L2	M2	M5
120	L2	M4	0
45	L2	M4	M5
29	L2	N4	0
15	L3	M1	0
29	L3	M1	M3
27	L3	M2	M3
35	L3	M3	M3
34	L3	M3	M4
45	L3	M3	M5
18	L3	M3	N3
15	L3	M3	N5
20	L3	M4	0
91	L3	M4	M5
173	L3	M5	0
76	L3	M5	M5
23	L3	M5	N4
18	L3	M5	N5
35	L3	N5	0
15	M2	M4	N6
18	M2	M4	N7
21	M3	M5	N7
16	M3	N3	N6
22	M3	N3	N7
16	M3	N6	N7
32	M4	N3	N4
28	M4	N4	N4
53	M4	N4	N5
30	M4	N4	N6
39	M4	N4	N7
21	M4	N5	N6
27	M4	N6	0
40	M4	N6	N6
100	M4	N6	N7
22	M5	N1	N5
45	M5	N3	N5
63	M5	N4	N5
31	M5	N4	N7
57	M5	N5	N5
54	M5	N5	N6
81	M5	N5	N7
130	M5	N6	N7
33	M5	N7	0
106	M5	N7	N7
17	N4	N6	N7
19	N5	N6	N7
21	N5	N7	N7
18	N5	N7	O5
15	N6	O4	O4
18	N6	O4	O5
23	N7	O4	O5
27	N7	O5	O5

D = 12.5 nm

WITH GOLD

Counts	IS1	IS2	IS3
3	L1	L3	N5
3	L2	L3	N4
5	L2	M4	0
2	L2	M4	M5
4	L3	M3	M3
2	L3	M4	0
8	L3	M4	M5
2	L3	M4	N5
18	L3	M5	0
6	L3	M5	M5
4	L3	M5	N5
3	L3	N5	0
2	M2	N2	N3
3	M3	M5	N7
2	M4	N1	N6
3	M4	N2	N4
2	M4	N3	N4
5	M4	N4	N5
2	M4	N5	N6
6	M4	N6	N6
4	M4	N6	N7
2	M5	N1	N5
2	M5	N1	N7
8	M5	N4	N5
2	M5	N4	N7
3	M5	N5	N5
5	M5	N5	N6
9	M5	N5	N7
21	M5	N6	N7
2	M5	N7	0
10	M5	N7	N7
2	M5	N7	O5
2	N2	N4	N6
2	N4	N6	N7
2	N5	N6	N7
2	N5	N7	N7
2	N5	N7	O4
2	N5	N7	O5
3	N6	O4	O4
3	N6	O4	O5
5	N7	O5	O5

TABLE D.5: Principal transitions detected in the surrounding halo of a nanoparticle with 25 nm (left) and 12.5 nm diameter (right).

D.4.4 Function for grouping shells

```
def group(bins, dose,volumes):
    N = len(bins)-1
    g=[]
    dV=[]
    for i in range(0,N):
        g.append([])
        dV.append([])
    for j in range(0,len(dose)):
        for i in range(0,N):
            if dose[j]<bins[i+1]:
                g[i].append(dose[j])
                dV[i].append(volumes[j])
                break
    return g,dV
```

FIGURE D.8: Function developed for grouping the subshells around a AuNP in ticker shells.

```
cell
0000000000000000000000000000000000000000000000000000000000000000000000
c nucleus
SURFACE (   1)
INDICES=( 0, 0, 0, 0, 0)
    AXX=(+6.250000000000000E+06,   0)
    AYY=(+6.250000000000000E+06,   0)
    AZZ=(+9.999999999999998E+09,   0)
     A0=(-1.000000000000000E-00,   0)
0000000000000000000000000000000000000000000000000000000000000000000000
BODY    (   1)
MATERIAL(   1)
SURFACE (   1), SIDE POINTER=(-1)
0000000000000000000000000000000000000000000000000000000000000000000000
c cytoplasm
SURFACE (   2)
INDICES=( 0, 0, 0, 0, 0)
    AXX=(+1.168736303871430E+06,   0)
    AYY=(+5.536332179930795E+06,   0)
    AZZ=(+1.000000000000000E+08,   0)
     A0=(-1.000000000000000E-00,   0)
0000000000000000000000000000000000000000000000000000000000000000000000
BODY    (   2)
MATERIAL(   2)
SURFACE (   2), SIDE POINTER=(-1)
SURFACE (   1), SIDE POINTER=(+1)
0000000000000000000000000000000000000000000000000000000000000000000000
c exterior
SURFACE (   3)
INDICES=( 1, 1, 1, 0,-1)
X-SCALE=( 2.000000000000000e+01,   0)
Y-SCALE=( 2.000000000000000e+01,   0)
Z-SCALE=( 2.000000000000000e+01,   0)
0000000000000000000000000000000000000000000000000000000000000000000000
BODY    (   3)
MATERIAL(   3)
SURFACE (   3), SIDE POINTER=(-1)
SURFACE (   2), SIDE POINTER=(+1)
SURFACE (   1), SIDE POINTER=(+1)
0000000000000000000000000000000000000000000000000000000000000000000000
END      0000000000000000000000000000000000000000000000000000000000000000
```

FIGURE D.9: Input geometry file of the cell. The nucleus and the cytoplasm are defined by ellipsoids with different axis. The external medium is a sphere.

```
def dose_vox(N,xbins,ybins,zbins,file):
    Nmat=xbins*ybins
    data = open(file, "r")
    a=data.readlines()
    a=a[14:]  #exclude the 14-line header
    data.close()

    mat_dose=np.zeros((ybins,xbins,zbins))
    mat_sigma=np.zeros((ybins,xbins,zbins))

    for z in range(0,zbins):
        begin=np.arange((z*(Nmat+ybins+1)),(z*(Nmat+ybins+1))+Nmat+ybins,xbins+1) #scrolling the blocks with fixed z

        for i in np.arange(0,len(begin)): # scrolling y-axis
            col=0
            for j in np.arange(begin[i],begin[i]+xbins): # read each x-value for the same y
                line=a[j]
                L=line.split()
                e=float(L[10])
                mat_dose[(ybins-1)-i,col,z]=float(L[9])*1.6022*10**(-16)*N
                mat_sigma[i,col,z]=e*1.6022*10**(-16)*N
                col+=1

    return mat_dose,mat_sigma
```

FIGURE D.10: Code used for reading the file 'TallySpatialDose Distrib' given by PenEasy.

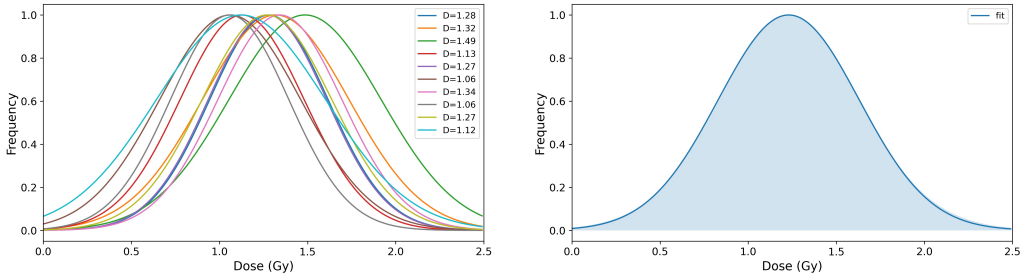

FIGURE D.11: Example of various probability density functions for doses on the left and the result of their superimposition on the right.

```
def aleat_cell(a,b,c):
    num = np.random.uniform(-1, 1)
    theta = np.arcsin(num)
    phi=np.random.uniform(0, 2*np.pi)
    rad = ((np.random.uniform(0,1))**(1/3))
    x=a*rad*np.cos(phi)*np.cos(theta)
    y=b*rad*np.sin(phi)*np.cos(theta)
    z=c*rad*np.sin(theta)
    return (np.array([x,y,z]))


def nucleus(an,bn,cn,x,y,z):
    #funtion returns 1 if the sample is inside the nucleus and returns 0 otherwise
    num = ((x**2/an**2)+(y**2/bn**2)+(z**2/cn**2))
    if num<=1:
        return 1
    else:
        return 0


p_cito=np.zeros((N,3)) #each column is a coordinate: x, y or z.


i=0
while i<N:
    x,y,z=aleat_cell(a,b,c)
    if nucleus(an,bn,cn,x,y,z)==0:
        p_cito[i,:]=np.array([x,y,z])
        i+=1

x=np.array(p_cito[:,0])
y=np.array(p_cito[:,1])
z=np.array(p_cito[:,2])
```

FIGURE D.12: Developed code for scattering the positions of numerous nanoparticles within the cytoplasm of a cell.

```
def sphere(n,mat,R,xx,yy,zz):
    L1=("0000000000000000000000000000000000000000000000000000000000000000")
    s2=(", SIDE POINTER=(-1)")

    if n<=9:
        L2=("SURFACE (   %d)" % n)
        L11=("BODY    (   %d)" % n)
        s1=("SURFACE (   %d)" % n)
    elif n<=99:
        L2=("SURFACE (  %d)" % n)
        L11=("BODY    (  %d)" % n)
        s1=("SURFACE (  %d)" % n)
    elif n<=999:
        L2=("SURFACE ( %d)" % n)
        L11=("BODY    ( %d)" % n)
        s1=("SURFACE ( %d)" % n)
    else:
        L2=("SURFACE (%d)" % n)
        L11=("BODY    (%d)" % n)
        s1=("SURFACE (%d)" % n)

    L3=("INDICES=( 1, 1, 1, 0,-1)")
    L4=("X-SCALE=( %.15e,   0)" % R)
    L5=("Y-SCALE=( %.15e,   0)" % R)
    L6=("Z-SCALE=( %.15e,   0)" % R)
    L12=("MATERIAL(   %d)" % mat)
    L13=s1+s2

    if xx<0:
        L7=("X-SHIFT=(%.15e,   0)" % xx)
    else:
        L7=("X-SHIFT=( %.15e,   0)" % xx)
    if yy<0:
        L8=("Y-SHIFT=(%.15e,   0)" % yy)
    else:
        L8=("Y-SHIFT=( %.15e,   0)" % yy)
    if zz<0:
        L9=("Z-SHIFT=(%.15e,   0)" % zz)
    else:
        L9=("Z-SHIFT=( %.15e,   0)" % zz)
    return (L1,L2,L3,L4,L5,L6,L7,L8,L9,L1,L11,L12,L13)
```

FIGURE D.13: Code used for writing the geometry file of one nanosphere.

D.4.5 Lognormal Distribution

The probability density function for *lognorm* in the standardized form is [55]:

$$f(x,s) = \frac{1}{sx\sqrt{2\pi}} \exp\left(-\frac{\log^2(x)}{2s^2}\right) \tag{D.2}$$

where $x > 0$ and $s > 0$.

This function can be shift and scaled by the use of **loc** and **scale** parameters, as follows:

$$g(x,s) = \frac{f(\frac{x-\mathbf{loc}}{\mathbf{scale}}, s)}{\mathbf{scale}}$$

This means that, if a random variable X is normally distributed with mean μ and standard deviation σ, then $Y = \exp(X)$ is lognormally distributed with $s = \sigma$ and $\mathbf{scale} = \exp(\mu)$.

Bibliography

[1] World Cancer Research Fund International: Worldwide cancer data. [Online]. Available: https://www.wcrf.org/cancer-trends/worldwide-cancer-data/ [Cited on page 1.]

[2] Cancro em Portugal. [Online]. Available: https://gco.iarc.fr/today/data/factsheets/populations/620-portugal-fact-sheets.pdf [Cited on page 1.]

[3] K. Sztandera, G. Michał, and K.-M. Barbara, "Gold nanoparticles in cancer treatment," *Molecular Pharmaceutics*, vol. 16, no. 1, pp. 1–23, 2019, pMID: 30452861. [Online]. Available: https://doi.org/10.1021/acs.molpharmaceut.8b00810 [Cited on pages 1, 2, and 29.]

[4] H. S. Ali, B. M. El-Haj, S. Saifullah, and M. Kawish, "Chapter 4 - gold nanoparticles in cancer diagnosis and therapy," in *Metal Nanoparticles for Drug Delivery and Diagnostic Applications*, ser. Micro and Nano Technologies, M. R. Shah, M. Imran, and S. Ullah, Eds. Elsevier, 2020, pp. 43–58. [Online]. Available: https://www.sciencedirect.com/science/article/pii/B9780128169605000045 [Cited on page 2.]

[5] Z. Kuncic and S. Lacombe, "Nanoparticle radio-enhancement: Principles, progress and application to cancer treatment," *Physics in Medicine and Biology*, vol. 63, no. 2, 2018. [Cited on pages xv, 2, 31, and 32.]

[6] S. J. McMahon, W. B. Hyland, E. Brun, K. T. Butterworth, J. A. Coulter, T. Douki, D. G. Hirst, S. Jain, A. P. Kavanagh, Z. Krpetic, M. H. Mendenhall, M. F. Muir, K. M. Prise, H. Requardt, L. Sanche, G. Schettino, F. J. Currell, and C. Sicard-Roselli, "Energy dependence of gold nanoparticle radiosensitization in plasmid dna," *The Journal of Physical Chemistry C*, vol. 115, no. 41, pp. 20 160–20 167, 2011. [Online]. Available: https://doi.org/10.1021/jp206854s [Cited on pages 3 and 48.]

[7] E. B. Podgorsak, *Radiation Physics for Medical Physicists*. Springer, 2006. [Cited on pages xv, 4, 9, 11, 12, 14, 15, 16, 17, 23, and 25.]

[8] N. E. Agency, *PENELOPE 2018: A code system for Monte Carlo simulation of electron and photon transport*, 2019. [Online]. Available: https://www.oecd-ilibrary.org/content/publication/32da5043-en [Cited on pages xv, xix, 5, 6, 7, 9, 11, 13, 14, 15, 49, 50, 51, 52, 53, 54, 55, 56, 61, 62, 66, 97, and 115.]

[9] F. H. Attix, *Introduction to Radiological Physics and Radiation Dosimetry*. New York: John Wiley and Sons, 1986. [Cited on pages 7, 10, 23, and 26.]

[10] E. J. Hall, *Radiobiology for the Radiologist*. Hagerstown, Md.: Medical Dept., Harper & Row, 1973. [Cited on pages 8, 26, 33, 34, 35, and 37.]

[11] P. Andreo, D. T. Burns, A. E. Nahum, J. Seuntjens, and F. H. Attix, *Fundamentals of Ionizing Radiation Dosimetry*, 2016. [Cited on pages xv, 9, 10, 11, 15, 16, 24, 25, 26, 30, and 31.]

[12] R. Ribberfors, "X-ray incoherent scattering total cross sections and energy-absorption cross sections by means of simple calculation routines. physical review a, 27 (6). 3061-3070," 1983. [Online]. Available: doi:10.1103/physreva.27.3061 [Cited on pages 13 and 114.]

[13] Wikizero: Parâmetro de impacto. [Online]. Available: https://www.wikizero.com/pt/Parametro_de_impacto [Cited on page 14.]

[14] J. Bushberg, *The Essential Physics of Medical Imaging*, 2nd ed., 2002. [Cited on pages xv, 17, 18, 19, 20, and 22.]

[15] F. M. Khan, *The Physics of Radiation Therapy*, 3rd ed. 530 Walnut Street, Philadelphia, PA 19106, USA: Lippincott Williams & Wilkins, 2003. [Cited on pages xv, 17, 18, 19, 20, and 21.]

[16] P. A. Gavin Poludniowski, Artur Omar, *Calculating X-ray Tube Spectra: Analytical and Monte Carlo Approaches*. Taylor & Francis Group, LLC, 2022. [Cited on pages 19, 20, and 50.]

[17] P. P. Dendy and B. Heaton, *Physics for Diagnostic Radiology*. Chichester, England: John Wiley & Sons, 2012. [Cited on pages 20 and 21.]

[18] X-ray spectra, Kieranmaher - Own work, Public Domain. [Online]. Available: https://commons.wikimedia.org/w/index.php?curid=12711485 [Cited on pages xv and 21.]

[19] W. Li, A. Belchior, M. Beuve, Y. Chen, S. Di Maria, W. Friedland, B. Gervais, B. Heide, N. Hocine, A. Ipatov, A. Klapproth, C. Li, J. Li, G. Multhoff, F. Poignant, R. Qiu, H. Rabus, B. Rudek, J. Schuemann, S. Stangl, E. Testa, C. Villagrasa, W. Xie, and Y. Zhang, "Intercomparison of dose enhancement ratio and secondary electron spectra for gold nanoparticles irradiated by x-rays calculated using multiple monte carlo simulation codes," *Physica Medica*, vol. 69, pp. 147–163, 2020. [Online]. Available: https://doi.org/10.1016/j.ejmp.2019.12.011 [Cited on pages 29, 32, 41, 71, 72, and 78.]

[20] "Nist: photon cross section data for a single element, compound, or mixture," URL: https://physics.nist.gov/PhysRefData/Xcom/html/xcom1.html. [Cited on page 30.]

[21] L. B. N. Laboratory, "Table 1-1. electron binding energies for the elements in their natural forms," Online. [Online]. Available: https://xdb.lbl.gov/Section1/Table_1-1.pdf [Cited on pages xix and 31.]

[22] L. Castillo-Rico, M. Flores-Mancera, and G. Massillon-JL, "Stopping power and csda range of electrons in liquid water, lif, caf2, and al2o3 from the energy gap up to 433 kev," *Nuclear Instruments and Methods in Physics Research Section B: Beam Interactions with Materials and Atoms*, vol. 502, pp. 189–197, 2021. [Online]. Available: https://www.sciencedirect.com/science/article/pii/S0168583X21002342 [Cited on pages xv and 32.]

[23] P. Pianetta, "X-ray data booklet." [Online]. Available: https://xdb.lbl.gov/Section3/Sec_3-2.html [Cited on pages xv and 32.]

[24] R. K. Hobbie and B. J. Roth, *Intermediate Physics for Medicine and Biology*, 4th ed. New York: Springer, 2007. [Cited on page 33.]

[25] M. Tubiana, *Introduction to Radiobiology*, 2005. [Cited on pages 33, 34, 35, and 36.]

[26] M. C. Joiner and A. J. van der Kogel, Eds., *Basic Clinical Radiobiology*, 5th ed., 2019. [Cited on pages xv, 34, and 36.]

[27] D. F. Regulla, L. B. Hiebert, and M. Seidenbusch, "Physical and biological interface dose effects in tissue due to x-ray-induced release of secondary radiation from metallic gold surfaces," *Institute of Radiation Protection and Institute of Radiation Biology, GSF-National Research Center for Environment and Health*, 2000. [Cited on page 37.]

[28] D. M. Herold, I. J. Das, C. C. Stobbe, R. V. Iyer, and J. D. Chapman, "Gold microspheres: A selective technique for producing biologically effective dose enhancement," *International Journal of Radiation Biology*, November 2000. [Cited on page 37.]

[29] J. F. Hainfeld, D. N. Slatkin, and H. M. Smilowitz, "The use of gold nanoparticles to enhance radiotherapy in mice," 2004. [Cited on pages 38 and 101.]

[30] E. Lechtman, N. Chattopadhyay, Z. Cai, S. Mashouf, R. Reilly, and J.-P. Pignol, "Implications on clinical scenario of gold nanoparticle radiosensitization in regards to photon energy, nanoparticle size, concentration and location," *Physics in medicine and biology*, vol. 56, pp. 4631–47, 08 2011. [Cited on pages xv, 38, 40, 41, and 42.]

[31] J. D. Carter, N. N. Cheng, Y. Qu, G. D. Suarez, and T. Guo, "Nanoscale energy deposition by x-ray absorbing nanostructures," *The Journal of Physical Chemistry B*, vol. 111, no. 40, pp. 11 622–11 625, 2007, pMID: 17854220. [Online]. Available: https://doi.org/10.1021/jp075253u [Cited on page 39.]

[32] S. J. McMahon *et al.*, "Biological consequences of nanoscale energy deposition near irradiated heavy atom nanoparticles," *Scientific reports*, vol. 1, p. 18, 2011. [Cited on pages xv, 39, 40, 46, and 48.]

[33] W. Sung, S.-J. Ye, A. L. McNamara, S. J. McMahon, J. Hainfeld, J. Shin, H. M. Smilowitz, H. Paganetti, and J. Schuemann, "Dependence of gold nanoparticle radiosensitization on cell geometry," 2017. [Cited on pages 40 and 43.]

[34] W. Sung and J. Schuemann, "Energy optimization in gold nanoparticle enhanced radiation therapy," *Phys. Med. Biol.*, vol. 63, p. 135001, 2018. [Cited on pages 41, 43, 94, and 95.]

[35] Y. Lin *et al.*, "Comparing gold nano-particle enhanced radiotherapy with protons, megavoltage photons and kilovoltage photons: a monte carlo simulation," *Phys. Med. Biol.*, vol. 59, p. 7675, 2014. [Cited on pages 41, 42, and 44.]

[36] W. Sung and et al, "Evaluation of the microscopic dose enhancement for nanoparticle-enhanced auger therapy," *Phys. Med. Biol.*, vol. 61, p. 7522, 2016. [Cited on pages 41 and 43.]

[37] E. Lechtman *et al.*, "A monte carlo-based model of gold nanoparticle radiosensitization accounting for increased radiobiological effectiveness," *Phys. Med. Biol.*, vol. 58, p. 3075, 2013. [Cited on pages 42, 43, and 44.]

[38] Y. Lin *et al.*, "Biological modeling of gold nanoparticle enhanced radiotherapy for proton therapy," *Phys. Med. Biol.*, vol. 60, p. 4149, 2015. [Cited on pages xv, 43, 44, and 47.]

[39] A. L. McNamara, W. W. Kam, N. Scales, S. J. McMahon, J. W. Bennett, H. L. Byrne, J. Schuemann, H. Paganetti, R. Banati, and Z. Kuncic, "Dose enhancement effects to the nucleus and mitochondria from gold nanoparticles in the cytosol," *Physics in Medicine and Biology*, vol. 61, no. 16, p. 5993–6010, 2016. [Cited on page 44.]

[40] G. Kraft, M. Scholz, and U. Bechthold, "Tumor therapy and track structure," *Radiation and Environmental Biophysics*, vol. 38, pp. 229–237, 1999. [Cited on pages 45 and 47.]

[41] M. Scholz and G. Kraft, "The physical and radiobiological basis of the local effect model (lem): A response to the commentary by r. katz," *GSI / Biophysics, Darmstadt*, 2006. [Cited on pages xv, 46, and 47.]

[42] O. N. Vassiliev, *Monte Carlo Methods for Radiation Transport: Fundamentals and Advanced Topics*, ser. Biological and Medical Physics, Biomedical Engineering. Springer, 2017. [Cited on pages 49, 51, 52, 54, 55, and 67.]

[43] Fortran Programming Language. [Online]. Available: https://fortran-lang.org/# [Cited on page 56.]

[44] J. Sempau, A. Badal, and L. Brualla, "A PENELOPE-based system for the automated Monte Carlo simulation of clinacs and voxelized geometries—application to far-from-axis fields," *Med. Phys.*, vol. 38, pp. 5887 – 5895, 2011, available at http://dx.doi.org/10.1118/1.3643029. [Cited on pages 60, 68, and 69.]

[45] ICRU (1989), Tissue Substitutes in Radiation Dosimetry and Measurement, Report 44 of the International Commission on Radiation Units and Measurements. [Online].

Available: https://physics.nist.gov/PhysRefData/XrayMassCoef/tab2.html [Cited on page 79.]

[46] "My jupyter notebook crashed and now won't open," URL: https://www.purplefrogsystems.com/2023/02/my-jupyter-notebook-crashed-and-now-wont-open/. [Cited on page 83.]

[47] NIST: X-Ray Mass Attenuation Coefficients. [Online]. Available: https://physics.nist.gov/PhysRefData/XrayMassCoef/tab4.html [Cited on page 91.]

[48] G. Poludniowski, A. Omar, R. Bujila, and P. Andreo, "Technical note: Spekpy v2.0—a software toolkit for modeling x-ray tube spectra," *Medical Physics*, vol. 48, 05 2021. [Cited on pages xix and 111.]

[49] D. Cullen, "Evaluated photon data library," 1997. [Cited on page 113.]

[50] T. A. Carlson, "Photoelectron and auger spectroscopy, plenum," 1975. [Cited on pages 113 and 114.]

[51] L. Sabbatucci and F. Salvat, "Theory and calculation of the atomic photoeffect," *Radiation Physics and Chemistry*, vol. 121, pp. 122–140, 2016. [Online]. Available: https://api.semanticscholar.org/CorpusID:122022671 [Cited on page 113.]

[52] R. H. Pratt, "Atomic photoelectric effect at high energies." physical review 117.4: 1017." 1960. [Cited on page 113.]

[53] J. W. MOTZ, H. A. OLSEN, and H. W. KOCH, "Pair production by photons," *Rev. Mod. Phys.*, Oct 1969. [Online]. Available: https://link.aps.org/doi/10.1103/RevModPhys.41.581 [Cited on page 114.]

[54] L. Kirkup and R. B. Frenkel, *An Introduction to Uncertainty in Measurement Using the GUM (Guide to the Expression of Uncertainty in Measurement)*, June 2006. [Cited on page 118.]

[55] Scipy: lognorm distribution. [Online]. Available: https://docs.scipy.org/doc/scipy/reference/generated/scipy.stats.lognorm.html#scipy.stats.lognorm [Cited on page 127.]